Measuring Ultracomplex Supercontinuum Pulses and Spatio-Temporal Distortions

A Thesis
Presented to
The Academic Faculty

by

Xun Gu

In Partial Fulfillment
of the Requirements for the Degree
Doctor of Philosophy

School of Physics
Georgia Institute of Technology
July 2004

Measuring Ultracomplex Supercontinuum Pulses and Spatio-Temporal Distortions

Approved by:

Rick Trebino, Advisor

Stephen E. Ralph

Donald C. O'Shea

Chandra Raman

John A. Buck

Date Approved: 7 July 2004

ACKNOWLEDGEMENTS

This thesis would not be possible without the help of many people. First of all, I would like to thank my advisor Rick Trebino, for his constant wise guidance through my graduate research, and for maintaining an open and interactive environment for me to thrive in. I would especially like to thank Mark Kimmel, who patiently taught me so much practical knowledge, without which a Ph.D. education would just not be complete. I would also like to thank fellow graduate students and postdocs in the lab: Aparna, Patrick, Erik, Lin, Selcuk, Pablo, Qiang, and the rest of the gang. You guys are such a great team to work with. And finally, I want to thank my parents for their love and support, and especially for encouraging me all along to pursue my own independent development. I love you.

TABLE OF CONTENTS

LIST OF TABLES

LIST OF FIGURES

SUMMARY

This thesis contains two components of research: studies of supercontinuum pulses generated in the novel microstructure fiber, and research on spatio-temporal coupling in ultrafast laser beams.

One of the most exciting developments in optics in recent years has been the invention of the microstructure optical fiber. By controlling the structural parameters of these novel fibers in design and manufacturing, their dispersion profile can be freely tailored, opening up a huge application base. One particularly interesting effect in the microstructure fiber is the generation of ultrabroadband supercontinuum with only nJ-level Ti:sapphire oscillator pulse pump. This supercontinuum is arguably the most complicated ultrafast pulse ever generated, with its huge time-bandwidth product (> 1000 from a 16-cm-long fiber). Although many applications have been demonstrated or envisioned with this continuum, its generation is a very complicated process that is poorly understood, and the characteristics of the continuum pulses are not clearly known. In this work, we make a full-intensity-and-phase measurement of the continuum pulses using cross-correlation frequency-resolved optical gating (XFROG). The results reveal surprising unstable fine spectral structure in the continuum pulses, which is confirmed by single-shot measurements. Our study on the coherence of the continuum, on the other hand, shows that the spectral phase of the supercontinuum is fairly stable. Numerical simulations are carried out whose results are in good agreement with experiments.

The second component of this thesis is the study of spatio-temporal coupling in ultrafast beams. We propose two definitions of spatial chirp, point out their respective physical meanings, and derive their relationship. On the common perception of the equivalence between pulse-front tilt and angular dispersion, we show that the equivalence only holds for plane waves. We establish a generalized theory of ultrafast laser beams with first-order spatio-temporal couplings, and discover a new pulse-front tilt effect associated with the

combination of spatial chirp and temporal chirp. For the measurement of spatio-temporal distortions, the effects of such distortions in the input beam to a GRENOUILLE trace are carefully studied. An algorithm is proposed and tested to retrieve information about the distortions from the GRENOUILLE trace.

CHAPTER 1

MICROSTRUCTURE OPTICAL FIBER

1.1 Optical Fibers

The impact of the optical fiber on the modern world can hardly be overstated. What began as some basic research experiments in the 1960s has evolved into a ubiquitous global technological foundation, which the world increasingly relies on.

Optical fibers are cylindrical dielectric waveguides, made of low-loss materials such as silica glass. Owing to advances in fabrication, loss in optical fibers can be made as low as ~ 0.15 dB/km, making optical fibers the blessed transmission medium for electromagnetic waves. Indeed, the loss is so low that, if the ocean were made of optical fiber glass, we would have no trouble at all seeing the bottom of the Mariana Trench, the deepest point in the world (10,924 meters below sea level), because the round-trip loss between there and the ocean surface would only be ~ 3.3 dB (44%).

An optical fiber consists of a central core of refractive index n_1, in which the light is guided, surrounded by an outer cladding of slightly lower refractive index n_2. Those light rays within the core that are incident on the core-cladding interface at angles greater than the critical angle $\theta_c = \sin^{-1}(n_2/n_1)$ undergo total internal reflection, and thus are guided without refraction loss into the cladding. Guided modes consists of these rays.

Conditions for the guided eigenmodes are quantized due to the boundary conditions on the core-cladding interface. Full analysis of the mode characteristics was given in many excellent papers in the 1970s and can be found in numerous textbooks [17, 96].

To present these results in an elegant way, we would define a set of normalized parameters:

Normalized transverse propagation/absorption constants

$$u = a\left(n_1^2 k_0^2 - \beta^2\right)^{1/2} \qquad \text{in core} \tag{1a}$$

$$w = a\left(\beta^2 - n_2^2 k_0^2\right)^{1/2} \qquad \text{in cladding} \tag{1b}$$

Normalized frequency parameter

$$V = \left(u^2 + w^2\right)^{1/2} = a k_0 \left(n_1^2 - n_2^2\right)^{1/2} \tag{2}$$

where $k_0 = \omega/c$ is the wavenumber in vacuum, $\beta = k_z$ is the z-component of the wavevector, or the propagation constant, and a is the radius of the core.

Using these normalized parameters, a complete set of eigenmodes can be derived.

The V parameter is an especially important and useful parameter in practical applications, because it determines the cutoff condition and the number of modes that can propagate in the fiber. If the V number of the fiber is less than 2.405, only the fundamental mode is allowed to propagate, in which case the fiber is called a single-mode fiber. A single-mode fiber is preferred in pulse applications, while multi-mode fibers are more suitable for power-delivery applications.

For telecommunication applications, dispersion in an optical fiber, apart from absorption, is the most important issue. Information is usually encoded onto a sequence of optical pulses, which is transmitted through the fiber to the other end. The accuracy of the transmission depends on the fidelity of pulse shape at the receiver's end. However, the faster the transmission rate is, the shorter the optical pulses need to be; and the shorter an optical pulse is, the more bandwidth, or frequency components, it contains. The major problem is that these frequency components, or colors, do not propagate at the same group velocity in the fiber. As a result, what comes into the fiber as a short optical pulse becomes longer and longer as it propagates, as different frequency components separate in time. Eventually, pulses representing different bits run into each other, causing inter-symbol interference (ISI) which ultimately undermines communication. This effect is minimized at the wavelength where group-velocity dispersion (GVD), defined as $\beta_2 = \dfrac{\mathrm{d}^2\beta}{\mathrm{d}\omega^2}$, is zero.

The total dispersion of a fiber consists of three contributions: material dispersion, which is intrinsic to the material itself; waveguide dispersion, which is due to the waveguide

characteristics of the fiber design; and modal dispersion, which results from the group-velocity differences between different guided modes in a multi-mode fiber.

For a single-mode fiber, modal dispersion does not exist, and the total dispersion consists of only the material and waveguide dispersion terms. The first term is determined by nature. Zero group-velocity dispersion occurs at around 1.3 μm for fiber silica, and doping hardly changes it at all. The second term, however, depends on the design of the fiber. Choosing different core size and/or index contrast can significantly modify the waveguide dispersion term, and even more interestingly, graded index profiles can be designed and fabricated, which allows fiber designers greater freedom to customize and fine-tune the dispersion curve. However, these designs all have fair limitations, with zero-dispersion wavelengths usually between 1.3 and 1.55 μm.

Pulses propagating in an optical fiber not only experience dispersion, but also induce nonlinear effects. Silica is an isotropic material, so second-harmonic generation cannot happen in a fiber as required by symmetry. However, other nonlinear optical effects, such as self-phase modulation, Raman scattering and Brillouin scattering do occur [2]. The magnitude of an nonlinear optical effect is directly related to the peak power of the pulse. In most fiber applications the nonlinear effects are usually modest, but become significant in state-of-the-art long-haul fiber communication systems, where dispersion can be very well compensated, but nonlinear effects cannot.

Nonlinear optical effects can interact with dispersion in an optical fiber, causing one peculiar and very useful effect—soliton. In the anomalous dispersion regime, self-phase modulation, the most important third-order nonlinear effect, can be balanced by the negative dispersion provided the pulse peak power is high enough. In that case, the pulse propagates either intact through the fiber without any shape change, which case is referred to as a fundamental soliton, or undergoes periodical pulse shape evolution in the case of a higher-order soliton. The soliton order number is the integer closest to [17]:

$$N = \left(\frac{\omega_0 n_2' P_0 T^2}{|\beta_2|\, c A_{\text{eff}}} \right)^{1/2} \tag{3}$$

where n_2' is the nonlinear refractive index, P_0 is the peak power of the pulse, A_{eff} is the

effective area of the fiber, and T is the pulse length.

If the peak power of the input pulse is very high, self-phase modulation can occur on a grand scale, significantly broadening the pulse spectrum. At the same time, the high power and broadened spectrum will trigger a variety of other nonlinear effects. These nonlinear effects along with dispersion interact in a very complicated manner, resulting in a very broad and continuous spectrum, which is called supercontinuum. Supercontinuum generation is a well-known effect in bulk materials with amplified ultrashort laser pulses, usually accompanied by undesired side effects such as small-scale self focusing and laser beam filamentation [15]. In optical fibers, supercontinuum generation can also be achieved with high power ultrashort pulses. In Chapter 6, we will discuss the supercontinuum generation in a dispersion-shifted fiber pumped by a 1.55-μm fiber laser, and the measurement of the continuum pulse.

Ultrafast optics is the study of ultrashort pulses, pulses that have lengths on the order of femtoseconds (10^{-15} s). To generate an ultrashort pulse, one needs a broad spectrum, and, the broader the spectrum is, the shorter a pulse can be potentially made. Such broad spectrum can be provided by supercontinuum generation. Besides making short pulses, supercontinuum has many other uses as well, some of which we will cover in Section 1.3.

Conventional fibers are ill-suited for supercontinuum generation. The most important issue is the mismatch between the fiber's zero-dispersion wavelength and the ultrafast laser's operating wavelength. The field of ultrafast optics predominantly uses the Ti:sapphire laser, which generates pulses ranging from a few to several hundred femtoseconds, with pulse energy typically on the order of nJ for an oscillator to mJ for an amplifier. The Ti:sapphire laser lases around 800 nm, a wavelength where an optical fiber has significant normal dispersion. At this wavelength, material dispersion of silica is so large ($\sim$ 100 ps/nm-km) that the waveguide dispersion of the fiber can essentially be neglected. Because of the massive dispersion, an ultrashort pulse entering the fiber quickly lengthens, and the peak power drops dramatically, before it has any chance of triggering significant nonlinear optical effects.

All of that would change with the invention of the microstructure fiber.

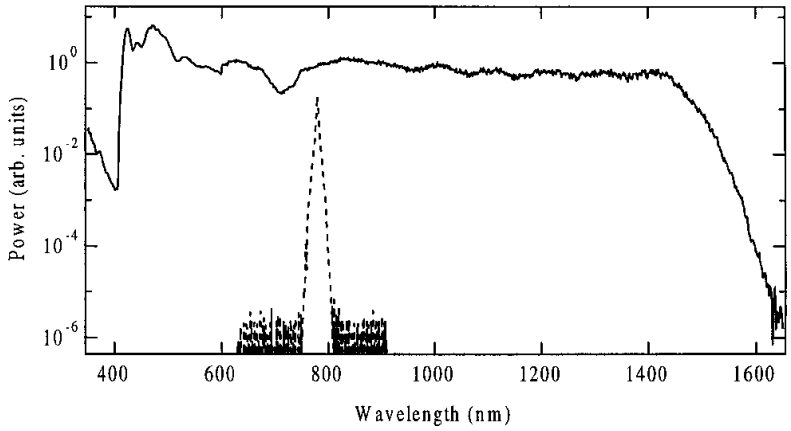

Figure 1: Supercontinuum spectrum generated from a 75-cm section of microstructure fiber, excerpted from Ref. [102].

1.2 Microstructure Fiber

A postdeadline talk at CLEO 1999 by Jinendra Ranka et al. [103] from Lucent Technologies set off a shockwave in the optics community. In this talk, Ranka et al. showed results of ultrabroadband supercontinuum generation in a special "microstructure fiber," with nJ-level Ti:sapphire oscillator pump pulses. The generated supercontinuum spanned from 400 nm to 1600 nm, covering almost two octaves (Figure 1), and the supercontinuum appeared single-mode, smooth, stable and flat (of which we will come to question in Chapter 3). Following the first demonstrations of the microstructure fiber by the Lucent group [102, 104] and the University of Bath group [77, 12] simultaneously, this novel fiber and the supercontinuum generation in it has become one of the hottest topics in the optics community. Today, a casual search on the key words "microstructure fiber" on the ISI Web of Science® website would yield more than 200 hits of journal papers, almost all written in the past three years, demonstrating the remarkable appeal of this new fiber to researchers.

The frenzy about the microstructure fiber is not at all unjustified. These novel fibers offer such abundant new possibilities that a whole field of research has emerged and numerous applications have resulted. One of the highest-profile applications is the construction of the world's most accurate optical clock in NIST [32, 33], with accuracy 1–2 orders of magnitude better than the world's current time standard, the Cs atomic clock. In this work, a

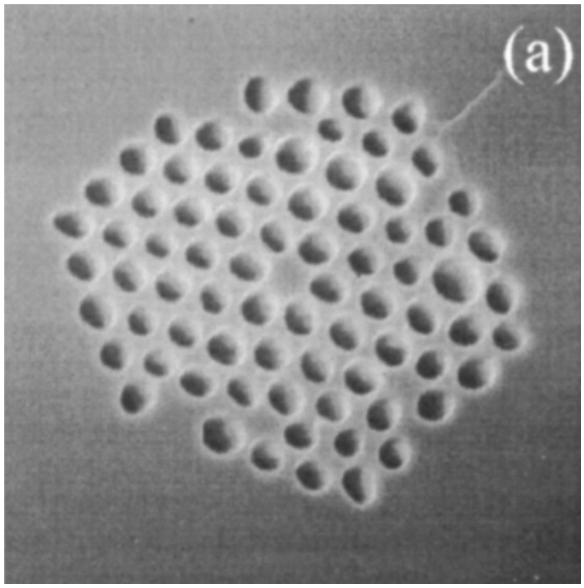

Figure 2: Cross-section electron micrograph of a microstructure fiber, excerpted from Ref. [104].

microstructure fiber generating an octave-spanning supercontinuum is the key component to its success.

Microstructure fibers, some of which are also known as photonic crystal fibers (PCFs), or holey fibers, are a class of fibers with microstructure, or a regular two-dimensional pattern of air holes (sometimes filled with dielectrics) fabricated (using a stack-and-draw method) in the fiber cross section (Figure 2). A defect, often just a missing hole, but occasionally a larger hole or even an extra hole in the microstructure array, forms a core in which light is guided.

In photonic crystal fibers, the regular air hole pattern forms a photonic crystal [71], a term indicative of the analogy between electrons in the periodic potential of a semiconductor crystal and photons in a periodic index profile. The mathematical treatments of the two cases are very similar, producing similar effects. In the semiconductor crystal, the key consequence of the well-known Bloch Theorem is the electronic bandgap between the valence band and the conduction band. In the bandgap, no electron energy levels are allowed. In the photonic crystal formed by the periodic index profile, the same Bloch Theorem also applies, mandating a *photonic bandgap*, in which no light propagation modes are allowed. Light having frequency or wavenumber in this bandgap is strongly confined and propagates only

in the core, because it cannot escape into the photonic crystal cladding as its propagation is forbidden there [79]. This concept made a new family of fibers possible, which were inconceivable by the conventional design principles five years ago. For example, light can be guided in the air core of a hollow-core photonic-crystal fiber without experiencing refraction loss into the cladding [26].

Not all two-dimensional periodic index structures exhibit photonic bandgap effects. It is worth pointing out that even without a photonic bandgap cladding, some microstructure fibers still guide light. Such fibers usually have a solid core, and the light guiding mechanism can be understood as follows: The microstructure cladding, being a mixture of silica and air, has a lower effective index than the solid core [78]. Total internal reflection, therefore, can still happen on the not-so-clearly-defined interface of the core and microstructure cladding, guiding light in the same principle as in ordinary fibers. It is often found that for such fibers, the full array of air holes are not really necessary for light guidance. If the fiber has only one or two innermost rings of air holes, the fiber would still function the same way. This effective index model and total internal reflection theory have proven quite satisfying for crude intuitive descriptions of such microstructure fibers, which are in very wide use today, especially for the purpose of supercontinuum generation. However, this first-order model is inadequate for the calculation of some important parameters such as dispersion. Full theoretical treatment of the microstructure fiber requires rigorous field analysis using the exact boundary conditions of the microstructure configuration. Such analysis applies regardless of the specifics of the light guiding mechanism or the complexity of the microstructure configuration. Several methods exist for the analysis, including the scalar beam propagation method [108, 75], the vectorial plane-wave expansion method [72, 66], the multipole method [125, 83], the finite-element method [28, 129], the radial scattering decomposition method [47], etc.

Numerical calculations using these methods are very successful, and are responsible for the huge number of new microstructure fiber designs that exhibit novel attractive properties and are becoming widely employed in all kinds of applications. These novel fibers include

the endless single-mode PCF [12], cobweb fiber [45], highly birefringent PCF [74], single-polarization single-mode PCF [106], polymer microstructure fiber [118], etc. Indeed, the types of microstructure fibers are so many that we cannot attempt to list them all here.

Microstructure fibers are interesting not only in their peculiar linear-optical waveguiding properties. They are much more interesting because of the significant nonlinear effects that happen in them. In fact, the efficiency of the nonlinear optical effects is directly related to the linear optical properties of the microstructure fiber, which we will discuss in detail in the next section. Many different nonlinear processes have been observed in the microstructure fiber, including self-phase modulation, third-harmonic generation, parametric four-wave mixing, stimulated Raman scattering, etc. Essentially, all nonlinear optical processes that can happen in an optical fiber have been seen in the microstructure fiber, and these processes happen on a *grand* scale. Most commonly, these nonlinear processes happen at the same time, working in concert to create an amazing ultrabroadband supercontinuum. As Ranka et al. showed in their CLEO postdeadline talk [103], the supercontinuum generated in their microstructure fiber had a bandwidth of over 1200 nm! Supercontinuum generation is no doubt the most talked-about property of the microstructure fiber. Numerous papers have been written on this subject which comprise a large part of the body of the microstructure fiber literature, and many applications are demonstrated or envisioned for this amazing supercontinuum. The large number of publications about the supercontinuum generation is also due to the complexity of the process. Understanding the supercontinuum generation has only been possible very recently, with significant advances in the numerical simulation techniques and experimental characterization work such as the research we did, which is the subject of Chapters 3–6. In the following section, we will show the theoretical origin of the supercontinuum generation, summarize the current understanding of the process, and present some examples of its practical applications.

1.3 Supercontinuum Generation in Microstructure Fiber

The microstructure fiber that has been shown to exhibit spectacular supercontinuum generation has a hexagonal air hole configuration as shown in Figure 2. The light is guided in

the solid core region by total internal reflection. The ratio of hole radius and microstructure array pitch is on the order of 1. Studies show that the electric field is tightly confined within the few innermost rings of air holes.

The efficient supercontinuum generation in the microstructure fiber can be attributed to two properties of the fiber. The first is quite obvious. The microstructure fiber has a core size of 1–2 μm, significantly smaller than that of conventional single-mode fibers. Because the guided mode is much more confined, the power density is much higher, so that the effective nonlinearity is enhanced.

The second and more important reason for the efficient supercontinuum generation is dispersion. Conventional fibers have very high normal dispersion at the Ti:sapphire wavelength of 800 nm. An ultrashort pulse entering the fiber quickly lengthens due to dispersion, diminishing any possibility for significant nonlinear effects to grow.

In a microstructure fiber, dispersion is remarkably modified by the microstructure configuration. Indeed, by choosing the proper fiber parameters such as air hole size and pitch, one can easily tailor the dispersion characteristics of the fiber, and shift the zero-GVD wavelength to 800 nm or even lower [76]. This remarkable dispersion customizability is largely due to the small core size, and the high index contrast between the solid core and the microstructure cladding, which is two orders of magnitude higher than the index contrast in conventional fibers.

Because of the low dispersion around 800 nm in the microstructure fiber, the input ultrashort pulse maintains its short duration and high peak power while it propagates in the first few millimeters. Consequently, the pulse spectrum is quickly broadened to an ultrabroadband supercontinuum by the many nonlinear optical processes that are triggered in the propagation. It is clear that the ultrabroadband supercontinuum is not the result of one or few individual nonlinear processes, but rather a complex interplay between the many nonlinear processes and the dispersion properties of the fiber. However, the dynamics of the supercontinuum generation process, including the role each nonlinear optical effect plays in the different stages of supercontinuum generation, and their effects on the characteristics of

the resulting supercontinuum, were not well understood. There were prevalent misconceptions about the continuum, which would have profound implications on its potential use. For example, since Ranka et al.'s first presentation, the supercontinuum spectrum had been perceived as smooth, stable and flat. Our characterization of the intensity and phase of the continuum pulse has shown that this perception is not true [60]. A detailed discussion on this issue is contained in Chapter 3.

Numerical simulation techniques for supercontinuum generation in the microstructure fiber have advanced tremendously in recent years. With the help of experimental measurements, the results of these theoretical calculations [39, 54] based on the nonlinear Schrödinger equation have helped people understand the process of supercontinuum generation much better, and have predicted properties of the supercontinuum which are nicely confirmed by experiments. It is worth pointing out that supercontinuum generation in the microstructure fiber is in principle no different from that in conventional fibers. The processes that happen in fibers have been known for many years in the fiber community. The only complexity is that the spectrum broadening is so fast and dramatic in the microstructure fiber, that the various terms of nonlinear interaction and dispersion quickly get mingled together, making the evolution of the pulse extremely complicated and hard to interpret. To correctly calculate the evolution of the supercontinuum pulse which has over 1000 nm of bandwidth, a huge number of data points need to be computed at very small propagation steps using the split-step Fourier transform method. Such numerical simulations have only been possible recently with improvements both in the numerical models and the computer technology.

Following the first publication of supercontinuum generation in the microstructure fiber [102], there have been intense debates in the community on the theoretical interpretation and the roles played by various nonlinear optical processes. Now, years later, with the results of rigorous numerical simulations and experimental evidence, the community appears to have reached a consensus. The current understanding can be summarized in the following manner:

It has become clear that the evolution of supercontinuum is closely related to the formation and evolution of solitons. If the input pulse is in the anomalous dispersion regime of the microstructure fiber, a higher-order soliton will form due to self-phase modulation, with the soliton order number N determined by Eq. (3). With a nJ-level ultrashort Ti:sapphire oscillator pulse, N can be greater than 10.

If the fiber had only linear dispersion (with no higher-order dispersion terms) and no other nonlinear processes, the N^{th}-order soliton would only propagate with periodic contraction and expansion, as is stated in the textbooks. However, group-velocity dispersion being low also means that the effect of higher-order dispersion cannot be neglected. It has been shown that the perturbation of higher-order dispersion would cause the splitting of the N^{th}-order soliton into N fundamental solitons, similar to the splitting of degenerate energy levels due to perturbation in quantum mechanics [67, 65]. Therefore, instead of the behavior of a non-perturbed higher-order soliton, which experiences periodical breakup and recombination, in the perturbed case, the higher-order soliton breaks up into a series of fundamental soliton pulses but these pulses never recombine completely.

If that were the whole story, the N fundamental solitons would separate in time, but they would still be at the same wavelength, so that the continuum spectrum would not be as broad as it is. However, as the spectrum gets broader due to self-phase modulation and the bandwidth becomes comparable to the Raman frequency shift, a phenomenon called the soliton self-frequency shift occurs [92, 24, 85]. This is an effect that, due to the preferential gain in the Stokes wave of the stimulated Raman scattering, energy in the blue side of the soliton spectrum gets downconverted to the red side, causing the solitons to continuously shift toward longer wavelengths. As a result, as a series of fundamental solitons are shed one by one from the input pulse, they also move toward longer wavelengths, resulting in a considerable spectral expansion into the red.

The interpretation of the development of the blue end of the supercontinuum, on the other hand, is less clear. There are still debates on the mechanisms responsible for the generation of the blue spectral components, and it appears that certain mechanisms are more important in some fibers than others. One major mechanism that has been recognized

for the blue component generation is the non-solitonic radiation, in which a soliton pulse, perturbed by higher-order dispersion, transfers energy into a phase-matched blue dispersive wave component satisfying a resonance condition [67, 65, 27]. This radiation process is mathematically equivalent to the Cherenkov radiation of electrons, and therefore, is often referred to by scientists as the Cherenkov radiation in optical fibers [3]. Owing to this process, as the fundamental solitons that are formed in soliton splitting move to longer wavelengths, corresponding blue dispersive wave components are developed and amplified. Consequently, an ultrabroadband supercontinuum is generated toward both ends of the spectrum. Experimental measurements strongly support this theory, with clear evidence of phase-matching relationship between the blue non-solitonic wavelengths and the soliton wavelengths, in good agreement with theoretical predictions.

Other processes have been suggested for the generation of blue spectral components in some microstructure fibers, including parametric four-wave mixing [1, 4, 22, 68, 109], third-harmonic generation [97, 43], and others. Their presence has also been supported by a number of experiments.

If the pump wavelength is in the normal dispersion regime of the microstructure fiber, a soliton is not formed immediately at the input. However, high peak power of the input pulse still induces significant self-phase modulation which broadens the pulse spectrum over into the anomalous dispersion regime, while the fiber's low dispersion keeps the peak intensity high. Afterwards, processes similar to those described above happen, and a narrower and less structured supercontinuum usually results.

It should be noted that the supercontinuum is generated in a short distance in the microstructure fiber. As is shown both by numerical simulations and experiments [18, 41], the full spectral width of the supercontinuum is typically achieved in the first few millimeters of the fiber. Afterwards, while no new frequencies are created, the individual solitons and their dispersive wave components keep separating in time as they propagate, causing increasingly fine interference features in the continuum spectrum [60, 58], which tend to vary from shot to shot. The unstable fine spectral structure is a problem in many applications. Using a very short microstructure fiber (< 1 cm) and/or careful choice of fiber or pump

pulse parameters may minimize the problem.

The microstructure fiber is not the only fiber that can generate supercontinuum with nJ-level Ti:sapphire pulses. In recent years, tapered glass fibers have also been fabricated. They have been demonstrated to generate supercontinuum in much the same way as microstructure fibers [11]. The tapered fiber is a conventional single-mode fiber adiabatically tapered to a radius of $\lesssim 1$ μm. In the tapered section, the original cladding and core collapse into one region, where light is guided, among a "cladding" of air. This fiber has similar properties as the microstructure fiber, for the index contrast is also high, and the core is small. Although the tapered fiber is easier to fabricate than the microstructure fiber, it is also extremely fragile and difficult to use. The practical applications of the tapered fiber are yet to be seen.

Supercontinuum generation in microstructure fibers has many applications. Most importantly, it is the most easily made ultrabroadband supercontinuum, with nice spatial and spectral coherence. After all, to generate the supercontinuum, one only needs a Ti:sapphire oscillator and a short piece of the microstructure fiber, and the quality of the generated supercontinuum is much better than the one generated in bulk media with amplifier pulses. The most publicized application is probably the construction of the NIST optical clock. Using the over-an-octave supercontinuum generated in the microstructure fiber, NIST scientists were able to lock the carrier-envelope phase of their laser system by locking the phase drift between the blue end of the supercontinuum spectrum and the second harmonic of the red end of the spectrum. Using the phase-locked laser, an optical clock of record precision was demonstrated. Other demonstrated applications of supercontinuum generation and nonlinear effects in the microstructure fiber in general include ultra-high-precision optical coherence tomography (OCT) [61, 121], quantum optics [48], optical switching [110], etc.

The study of the microstructure fiber and the supercontinuum generation therein still remains one of the hottest topics in the field. Many questions have yet to be answered or clarified. Future years will hopefully see a better understanding and wider application of this wonderful technological advance.

CHAPTER 2

FROG AND XFROG

Ultrashort laser pulses are the shortest events mankind has ever created. Pulses on the order of femtoseconds are now routinely generated in labs, and are widely used in fields like physics, chemistry and biology. It is very important to measure these pulses well.

To measure such short pulses is not easy. Indeed, to measure an event in time, you normally need a shorter event. But how do you measure the shortest event ever created?

The answer is, you will have to use the pulse itself. Early on, techniques that use this concept, such as the intensity autocorrelation [107, 126], were invented, which can give a crude, *very unreliable* estimation of the pulse length, but nothing more than that. Particularly, it is not only important to know how long the pulse is, or what colors are in the pulse, but it is also very important to know at what time a color occurs in a pulse, or equivalently, what colors are present at a certain time. That sort of information is crucial for the generation, manipulation and application of ultrashort laser pulses, but can only be obtained by using a full-intensity-and-phase pulse characterization technique.

Several such full characterization techniques were invented in the early 1990s, and their applications have truly revolutionized the field of ultrafast optics. Among these pulse measurement techniques, frequency-resolved optical gating (FROG) [115, 116] and spectral phase interferometry for direct electric-field reconstruction (SPIDER) [69] are the two most well-known and trusted techniques.

FROG is a technique based on the concept of spectrogram, a description of a complex pulse in the joint time-frequency domain [23]. A FROG trace completely determines the intensity and phase of a complex pulse, aside from a few trivial ambiguities that some implementations of the technique have but are easy to deal with. Retrieval of the pulse intensity and phase relies on an iterative algorithm, which is extremely robust against noise or system errors. Indeed, using this technique, one not only gets the pulse intensity and

phase, but also finds how reliable that information is.

SPIDER, on the other hand, uses the spectral interferogram of two frequency-upconverted copies of the pulse—each with a different time (and hence also spectral) slice of a linearly chirp pulse—to obtain information about the pulse's spectral phase. SPIDER requires a more complicated interferometer-based device, hence is difficult to align, but its pulse retrieval algorithm uses a direct inversion procedure, which is fast and easy. The greatest drawback of SPIDER is its lack of independent checks. In other words, while you always get a result with a SPIDER measurement, you are not guaranteed its correctness. The experimental apparatus is so complicated that the result can easily be corrupted by slight misalignment or inadequate device capability or anything else, and it's very hard to assess the quality of the measurement.

The supercontinuum generated from the microstructure fiber, as stated in the previous section, is arguably the most complicated pulse ever created. Its measurement is a great challenge for all pulse measurement techniques. It is virtually impossible to make such a measurement with SPIDER, let alone a convincing one. To accomplish this task, we have chosen FROG, particularly, a variation of FROG called cross-correlation FROG (XFROG) [84] in our effort. A couple of clever innovations were used to make this measurement possible, and the rather surprising results of this measurement are shown in Chapter 3.

In this chapter, we will cover the basics of the FROG and XFROG theory. Interested readers are referred to the FROG book authored by Rick Trebino [116].

2.1 Autocorrelation

To understand FROG, we will first consider its historical predecessor, the autocorrelation.

The invention of using autocorrelation to measure the pulse length was a very important development in the art of generating and manipulating ultrashort pulses [107, 126]. It had been the main technique of the field until being replaced by more sophisticated techniques such as FROG or SPIDER. Even as we speak today, many people still use autocorrelation in their research, although serious scientists should have adopted the better techniques instead.

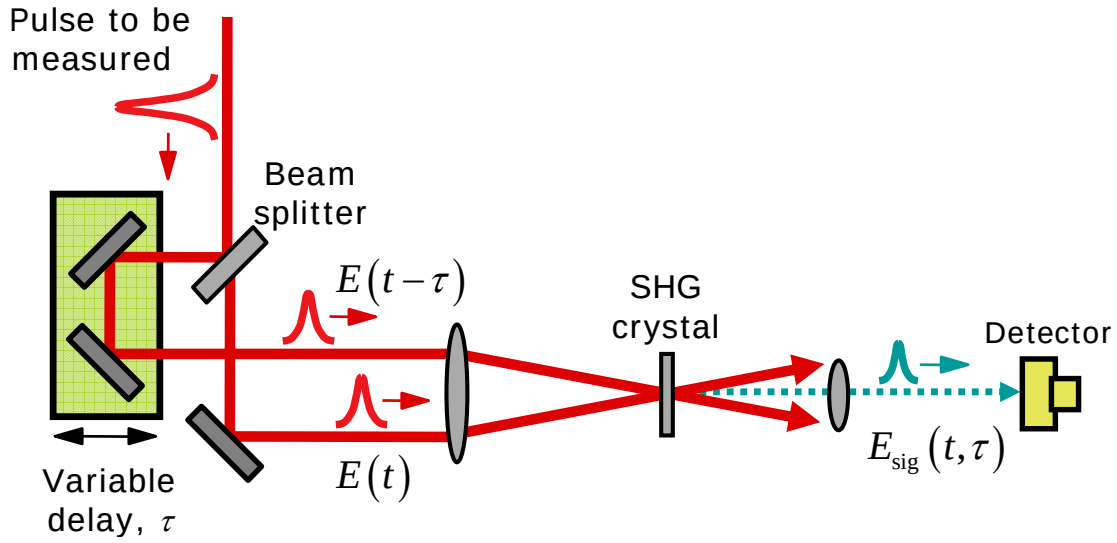

Figure 3: Schematic diagram of an SHG autocorrelator

In an autocorrelator, we need to create two copies of the pulse to be measured, either with a beamsplitter or a mirror. The two pulses, variably delayed with respect to one another, cross in a properly chosen nonlinear optical medium. A nonlinear optical signal will be generated when the two pulses overlap in space and time, and the magnitude of the signal depends on the extent of overlap. Normally in an autocorrelator, optimal spatial overlap is maintained throughout the measurement. The signal intensity is mapped out as a function of relative delay, from which an "autocorrelation width" is obtained. Assuming a certain pulse shape, the actual pulse width can be inferred from the autocorrelation width.

Mathematically, an SHG autocorrelation trace is

$$I_{\mathrm{AC}}(\tau) = \int_{-\infty}^{\infty} |E(t)\, E(t-\tau)|^2 \, \mathrm{d}t \tag{4}$$

The major problem of autocorrelation is that it does not uniquely determine the pulse characteristics. It cannot even accurately determine the pulse length, as to do that requires *a priori* information about the pulse shape, which in fact is impossible to obtain.

The deficiency of autocorrelation is fundamentally rooted in the fact that the amount of information contained in an autocorrelation trace is much less than the information in a pulse. To fully characterize a pulse, a total of $2N$ points, with N in intensity and N in

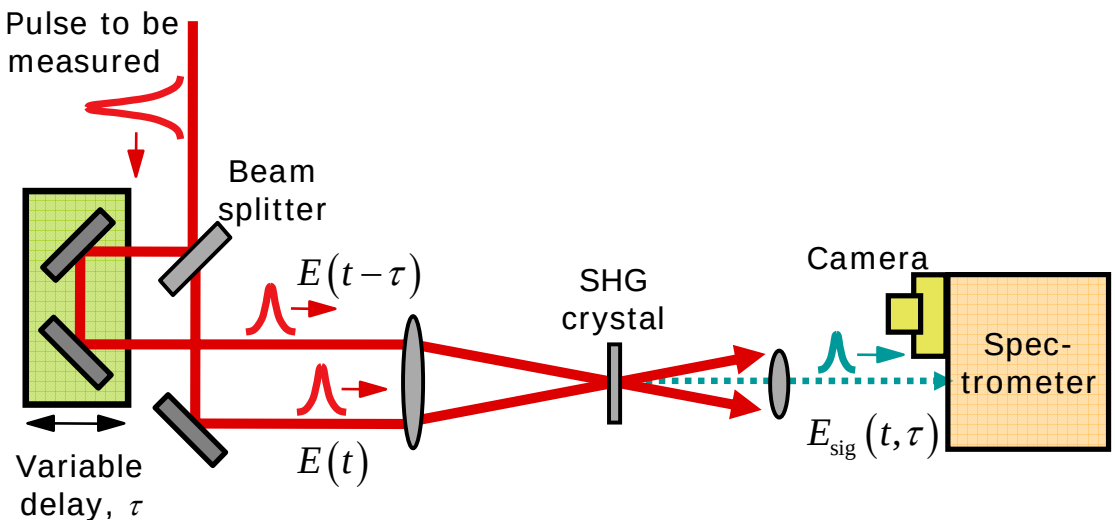

Figure 4: Schematic diagram of an SHG FROG apparatus

phase, need to be given. An autocorrelation trace only contains N data points—less inputs than the outputs, meaning the problem is quite underdetermined! Even with additional measurements such as the spectrum [100], autocorrelation still almost always fails. Recently, a very good analysis was given in Ref. [20] that showed pulses of vastly different shapes and lengths can produce very similar autocorrelation traces and power spectra.

Second-order intensity autocorrelation is not the only autocorrelation technique in use. There are some other autocorrelation techniques such as third-order autocorrelation [44], interferometric autocorrelation [34], etc. However, they all suffer from the same problem, and none are accepted ways of characterizing an ultrashort laser pulse.

2.2 FROG

Frequency-resolved optical gating, or FROG, was the first technique able to fully characterize a pulse, yielding not only its intensity, but also its phase [73].

From the experimental point of view, a FROG apparatus is only an autocorrelator followed by a spectrometer. Therefore, instead of just measuring the intensity of the nonlinear optical signal generated by the two variably delayed pulses, the nonlinear optical signal is now spectrally resolved into a delay-dependent spectrum. The resulting data is then a two-dimensional trace. If we use second-harmonic generation (SHG) as the nonlinear optical

process, the FROG trace is:

$$I_{\mathrm{FROG}}(\tau,\omega)=\left|\int E(t)\,E(t-\tau)\,e^{-i\omega t}\mathrm{d}t\right|^2 \tag{5}$$

Can the intensity and phase of a pulse be uniquely determined by its FROG trace? The answer is yes (save a few trivial ambiguities), and very interestingly, the proof is ultimately based on the Fundamental Theorem of Algebra, one of the most basic theorems of mathematics.

The problem of pulse characterization can be viewed as a phase retrieval problem, a well studied problem in the field of image processing. Using autocorrelation to determine a pulse is equivalent to retrieving the intensity and phase of a one-dimensional vector from the magnitude of its Fourier transform. Using a FROG trace to determine a pulse, on the other hand, is equivalent to retrieving the intensity and phase of a two-dimensional matrix from the magnitude of its two-dimensional Fourier transform.

What had been shown earlier in image processing is that with certain common constraints such as finite support, one-dimensional phase retrieval is fundamentally impossible, whereas two-dimensional phase retrieval is almost always possible [16]. The reason is, curiously, that for a one-variable polynomial, there exists the Fundamental Theorem of Algebra, but the same theorem does not hold for a two-variable polynomial. The full discussion of this interesting issue and its implication on phase retrieval is beyond the scope of this thesis. Detailed discussions can be found in Ref. [116].

Even though a FROG trace uniquely determines a pulse, the correspondence between a pulse's intensity and phase and its FROG trace is quite indirect and complicated. No direct inversion methods exist for retrieving a pulse from its FROG trace. Fortunately, numerical iterative algorithms work very well for this problem. Since its invention, FROG and its pulse retrieval algorithms have been used in many different labs and applications, whose success has testified the strength and reliability of the technique.

Not only can we uniquely determine the pulse from its FROG trace (save a few trivial ambiguities), we can do it extremely robustly. By making a FROG measurement, we obtain N^2 data points in the two-dimensional trace, but we only need to solve for $2N$ points for

the pulse intensity and phase. The problem has now moved from being underdetermined as in the case of autocorrelation to being overdetermined.

This data redundancy is a special strength of FROG, and indeed, the key to FROG's remarkable robustness. It is worth emphasizing that while every pulse corresponds to a unique FROG trace, not every two-dimensional trace corresponds to a physical pulse. The two-dimensional matrix space is so much larger than the one-dimensional complex-valued vector space, that it is only sparsely occupied by the FROG traces corresponding to possible physical pulses. When given an experimental FROG trace, which may be contaminated by noise or systematic error, the iterative retrieval algorithm always seeks to find the closest "physical" FROG trace to the experimental trace, and, by doing this, not only does it yield the best result, but also yields the accuracy of the measurement, which can be evaluated using the degree of resemblance between the experimental trace and the retrieved trace.

The data redundancy is not just a safety feature. At times, it yields information that is apparently missing from the original measurement, but is in fact still encoded in a different way in the FROG trace. A classic example is the FROG characterization of mode-locked semiconductor diode laser by Peter Delfyett et al. [29]. In that experiment, fine temporal structure in the FROG measurement was washed out due to insufficient temporal resolution. However, spectral bands in the trace contained adequate information for the iterative algorithm to retrieve the lost temporal structure. Subsequent finer-resolution measurements confirmed the existence of the retrieved temporal structure. In our measurement of the microstructure-fiber supercontinuum [60], we encountered a similar problem, and the redundant information in the measured trace also helped retrieve missing fine structure. Discussions on this interesting issue are in Chapter 3.

There are many variants of FROG, and they are all very useful. For example, we may use a variety of nonlinear optical processes in FROG, including second-harmonic generation [30], polarization gating [117], self diffraction [21], transient grating [112], etc. Also, both single-shot [126] and multi-shot versions of FROG are commonly used.

2.3 XFROG

FROG allows us to measure a pulse without a shorter reference pulse. Sometimes, however, a well-characterized reference pulse is available, often measured by FROG. In this case, we have the option to use the known reference pulse, which may greatly help our measurement.

One way to use a well-characterized reference pulse is spectral interferometry [53], which is a linear optical technique, and hence very sensitive. In combination with FROG, spectral interferometry (called TADPOLE [49] in this form) has measured pulses as weak as 42 zJ (1 zJ = 10^{-21} J), a record yet to beat. However, a key requirement to use spectral interferometry is that the reference pulse has to have equal or larger bandwidth than the pulse we want to measure, since spectral fringes only appear in the overlapped region of the spectra of the two pulses.

Obviously, spectral interferometry cannot be used to measure the microstructure-fiber supercontinuum. The continuum is so broadband that no reference pulse is available for its measurement. On the other hand, if we can characterize the continuum, it is conceivable to use it to characterize almost any other ultrafast pulses using spectral interferometry. In this sense, the microstructure-fiber supercontinuum can be regarded as a generic reference pulse, a truly exciting prospect. However, the hope of this use of the continuum was severely damaged when we revealed to the community its surprising fine and unstable spectral structure, which will be detailed in Chapter 3. The prospect is still not entirely dead, but we will at least need to resort to an extremely short microstructure fiber, which produces a more stable and less structured continuum. Such experiments can be a future direction of research.

The well-characterized reference pulse can also be used in the framework of FROG. This technique is known as the cross-correlation FROG, or XFROG [84]. In XFROG, rather than create two replicas of the unknown pulse, we take the unknown pulse and the reference pulse, and cross them in the nonlinear optical medium. The produced trace will then be a true spectrogram. Only minor modifications to the FROG algorithm are required to retrieve the pulse intensity and phase from the XFROG trace, while retaining all the nice features of FROG.

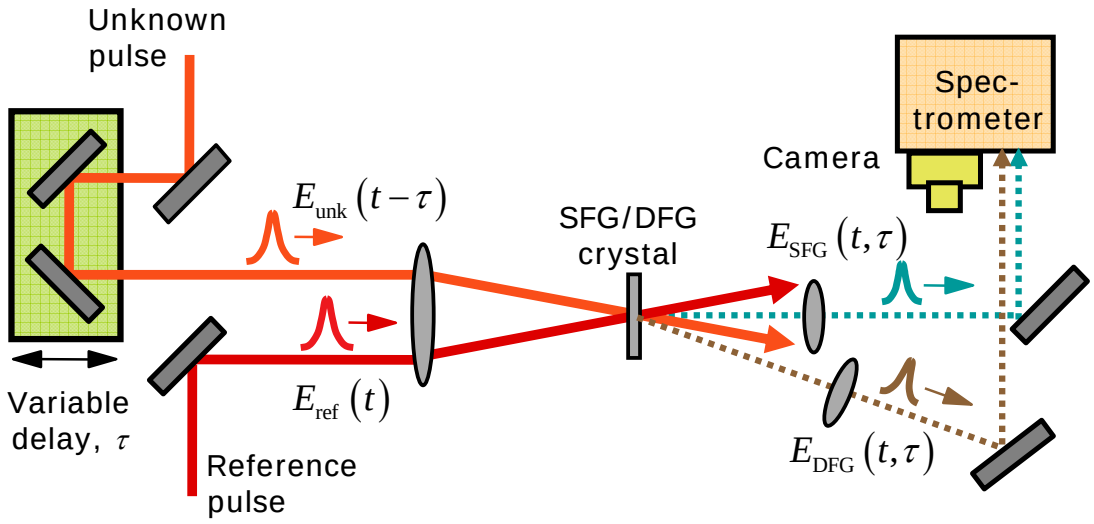

Figure 5: Schematic diagram of an SFG/DFG XFROG apparatus

XFROG is especially helpful when the unknown pulse is very weak. A weak pulse produces a much weaker nonlinear signal in FROG, even with the most sensitive nonlinear optical process—second-harmonic generation (SHG). The generated signal strength is proportional to the square of the unknown pulse $|E_{\mathrm{FROG}}| \propto |E_{\mathrm{unk}}|^2$. With XFROG, we have access to a reference pulse, which can be quite stronger. The same second-order nonlinear optical process, now known as sum-frequency generation (SFG) or difference-frequency generation (DFG), yields a nonlinear signal that is proportional to both the unknown pulse and the reference pulse $|E_{\mathrm{XFROG}}| \propto |E_{\mathrm{unk}} E_{\mathrm{ref}}|$.

Another advantage of XFROG comes from easy access to inconvenient wavelengths. For example, UV pulses with energies less than nJ levels are too weak to be measured with a third-order nonlinearity FROG technique. SHG FROG cannot be used either because SHG crystals are absorptive at the second harmonic wavelength of such pulses. Using XFROG, one can gate the UV pulse with a visible or infrared reference pulse, and the DFG process produces a signal pulse easy to measure at its wavelength.

Last but not least, an XFROG trace is also easier to interpret than a FROG trace. A FROG trace is produced by gating the pulse with itself. Both interacting pulses are, by definition, equally complicated. Although it's quite possible to read pulse information such as chirp directly from a FROG trace of a simple pulse, it is usually not straightforward

with a complicated pulse. And, because the two pulses are the same, SHG-FROG and other even-order FROG techniques suffer from a direction-of-time ambiguity, by which a positive and a negative chirp cannot be differentiated. An XFROG trace, on the other hand, is produced by gating the unknown pulse, with a known reference or gate pulse. The produced trace is a true spectrogram. If the reference pulse is short and simple, as is almost always the case, the XFROG trace can simply be read as a plot of frequency vs. time. A positively chirped pulse and a negatively chirped pulse have opposite slopes in their XFROG traces. The results of the XFROG retrieval algorithm—pulse intensity and phase—of course contain the full information of the pulse, and are more useful in numerical calculations. Nevertheless, one often finds that the XFROG trace itself is very intuitive and easy to interpret, which makes it an ideal tool for the representation and analysis of complicated pulses.

The microstructure-fiber supercontinuum is the most complicated pulse ever generated. Requiring only an oscillator pump, its pulse energy is on the order of nJ, and its bandwidth is huge! To use FROG to measure the continuum, an extremely thin SHG crystal has to be used, which would produce minuscule amount of signal. Although it's not entirely impossible, and may still be the only possible method to use in certain cases such as to measure a few-cycle continuum pulse after compression, using FROG to measure the microstructure-fiber continuum will be very difficult. XFROG, in comparison, is a better choice. In the next chapter, we will discuss the challenges we face in making the XFROG measurement of the microstructure-fiber continuum, describe our experiments and results, and discuss their implications.

CHAPTER 3

XFROG MEASUREMENT OF MICROSTRUCTURE-FIBER SUPERCONTINUUM

This chapter originally appeared as a paper by the author:

Xun Gu, Lin Xu, Mark Kimmel, Erik Zeek, Patrick O'Shea, Aparna P. Shreenath, Rick Trebino, and Robert S. Windeler, "Frequency-resolved optical gating and single-shot spectral measurements reveal fine structure in microstructure-fiber continuum," *Optics Letters* **27**, 1174–1176 (2002). [60]

3.1 Introduction

It has recently become possible to generate an ultrabroadband white-light continuum with a TEM_{00} spatial mode and a reportedly smooth and stable spectrum extending throughout the entire visible and near-IR regions of the spectrum by propagating sub-nanojoule 800-nm pulses through microstructure fiber [102].

As numerous far-reaching applications for this light are envisioned, it is crucial to measure the continuum as well as possible, especially its intensity and phase versus time. Such a measurement involves many complications, however. First, a multi-shot measurement requires that all the continuum pulses in the train be identical. Second, the nonlinear-optical process used to make the measurement must have a massive phase-matching bandwidth that exceeds that of the continuum. Third, while the precise time-bandwidth product (TBP) of the continuum is unknown, our measurements indicate that it is very large ($\sim$ 1000), making it the most complex ultrashort laser pulse ever generated. The most complex pulse ever measured previously had a TBP of about 10 [40].

In this chapter, we report preliminary multishot cross-correlation frequency-resolved-optical-gating (XFROG) measurements [84] of the continuum using a dithered-crystal technique. We find that the retrieved spectrum is not smooth or stable but instead contains fine

structure on a $\sim$ 1-nm scale, in disagreement with previous direct spectral measurements. Ordinarily such a discrepancy in retrieval would imply inadequacies in the more complex measurement, which in our case is the XFROG measurement. However, we performed single-shot measurements of the continuum spectrum, which also reveal $\sim$1-nm structure, in excellent qualitative agreement with the XFROG measurements. We also found that the continuum spectrum varies significantly from shot to shot, becoming smooth only in averages over several shots. While our multi-shot measurements of the continuum are thus inherently non-quantitative, they nevertheless provide much useful information, such as the continuum pulse length, approximate spectral phase, and the clue that the spectrum is in fact highly structured. Finally, it is interesting to speculate why our XFROG measurements—performed using more than 10^{11} shots—were able to see the spectral structure when simple spectral averages over as few as 100 pulses did not.

3.2 XFROG Measurement

We first discuss the phase-matching bandwidth, which scales inversely with the crystal thickness, while signal strength scales with the square of the thickness. In previous work, Baltuska et al. [8] measured 4.5-fs pulses with spectrum ranging from 600 to 1000 nm using second-harmonic-generation (SHG) FROG [115] with an extremely thin (10-μm-thick) β-barium borate (BBO) crystal. Thus, crystals considerably thinner than 10 μm would seem to be required to measure the much broader microstructure-fiber continuum. Such crystals are not available and, even if they were, would yield insufficient signal strength to actually make this measurement.

An SHG-based measurement of a pulse with wavelengths from 400 to 1600 nm generates wavelengths from 200 to 800 nm. Because crystal dispersion increases drastically near 200 nm, phased-matching these short wavelengths is especially problematic. This difficulty can be significantly reduced by performing XFROG, which uses sum-frequency generation (SFG) with a known potentially narrower-band gate pulse (here a $\sim$ 30-fs, 50-nm-bandwidth, 800-nm-wavelength pulse directly from a Ti:sapphire oscillator). SFG involving the continuum and the 800-nm gate pulse generates signal wavelengths from $\sim$ 260

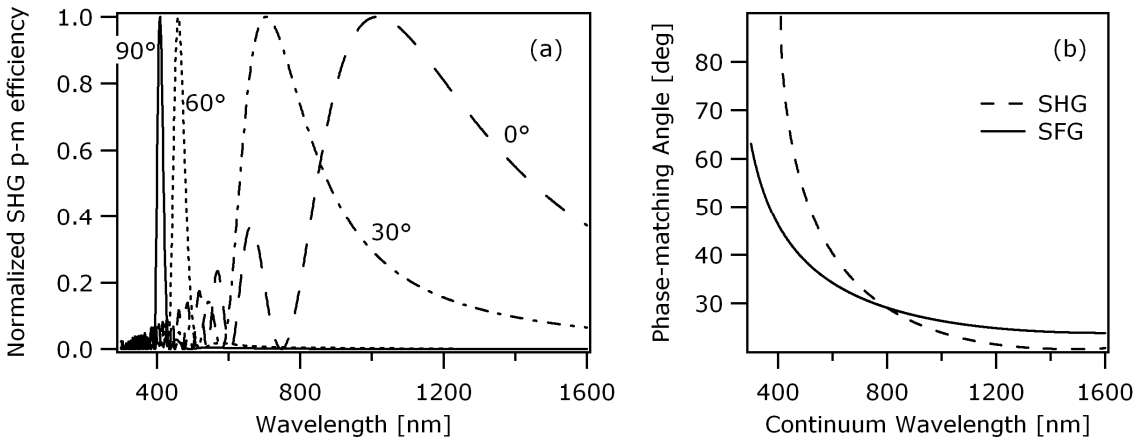

Figure 6: (a) Normalized SHG phase-matching efficiency of a 10-μm-thick BBO crystal for angles ranging from 0° to 90°; (b) phase-matching angle tuning curve for SHG and SFG with an 800-nm gate pulse.

to $\sim$ 550 nm, a considerably reduced signal-light bandwidth, which is, in fact, the more important quantity. Indeed, the required range of crystal phase-matching angles is much less (see Figure 6).

The use of XFROG helps, but, by itself, is not sufficient for performing this measurement. Fortunately, in recent work [98] we showed that, in a multi-shot measurement, it is in fact not necessary for the crystal phase-matching to achieve the full pulse bandwidth on every pulse; instead it is sufficient to do so over the measurement period—a much less strict condition. Because the crystal phase-matching angle varies with wavelength, angle-dithering a relatively thick crystal will increase the bandwidth of an (autocorrelator or) FROG.

We combined the dithered-crystal technique with XFROG to measure the continuum generated by sending $\sim$ 1 nJ of energy through 16 cm of microstructure fiber. We butt-coupled the microstructure fiber to a 3.4-μm-mode-field-diameter standard step-index fiber, reducing the full divergence angle of the continuum from $\sim$60° to $\sim$12°. Using a 40$\times$ reflective Cassegrain objective slightly off-axis, we achieved good-quality collimation.

Our apparatus is shown in Figure 7. We used a 1-mm-thick BBO crystal (whose group-velocity-dispersion-induced chirp is small compared to that of the continuum) that was rapidly angle-dithered by sim20°. The beam crossing angle was 2°, the delay increment

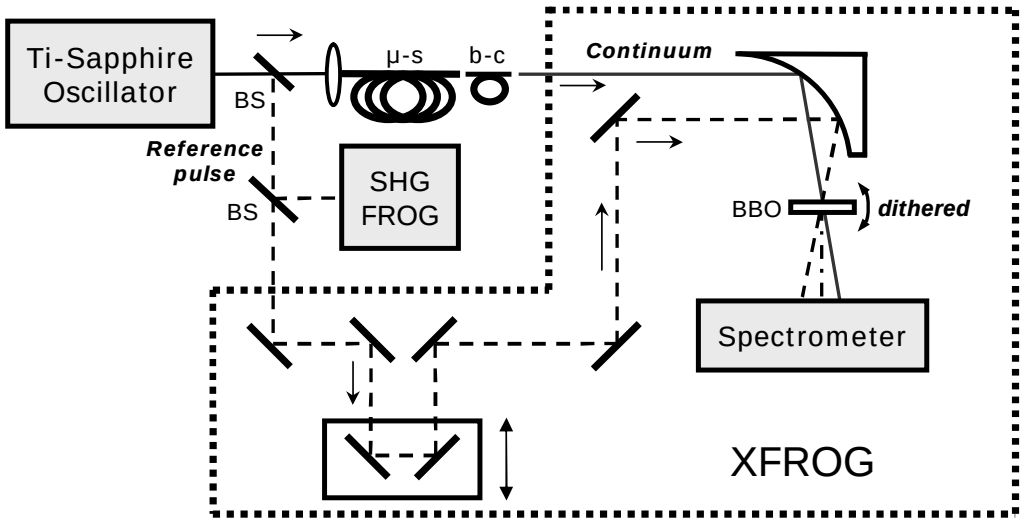

Figure 7: Schematic diagram of the multi-shot XFROG measurement apparatus. BS, beam-splitter; μ-s, microstructure fiber; b-c, butt-coupling fiber.

was 3 fs, the wavelength increment was 1 nm, and the wavelength resolution was less than 1 nm. Our measured trace had dimensions 3000×1024, which we interpolated and expanded to 8192×8192 for retrieval. We corrected traces for the wavelength dependence of phase-matching efficiency, taking into account such effects as phase-mismatch, nonlinearity dispersion, the ω-factor in Maxwell's equations, our crystal-angle dithering, and efficiency of the grating-camera system.

The measured XFROG trace is shown in Figure 8. The retrieved spectral phase was therefore mainly cubic, in agreement with the trace's parabolic shape. Although the retrieved spectrum has the same gross shape as the independently measured spectrum, we observe much fine-scale structure in the retrieved trace and spectrum that we did not see in the measured quantities, a clear indication that something is amiss.

3.3 Evidence of Unstable Fine Spectral Structure

In previous work measuring other light sources [29], retrieved FROG traces showed structure not present in measured traces, which was later revealed by subsequent measurements with improved resolution. With this knowledge, we have retaken XFROG measurements many times using ever-increasing array sizes and ever-better temporal and spectral resolution,

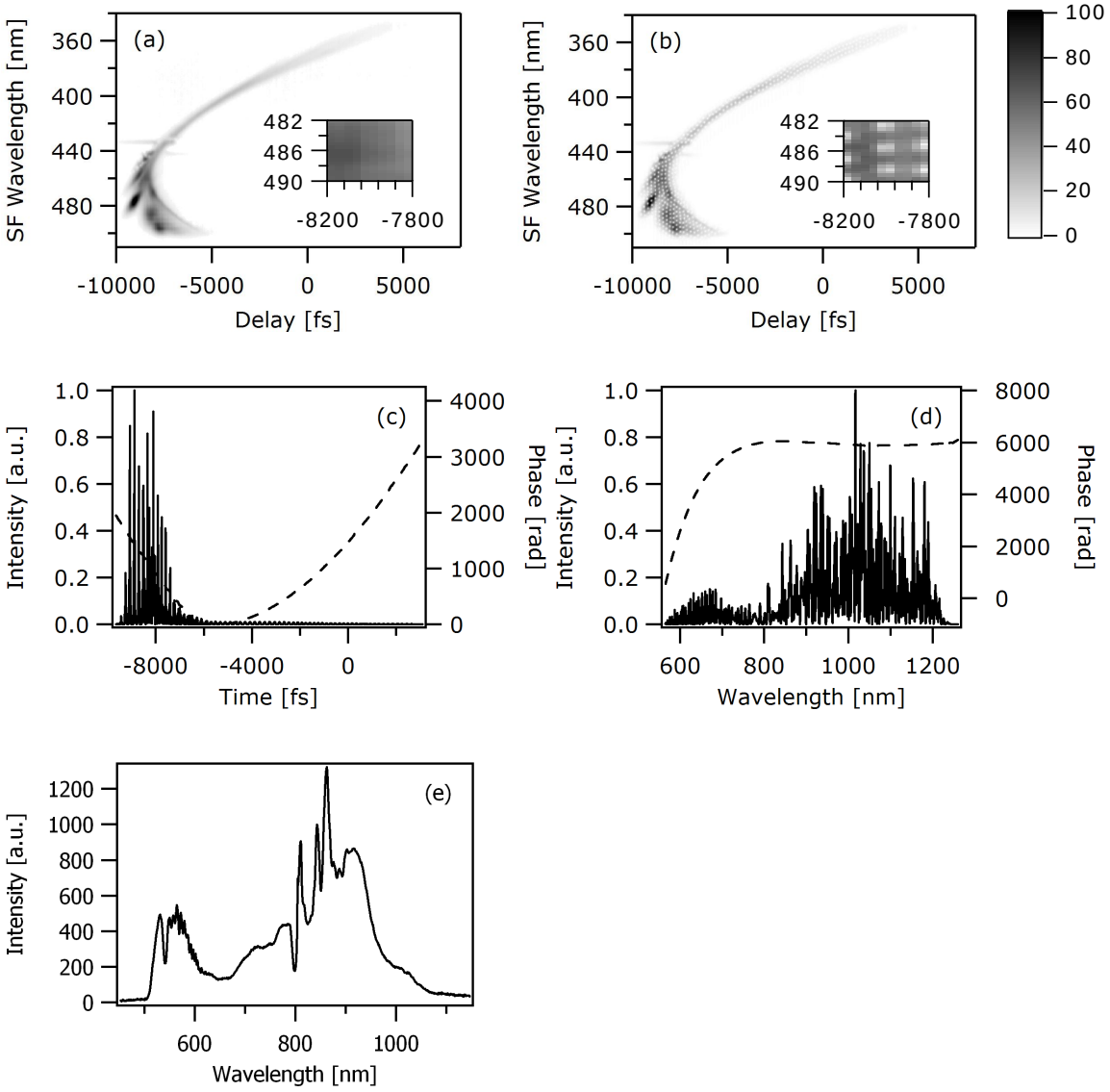

Figure 8: XFROG measurement of the microstructure-fiber continuum with an 800-nm 30-fs pre-characterized reference pulse: (a) measured trace, (b) retrieved trace, (c) retrieved temporal intensity (solid) and phase (dash), (d) retrieved spectral intensity (solid) and phase (dash), (e) independently measured spectrum. The XFROG error was 0.012. The insets in plots (a) and (b) are higher-resolution sections in the traces. Both traces are 8096×8096 in dimension. SF, sum frequency.

culminating in the measurements reported here, and we continue to observe fine-scale ($\sim$ 1 nm) structure in the retrieved trace and retrieved spectrum.

A possible explanation for these observations is that variations in the continuum pulse from shot to shot wash out the structure in directly measured spectra and in measured XFROG traces. That the information on the spectral structure remains in the multi-shot XFROG trace is possible because FROG traces contain much redundancy, and information washed out in one domain may remain in the other. Specifically, fine-scale frequency information is also present in the trace in the form of slow oscillations in delay, which are less likely to wash out. Specifically, fine-scale frequency information is also present in the trace in the form of slow oscillations in delay, which are less likely to wash out.

To test this hypothesis, we performed the first single-shot spectral measurements of the microstructure-fiber continuum. The output pulse from a Ti:sapphire oscillator was amplified by an adjustable-repetition-rate regenerative amplifier to $\sim$ 100 μJ per pulse, which was then attenuated to $\sim$ 1 nJ for input into 152 cm of 2-μm-diameter microstructure fiber from OFS Fitel Laboratories. Using different amplifier repetition rates and camera exposure times, we could vary the number of shots in a measurement (see Figure 9).

Figure 9 shows a 120-nm section of the continuum from 490 to 610 nm, with resolution of about 1 nm. Note that the fewer shots, the more spectral structure. Finally, the single-shot spectrum exhibits deep and fine oscillations, and each single-shot spectrum is different. If we manually take an average of just four successive single-shot spectra [Figure 9(e)], the oscillation amplitude decreases greatly, and the spectrum approaches those averaged over many shots. Shot-to-shot energy jitter in our amplified pulses was about 1%.

Theoretical simulations also confirmed our hypothesis (see Figure 10). Using a cubic spectral phase and a smooth super-Gaussian spectrum, we generated a smooth parabolic XFROG trace [Figures 10(a)–10(c)]. Imposing 100% multiplicative random noise on the spectrum, however, yielded a pulse with much structure in its trace [Figures 10(d)–10(h)]. The XFROG algorithm retrieves both the smooth and the structured spectra from their respective traces. Averaging 100 such structured traces washed out the structure and generated an artificially smoothed trace, similar to what we measure in a multi-shot experiment

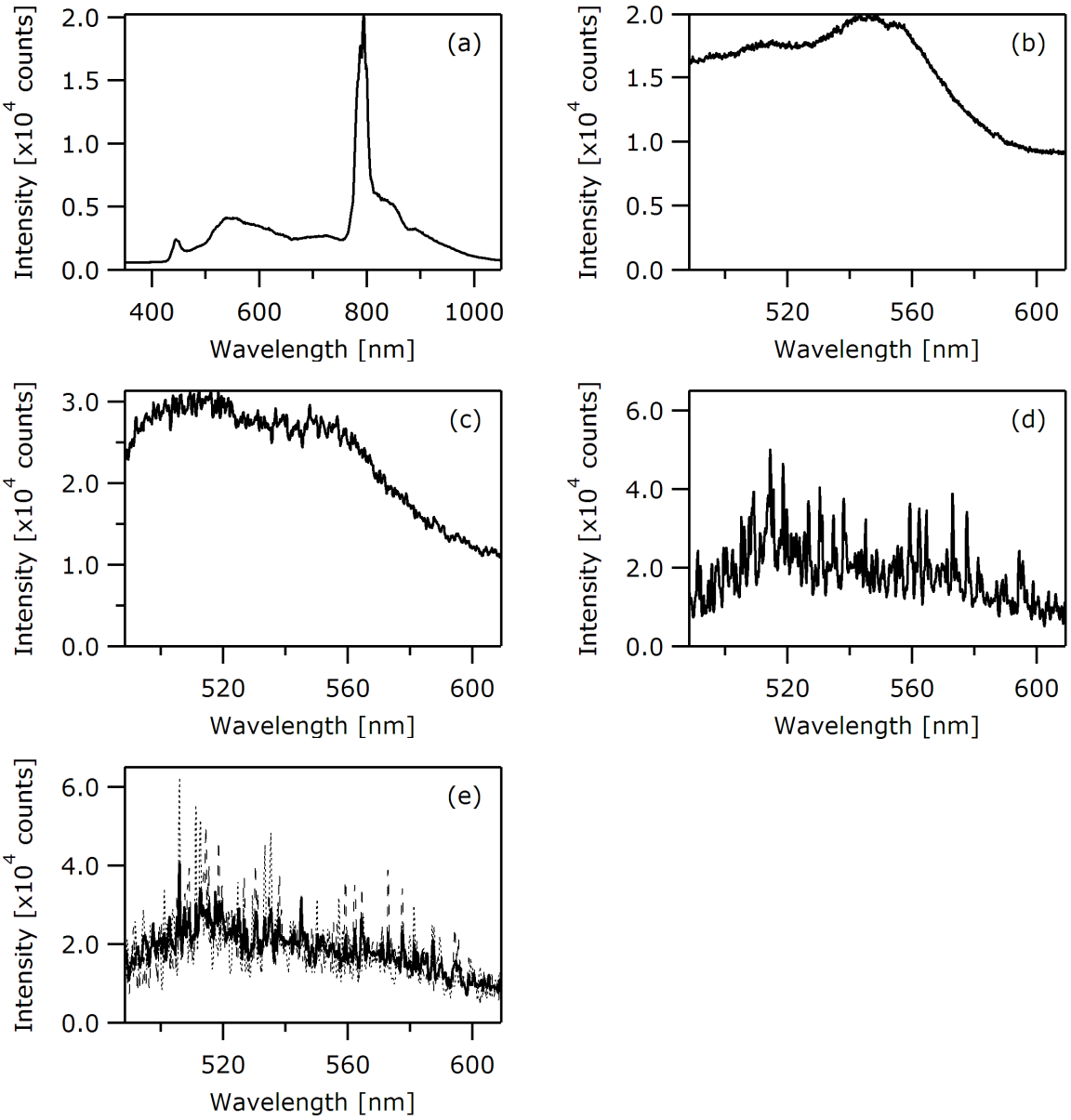

Figure 9: Continuum spectrum with various number of shots: Entire spectrum of the continuum (a) averaged over 10,000 pulses, and spectral sections of the continuum exposed for (b) 10,000 shots, (c) 100 shots, and (d) a single shot. (e) Numerical average of single-shot measurements taken successively; dashed and dotted curves are two single-shot spectra taken seconds apart, and the solid curve is the average of four single-shot spectra. Our measured single-shot spectra contained $\sim 2 \times 10^5$ photons per pixel, so shot noise was negligible in these measurements. Averaged spectra were attenuated; single-shot spectra were not.

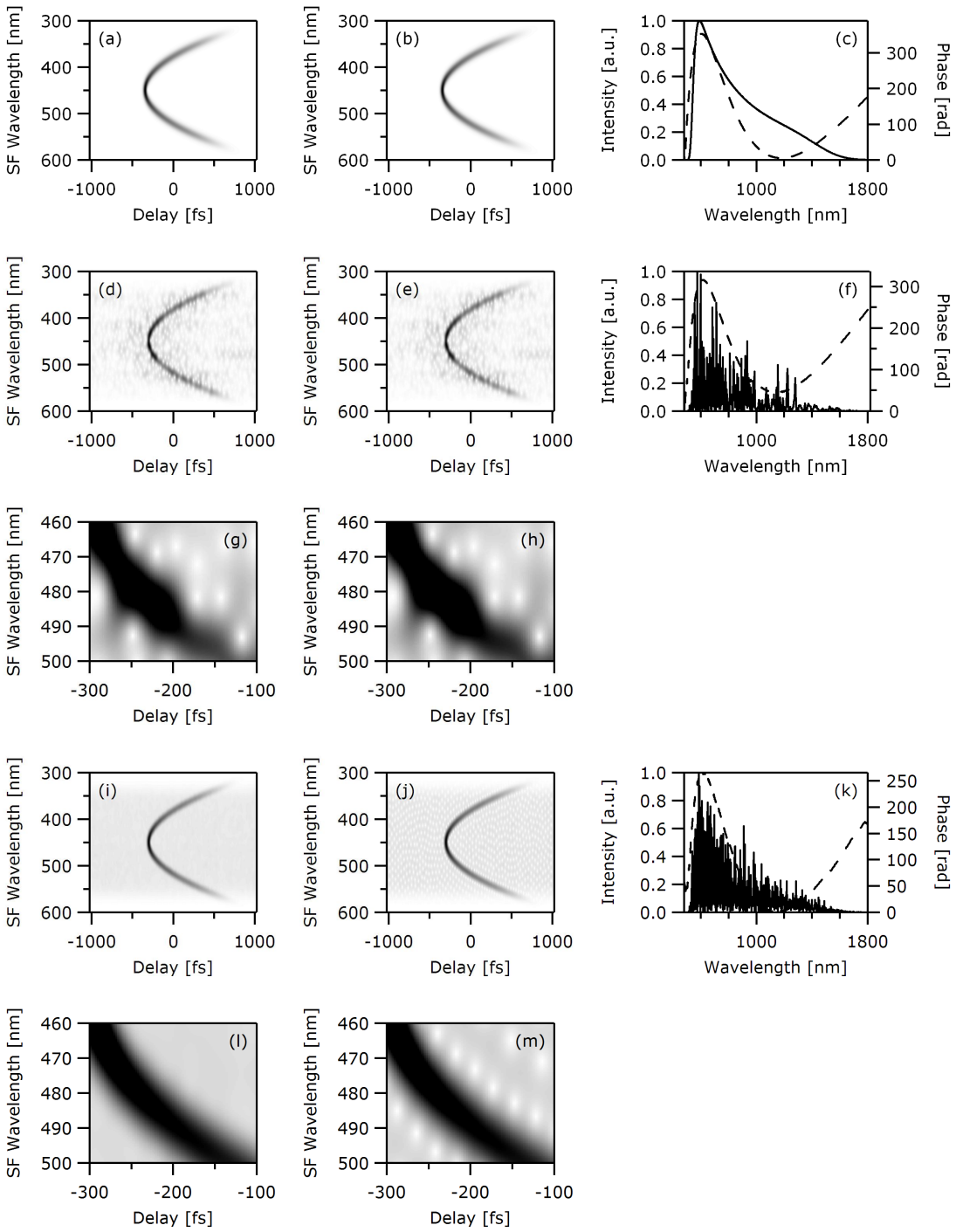

Figure 10: Simulations: (a) Theoretically generated, (b) retrieved XFROG traces, and (c) retrieved spectral intensity and phase of a pulse of a smooth super-Gaussian spectrum and cubic spectral phase, XFROG error 0.00015. (d) Theoretically generated, (e) retrieved XFROG traces, and (f) retrieved spectral intensity and phase of a pulse with a structured spectrum and cubic spectral phase, XFROG error 0.00031. (i) Average of 100 such structured traces, (j) retrieved XFROG trace, and (k) retrieved spectral intensity and phase from trace (i), XFROG error 0.0027. Plots (g), (h), (l) and (m) are higher-resolution sections in traces (d), (e), (i) and (j) respectively. All the traces are 1024×1024 in dimension.

[Figures 10(i) and 10(l)]. Retrieval on the smoothed-out trace not only preserved the gross shape of the trace, but also placed the fine structure back into the spectrum and the trace [Figures 10(j), 10(k), and 10(m)]. Also interesting to note is that the spectral phase was well retrieved, whether we started from a smooth, a structured or an artificially smoothed trace. This simulation imitates the real experiment and strongly supports our hypothesis.

Theoretical simulations of continuum generation have also predicted a deep and fine structure in the continuum spectrum [54, 39]. These simulations also predict large variations from very small fractional input power changes, also in agreement with our XFROG measurements.

We conclude that, because any single continuum pulse spectrum is highly structured, any measured smooth multi-shot spectrum—from even the most stable unamplified oscillator—must have involved averaging over widely different highly structured individual spectra. However, the retrieved spectral phase appears to be relatively stable, consistent with the coherence measurements of Bellini and Hänsch on bulk-media continuum generation [10]. It will be interesting to see the implications of these variations on continuum applications.

This research was supported by a Georgia Tech start-up grant from the Georgia Research Alliance and by National Science Foundation grant 9988706.

We thank Jinendra Ranka and Andrew J. Stentz for assistance with microstructure fibers and Alex Gaeta and John Dudley for help conversations. X. Gu's email address is xg7@prism.gatech.edu.

CHAPTER 4

COHERENCE PROPERTIES OF MICROSTRUCTURE-FIBER SUPERCONTINUUM

This chapter originally appeared as a paper by the author:

Xun Gu, Mark Kimmel, Aparna P. Shreenath, Rick Trebino, John M. Dudley, Stéphane Coen, and Robert S. Windeler, "Experimental studies of the coherence of microstructure-fiber supercontinuum," *Optics Express* **11**, 2697-2703 (2003). [57]

The numerical simulations contained in this chapter were performed by John Dudley and coworkers. The experiments were carried out in Georgia Tech.

4.1 Introduction

Supercontinuum (SC) generation in microstructure fiber has now been reported under a variety of experimental conditions, and has found particularly important applications in optical frequency metrology [31]. Although SC generation is complex, several studies have now identified the dominant spectral broadening mechanisms, providing insight into the stability (or the lack thereof) of the generated SC [67, 54, 38]. Numerical simulations, in particular, have shown that SC generation can exhibit extreme sensitivity to input pulse noise, leading to both shot-to-shot intensity fluctuations which can wash out spectral fine structure and shot-to-shot phase fluctuations that degrade the SC coherence [54, 38]. These predictions were confirmed experimentally by frequency-resolved optical gating (FROG) and single-shot spectral measurements [60], and by using RF noise analysis to measure both the relative intensity noise [52, 25] and the long-term carrier-envelope phase coherence [51].

The SC coherence can also be conveniently quantified by interfering together independently generated SC in a Young's two source type experiment. This technique, first reported by Bellini and Hänsch in the context of SC generation in bulk media [10], has also recently been used to quantify the relative coherence of independently seeded optical parametric

amplifiers [9]. In this paper, we report the first use of this method to characterize the coherence of microstructure fiber SC by interfering together two SC generated in different fiber segments, and in particular, we carry out a quantitative analysis of the resulting interferogram that allows the wavelength dependence of the mutual degree of coherence to be determined. A comparison with stochastic nonlinear Schrödinger equation (NLSE) simulations shows that the observed coherence degradation is consistent with fluctuations in the injected peak power significantly higher than the quantum limit. The significance of measuring the mutual coherence function is that it is the most natural measure of the phase coherence of light, and that experiments sensitive to phase stability will, in general, depend on it in some way. For SC generation, it provides an extremely useful measure of the sensitivity of the spectral broadening processes to input pulse noise, allowing the optimization of experimental design to ensure coherent SC generation.

Our experiments used a 90 MHz repetition rate KM Labs Ti:sapphire laser generating transform-limited 60 fs pulses at 800 nm. The pulses were injected into Lucent Technologies microstructure fiber with zero-dispersion wavelength $\sim$ 770 nm [102]. Before using the Bellini-Hänsch technique for coherence measurements, a preliminary study of the SC phase stability was performed using a straightforward spectral interference experiment between a typical microstructure-fiber-generated SC, and a picked-off fraction of the laser pump pulses. Figure 11 shows these results for an 18-cm fiber length and an injected pulse energy of 1 nJ. Distinct interference fringes are observed in the overlap region of the two spectra, suggesting that some coherence with the pump pulses is maintained during the SC generation process.

The presence of this residual pump-SC coherence is *a priori* surprising, as both numerical simulations of SC generation and spectral broadening in both microstructure fiber [54, 38] and standard fibers [93] have shown strong coherence degradation due to the amplification of input pulse noise. Moreover, cross-correlation FROG measurements of microstructure fiber SC generation have also shown strong shot-to-shot instabilities [60]. In this context, however, we note that the numerical studies in Refs. [54, 38, 25] have shown that the robustness of the SC generation process to input pulse noise (and hence the output SC coherence) depends strongly on the input pulse parameters, and the use of sub-100 fs pulses

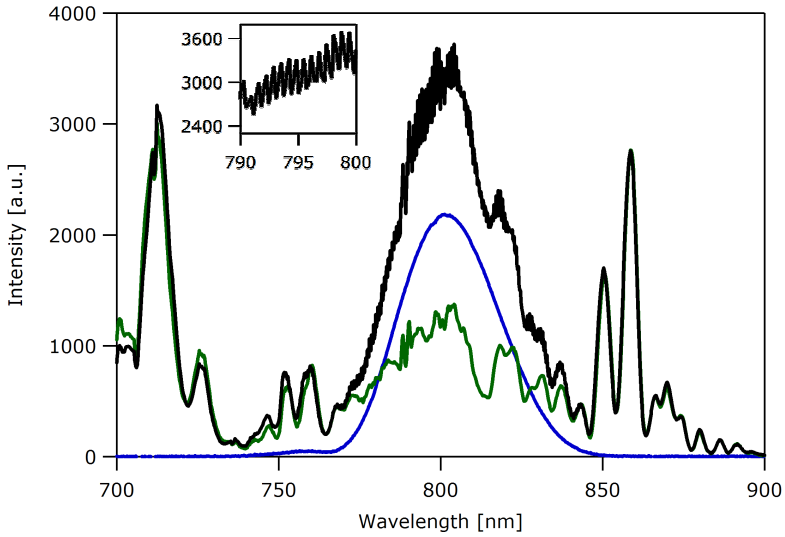

Figure 11: Spectral interference of a generated SC with the Ti:sapphire pump pulse. Shown in the plot are the spectra of: the microstructure-fiber SC (dotted line), the Ti:sapphire output (dashed line), and the interference spectrum of the two (solid line). The inset shows an expanded section of the interference spectrum around 795 nm.

would be expected to preserve some degree of spectral phase coherence even in the presence of significant spectral broadening. The residual coherence measured here using 60-fs pulses is consistent with these numerical results.

As has been discussed in detail in Refs. [38, 25], the dependence of the supercontinuum coherence on the input pulse duration can be understood physically in terms of the interplay between the spectral broadening processes associated with soliton fission [65] and modulational instability or four wave mixing [82]. With pulses injected in the anomalous dispersion regime, the initial pulse is viewed as a higher-order soliton that splits into individual fundamental solitons at different center wavelengths. However, because modulational instability gain amplifies any fluctuations present on the input pulse envelope, this process is extremely sensitive to the presence of any input pulse noise. The degree of sensitivity depends on the distance scale over which soliton fission occurs: for shorter pulses where fission occurs over a shorter propagation distance, modulational instability gain (which scales as the product of peak power and length) does not play as significant a role in perturbing the pulse break-up process and thus the resulting broadband spectrum exhibits higher intensity stability and

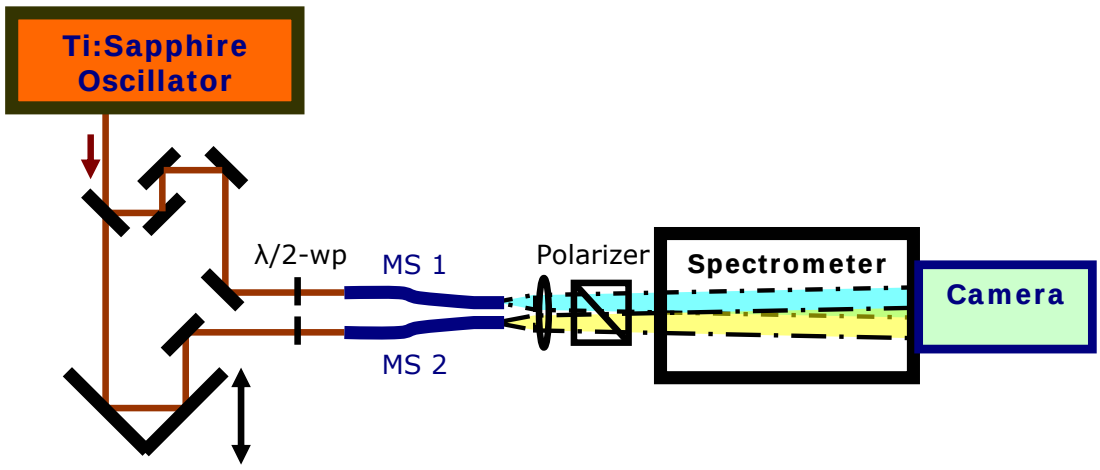

Figure 12: Schematic diagram of the Young's double-slit-type setup.

phase coherence. This can also be understood by considering that, for injected pulses with the same energy but different durations, shorter input pulses are associated with a lower soliton number so that the degree of soliton fission and hence the sensitivity to input pulse noise is lower.

4.2 Bellini-Hänsch-Type Experiment

To study the SC coherence more quantitatively, the Bellini-Hänsch technique was implemented using the setup in Figure 12. The Ti:sapphire output was split into two pulse trains which were injected along parallel polarization eigen-axes of two separate 18-cm fiber segments to yield independently generated SC with similar characteristics. The fiber output ends were secured next to each other in the same mounting slot of a fiber chuck. The SC were then collimated by a microscope objective and passed through a linear polarizer. (Although the SC was $> 80\%$ linearly polarized, the use of a polarizer facilitates optimal comparison with the scalar simulations described below.) The objective was adjusted so that the beams expanded and overlapped at the entrance slit of a spectrometer. A slice of the overlapped beams entered the spectrometer, and the spectra at all points along the slit were recorded by a two-dimensional camera at the spectrometer exit plane, which averaged for 20 ms (1.8×10^6 pulses). The two beams were aligned so that the interference fringes

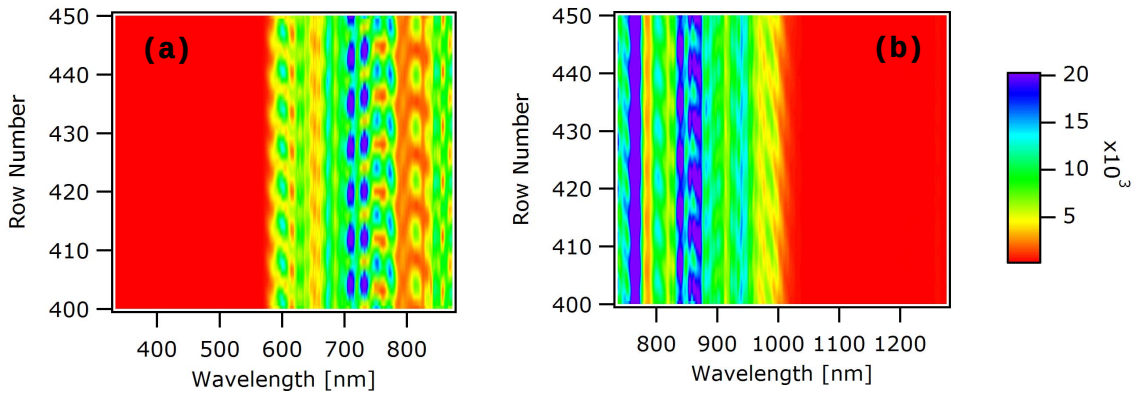

Figure 13: Measured spatially resolved interferograms for (a) shorter- and (b) longer-wavelength sections of the SC.

were across the direction of the slit, parallel to the direction of spectral dispersion, and readily observable on the camera. The relative delay was minimized. Because of the large SC bandwidth, it was necessary to record separate interferograms over wavelength ranges 350–850 nm and 800–1500 nm, and these results are presented separately in Figure 13(a) and 13(b). Well-defined interference fringes are clearly seen in the overlapped region of the two beams, indicating coherence over a wide range of wavelengths. The wavelength-dependent fringe visibility $V(\lambda)$ can be easily extracted from the interferograms and, together with the measured individual SC spectra $I_1(\lambda)$ and $I_2(\lambda)$, one can calculate the magnitude of the degree of first order mutual coherence as a function of wavelength using: $\left|g_{12}^{(1)}(\lambda)\right| = \frac{V(\lambda)\left[I_1(\lambda)+I_2(\lambda)\right]}{2\left[I_1(\lambda)\,I_2(\lambda)\right]^{1/2}}$. Note that the calculation of $\left|g_{12}^{(1)}(\lambda)\right|$ naturally includes differences in the interfering SC intensities, relaxing the (in-practice difficult) experimental constraint of equal injected pulse energies. Here, and elsewhere in this paper, all coherence and visibility measurements are calculated at zero relative delay between the two fields. Also note that, although the visibility was measured over 570–1020 nm, calculations of the coherence were restricted to the range 630–910 nm where the individual SC intensities were sufficiently above the measurement noise floor that unphysical artifacts could be avoided.

Figure 14(a) shows the results of this analysis. Here, the top two panels show the visibility and the corresponding calculated degree of coherence, and the bottom panel shows

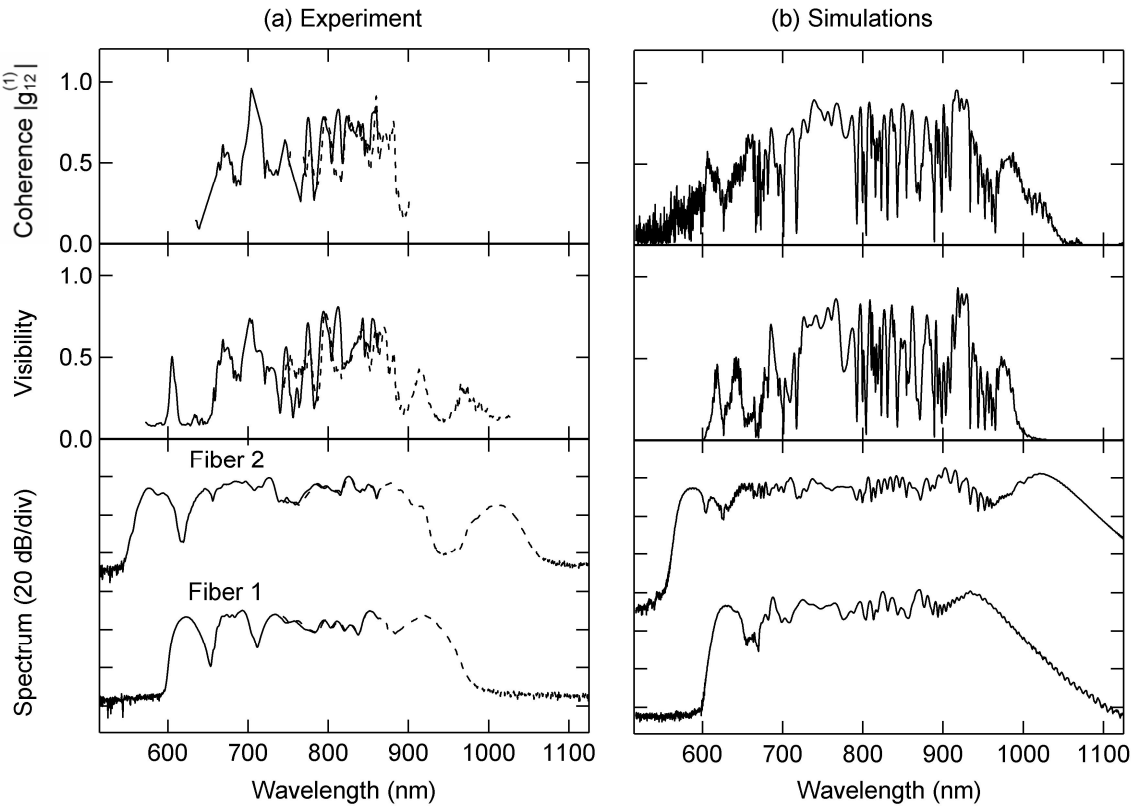

Figure 14: Coherence measurement and simulation results (a): experimentally measured SC spectra from each fiber (bottom), the visibility extracted from the interferogram between the two SC (middle) and the corresponding calculated degree of coherence (top). (b): corresponding results from simulations.

the independently measured SC spectra. The solid and dashed lines correspond to measurements over the shorter and longer wavelength ranges of the SC as shown in Figures 13(a) and 13(b) respectively. The visibility and degree of coherence are both high (~ 0.8) in the vicinity of the pump wavelength, confirming the spectral interference experiments described above. Away from the pump wavelength, however, a complicated wavelength dependent structure is present in both curves, and both the visibility and the coherence clearly decrease. We have found it useful to quantify these results in terms of the median visibility and degree of coherence, which we calculate to be 0.30 and 0.56 respectively. Significantly, the fact that the median degree of coherence is higher than the median visibility suggests that it is not only the loss of phase coherence which contributes to the loss of visibility, but also the fact that we were unable to generate identical SC spectra in our experiments (which was expected, in view of the spectrum's extreme dependence on the various system parameters), so that there are differences in the interfering intensities at each wavelength. From a practical viewpoint, the median degree of coherence can be interpreted physically as providing a measure of the suitability of the SC generated under different conditions for metrology or stabilization purposes.

4.3 Numerical Simulations

To interpret the experiments further, we used a stochastic NLSE model which rigorously includes input pulse and Raman noise during propagation [37]:

$$\begin{aligned}\frac{\partial E(z,t)}{\partial z} = i\sum_{k\geq 2}\frac{i^k\beta_k}{k!}\frac{\partial^k E}{\partial t^k} + i\gamma\left(1+\frac{i}{\omega_0}\frac{\partial}{\partial t}\right) \\ \times\left[E(z,t)\left(\int_{-\infty}^{t} R(t')\left|E(z,t-t')\right|^2 \mathrm{d}t' + i\Gamma_{\mathrm{R}}(z,t)\right)\right]\end{aligned} \tag{6}$$

Here $E(z,t)$ is the pulse envelope in a co-moving frame, the β_k's describe the fiber dispersion over 300–2000 nm, and the nonlinear coefficient $\gamma = 85\ \mathrm{W^{-1}km^{-1}}$ at 800 nm. The function $R(t) = (1-f_{\mathrm{R}})\,\delta(t) + f_{\mathrm{R}}h_{\mathrm{R}}(t)$ includes instantaneous and delayed Raman contributions with the fractional Raman contribution $f_{\mathrm{R}} = 0.18$. For h_{R}, we used the measured Raman response of silica. Spontaneous Raman noise appears as the stochastic

variable Γ_{R} which has frequency domain correlations given by:

$$\left|\left\langle \Gamma_{\mathrm{R}}\left(\Omega,z\right)\Gamma_{\mathrm{R}}^{*}\left(\Omega',z'\right)\right\rangle\right|=\frac{2f_{\mathrm{R}}\hbar\omega_{0}}{\gamma}\left|\mathrm{Im}\,h_{\mathrm{R}}\left(\Omega\right)\right|\left[n_{\mathrm{th}}\left(\left|\Omega\right|\right)+U\left(-\Omega\right)\right]\delta\left(z-z'\right)\delta\left(\Omega-\Omega'\right) \tag{7}$$

where the thermal Bose distribution $n_{\mathrm{th}}\left(\left|\Omega\right|\right)=\left[\exp\left(\hbar\Omega/k_{\mathrm{B}}T\right)-1\right]^{-1}$ and U is the Heaviside step function. The initial conditions are those of the measured pulse duration and chirp, with the addition of quantum-limited shot noise and technical noise as described below. The input pulse duration was 60 fs, and the injected pulse energies were 0.25 nJ for fiber 1 and 0.58 nJ for fiber 2, corresponding to experiments. The simulations were used to generate an ensemble of independent SC pairs $[E_1(\lambda), E_2(\lambda)]$ with different random noise seeds. From this, it is possible to calculate both the first-order coherence $g_{12}^{(1)}\left(\lambda\right)=\dfrac{\left|\left\langle E_{1}^{*}\left(\lambda\right)E_{2}\left(\lambda\right)\right\rangle\right|}{\left[\left\langle \left|E_{1}\left(\lambda\right)\right|^{2}\right\rangle\left\langle \left|E_{2}\left(\lambda\right)\right|^{2}\right\rangle\right]^{1/2}}$ as well as the corresponding fringe visibility (taking into account the different mean intensities).

Assuming shot-noise-limited input pulses in each fiber, no significant coherence degradation was observed in the simulations, with $\left|g_{12}^{(1)}\left(\lambda\right)\right|\approx 1$ at all wavelengths. This is consistent with earlier simulations [54, 38], and suggests that the observed coherence degradation in our experiments arises from other noise sources. The level of this additional noise was estimated from simulations using a simple numerical noise model based on injected peak power fluctuations, and adjusting the noise magnitude so that coherence degradation comparable to that in experiments was observed. Figure 14(b) shows simulation results assuming an input pulse noise level of 2%. Firstly, we note that the simulated mean spectra are in qualitative agreement with experiment, reproducing well the overall spectral width and the major spectral peaks at both extremes of the SC. Secondly, we see that the addition of this additional noise leads to significant coherence degradation, with median visibility and coherence of 0.35 and 0.64 respectively (calculated over the same wavelength ranges as in experiment). These results are in good agreement with experiment. Although no detailed studies were carried out to study the physical origin of this noise in more detail, additional experiments measured the level of technical injection noise at typically 0.4%. This suggests that other noise effects, possibly due to polarization instabilities also play an important role

in the coherence degradation. A quantitative study of these effects, however, will require the development of a fully vectorial stochastic NLSE.

In conclusion, we have shown that the Bellini-Hänsch technique has successfully allowed the first quantitative measurement of the wavelength-dependent spectral phase coherence of SC generated in microstructure fiber. Although shot-noise-limited 60-fs input pulses would be expected to yield a high degree of coherence across the entire SC spectrum, we experimentally observe significantly higher coherence degradation which exhibits strong wavelength dependence. Additional simulations allow us to estimate the magnitude of the additional noise present in the experiments as being consistent with 2% intensity fluctuations. Subsequently, we have been able to show that injection instabilties alone do not account for this level of fluctuation, suggesting that the decoherence effects most likely arise from a propagation-related instability. Since our numerical model is based on a scalar nonlinear Schrödinger equation, this suggests polarization-related effects as the most likely source of instability. Further investigations of such noise sources and their influence on the coherence will require a systematic study using the same Bellini-Hänsch method employed in this paper, under a variety of conditions, including different fiber lengths, pump power levels, fiber orientations and input polarizations. Nevertheless, the stochastic NLSE simulations have reproduced well the measured mutual degree of coherence assuming 2% fluctuations in the injected peak power, and these results suggest that the generation of coherent SC will require particular care in the stabilization of the pump laser and the mechanical fiber injection conditions. With the assumption of stabilized shot-noise-limited input pulses, additional numerical studies suggest that highly coherent SC (median degree of coherence > 0.95) can be readily obtained using pulses of duration 50 fs or less, and indeed we note that this is the pulse duration range which has been used successfully for stabilization purposes [52, 51].

CHAPTER 5

STUDIES OF FINE SPECTRAL STRUCTURE IN MICROSTRUCTURE-FIBER SUPERCONTINUUM

This chapter originally appeared as a conference paper by the author:

Xun Gu, Faisal Ahmad, Alexander L. Gaeta, Rick Trebino, and Robert S. Windeler, Fine spectral features in single-shot microstructure-fiber continuum, presented at the Conference on Laser and Eletro-Optics (CLEO), Baltimore, MD, June 1–6, 2003. [58]

Supercontinuum generation in newly developed microstructure fibers [102] is exciting and is finding many applications. It was recently discovered [60, 54] that the spectrum of the ultrabroadband light is neither smooth nor stable, as was believed from previous measurements. Indeed, the supercontinuum spectrum is full of deep fine features, which are extremely sensitive to pump conditions. Very small shot-to-shot input pulse variations cause the fine spectral features to shift, and over many shots (typically $> 10^6$ with a Ti:sapphire oscillator), they average out, leaving only a smooth envelope.

These unstable fine spectral features have many implications for applications of the microstructure-fiber continuum. In our experiments that first revealed these spectral features, the spectrometer had a resolution of ~ 1 nm, the same scale as the observed spectral structure [60]. Whether there is finer structure, what the structure is at different wavelengths, how stable it is, and how the structure evolves in the microstructure fiber are the subject of this study.

We used a regenerative Ti:sapphire amplifier system and attenuated its output to pump the microstructure fiber and generate white-light continuum. The repetition rate of the amplifier output was reduced so that single-shot spectra could be measured. A half-meter spectrometer with a 1200 groove/mm grating was used, yielding a resolution of 0.09 nm.

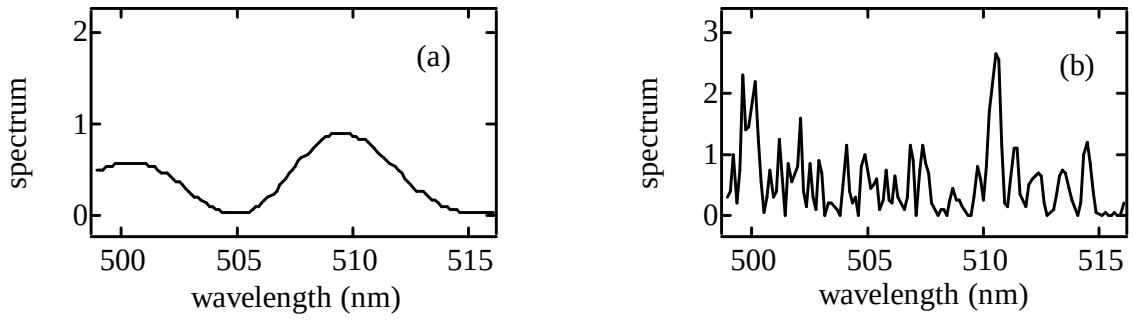

Figure 15: (a) Theoretically predicted continuum spectrum near 500 nm for (a) 1 cm and (b) 10 cm interaction lengths.

Three lengths of microstructure fiber were used in this study: 8 mm, 52 mm and 115 mm, and the results are shown in Table 1.

It is interesting to note that significant and complex differences exist in the fine spectral features of the continua generated with the three different lengths, although the widths of all the spectra are similar. At the blue end of the spectrum (500 and 600 nm), all three continua have unstable spectral features, and it is clear that the features get finer as the continuum pulse propagates along the fiber. From 500 to 700 nm, the scale of spectral features increases in 52-mm-fiber and 115-mm-fiber continua, and in the 8-mm-fiber continuum, there are also deeper 1-nm-scale modulations on top of the envelope. At 900 and 950 nm, the 8-mm-fiber continuum contains similar fine-scale features, although the intensity varies. In the 52-mm-fiber and the 120-mm-fiber continua, greater shot-to-shot variations are seen.

These varying features clearly indicate that although the envelope of the continuum reaches its full width after only a few millimeters of propagation in the microstructure fiber, additional processes other than dispersion are responsible for the fine structure of the continuum. Our numerical simulations indicate that it is due to the generation of multiple solitons at different wavelengths which, as a result of third-order dispersion, travel with different group velocities down the fiber. The separation in time between the pulses increases with propagation distance and results in finer and finer structure in the spectral domain (see Figure 15). Not surprisingly, for relatively long propagation distances this temporal separation is extremely sensitive to input pulse energy resulting in the highly

Table 1: Single-shot spectra of supercontinuum generated in microstructure fibers of lengths 8 mm, 52 mm and 115 mm respectively. Plotted in each figure are ten single-shot spectra measured consecutively from the microstructure fiber of given length.

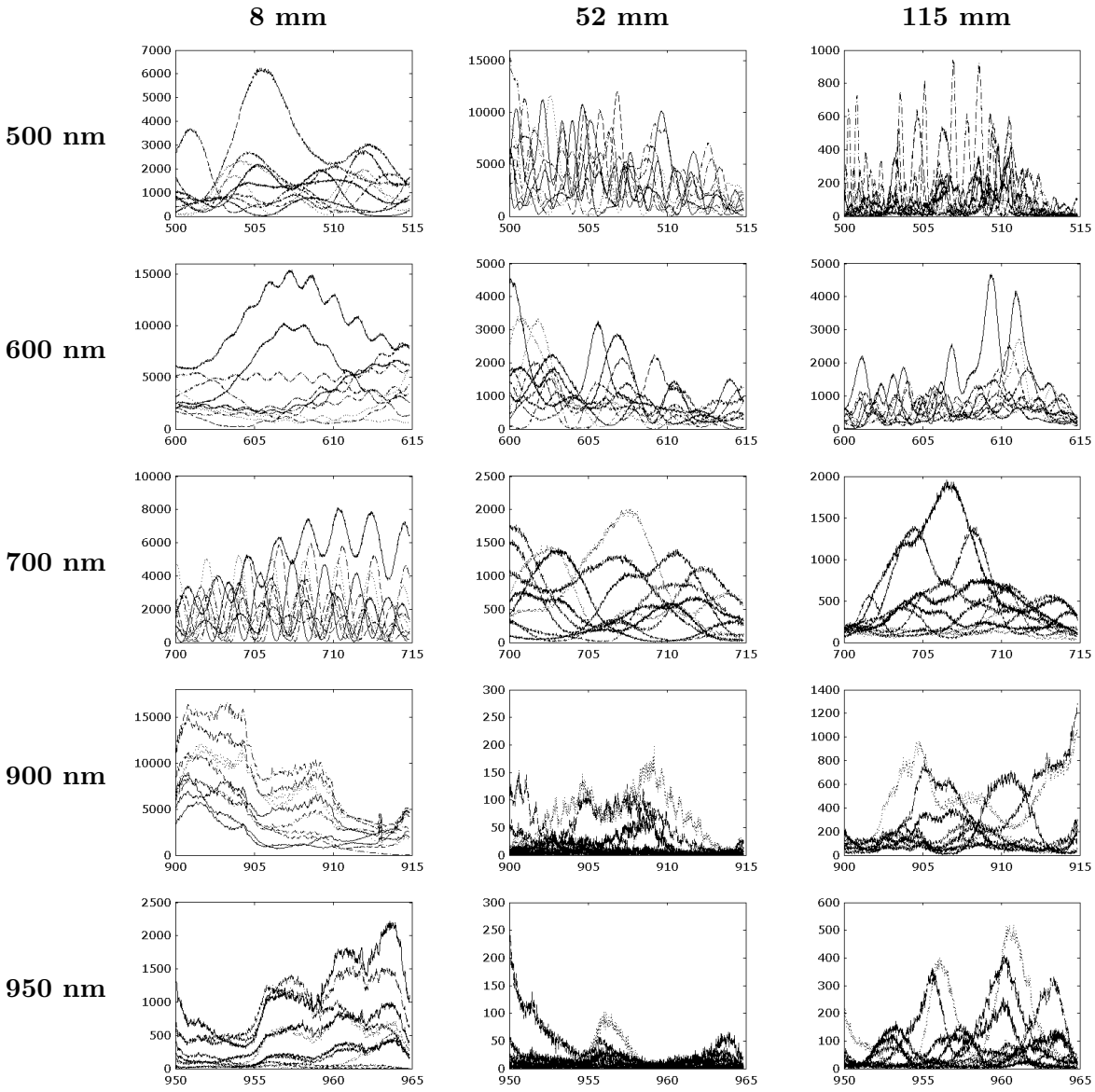

sensitive nature of the spectral sub-structure. These results argue for the use of shorter fiber for better-controlled experiments. Future single-shot FROG measurements should even better elucidate the physics of this complex light and the processes that create it.

CHAPTER 6

XFROG MEASUREMENT OF INFRARED SUPERCONTINUUM GENERATED IN CONVENTIONAL FIBER

This chapter originally appeared as a conference paper by the author:

Lin Xu, Xun Gu, Mark Kimmel, Patrick O'Shea, Rick Trebino, and Almantas Galvanauskas, "Ultra-broadband IR continuum generation and its phase measurement using cross-correlation FROG," presented at the Conference on Lasers and Electro-Optics (CLEO), Baltimore, MD, May 6–11, 2001. [127]

Ultrashort laser pulse technology plays an important role in the fields of physics, chemistry, biology, etc. The shorter the pulse, the faster the time scales that become accessible. More importantly, the broad bandwidths of such pulses, whether the pulses are short or not, are useful for many applications, including communication, coherent control of chemical reaction, ultrahigh-spatial-resolution optical coherence tomography, and optical metrology. Various approaches have been used to generate such broadband light, and continuum generation has been particularly successful, currently holding the record for the shortest event ever created in the visible–near IR spectral region [8]. In this paper, we report fairly flat-spectrum ultra-broadband IR continuum generation extending from 880 to 2400 nm using a high-energy 1550 nm pulse from a fiber oscillator/amplifier system [46], coupled into a standard fiber for continuum generation. Using cross-correlation frequency-resolved optical gating (XFROG) with an angle-dithered nonlinear crystal, we measured the continuum intensity and phase.

Like the continuum from microstructure optical fiber, this continuum is also single transverse mode and more than an octave in spectral width. But the IR continuum has

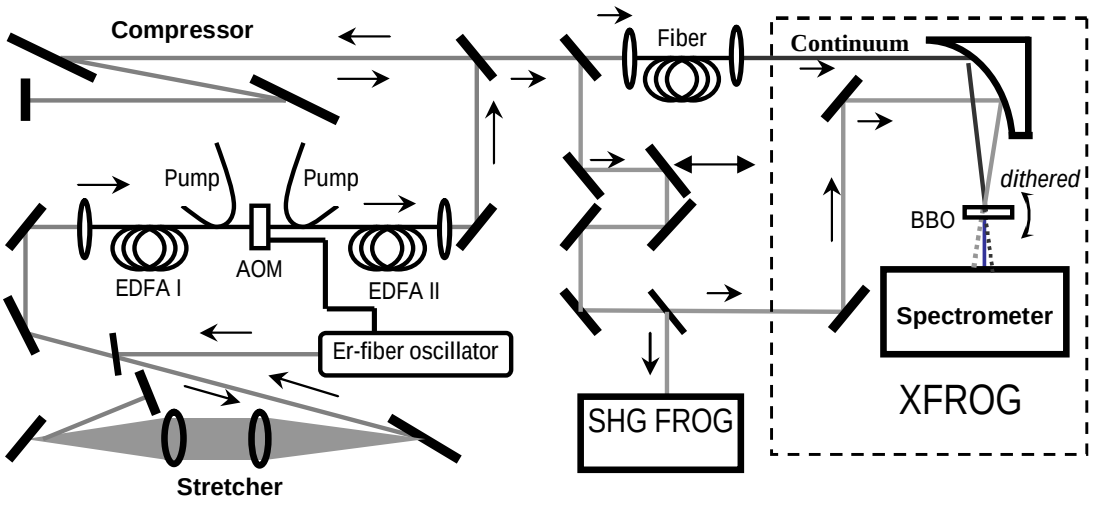

Figure 16: Layout of fiber oscillator/amplifier system for producing IR continuum and XFROG measurement

advantages over the visible continuum: it is easier to collimate and propagate due to lower material dispersion at IR wavelengths, and it should be easier to compress due to the availability of periodically poled lithium niobate (PPLN) [7, 70], which can simultaneously frequency double and compress this light, potentially to a single cycle without the need for pulse compressors that cause spatial distortions in the beam.

Our experimental layout is shown in Figure 16. The fiber oscillator/amplifier system consists of a diode-pumped Er-fiber oscillator operating at ~ 1550 nm, a diffraction-grating stretcher, an Er-fiber chirped-pulse amplifier (CPA) and a diffraction-grating compressor [46]. It can deliver $\sim$ 600-fs optical pulses with energies of hundreds of nJ at a variable repetition rate of 40–500 KHz. The high-energy output pulse is coupled into a 41-cm-long standard silica fiber for broad-spectrum generation. When the coupled energy is about 250 nJ (at a 40 KHz repetition rate), an ultra-broadband continuum is produced as shown in Figure 17 (measured with a spectrum analyzer). The spectral fall-off at 1750 nm is due to the weak response of the detector at and above this wavelength. Additional measurements (not shown) using sum-frequency generation show that the continuum extends to 2400 nm. The narrowband spike at the input-pulse wavelength is due to the amplified spontaneous emission of the fiber amplifier, which has small energy.

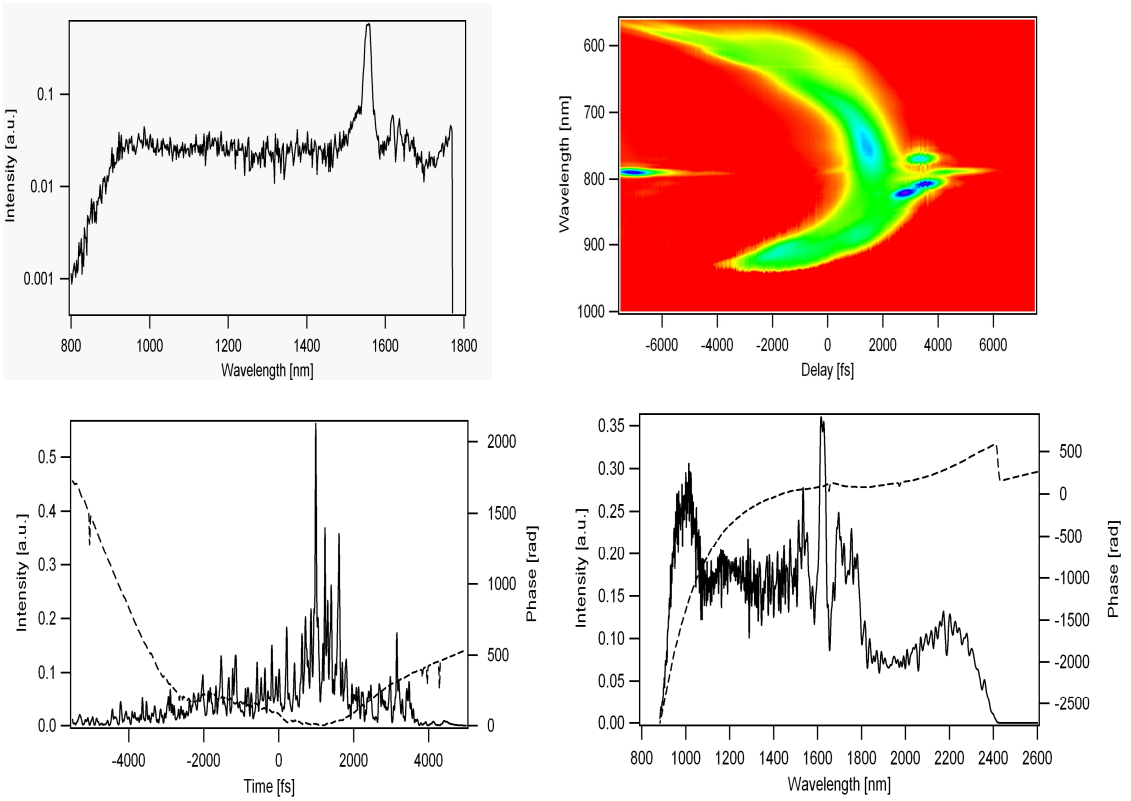

Figure 17: Upper left: The measured continuum spectrum using a spectrum analyzer whose detector response falls off at 1700 nm. Additional measurement using sum-frequency generation shows the continuum extends 2.4 μm. The narrowband spike at the input-pulse wavelength is due to the ASE of the fiber amplifier. Upper right: Measured XFROG trace of the IR continuum. Lower left: Retrieved intensity and phase (dashed line) vs. time. Lower right: Retrieved intensity and phase (dashed line) vs. wavelength for the ultra-broadband continuum. The retrieved continuum ranges from 880 to 2400 nm.

FROG is a very reliable technique for measuring the time-dependent intensity and phase of ultrashort laser pulses [115]. Baltuska et al. have measured 4.5 fs pulses with spectra from 600 to 1000 nm using SHG-FROG with a 10-μm-thick second-harmonic-generation (SHG) crystal [8]. But no known SHG medium achieves the huge bandwidth required to measure this continuum, even in the IR. Fortunately, we recently showed that dithering the crystal angle during FROG measurement significantly increases the phase-matching bandwidth [98], and that a cross-correlation FROG technique based on sum-frequency generation allows the complete measurement of an ultra-broad continuum [128] produced in a microstructure fiber [102].

We have combined the dithered-crystal technique with the XFROG technique to measure our IR continuum phase. XFROG involves gating the unknown pulse (here the continuum) with a shorter, known reference pulse. For the reference pulse in these XFROG measurements, we use a small fraction of the output pulse energy from the fiber oscillator/amplifier. This pulse was easily characterized using SHG FROG (see Figure 16). The IR continuum and the reference pulse were then focused into an angle-dithered 1-mm-thick BBO crystal to generate sum-frequency. The delay of the reference pulse was controlled by a stepper-motor. We have found that a 1-mm-thick BBO dithered by about 10 degrees is able to phase match the whole range of our IR continuum. The measured XFROG trace is shown in Figure 17. This trace shows that the continuum exhibits very strong cubic spectral phase (quadratic chirp), which is probably due to residual linear group delay dispersion (GDD) around 1300–1500 nm in the fiber. The retrieved intensity and phase vs. time and wavelength are also shown in Figure 17. While this pulse is extremely complex, all that is important for the purpose of compression is the spectral phase, which is well behaved. And this measured spectral phase provides useful information for PPNL crystal design, and a shorter optical pulse is expected by PPNL compression in the near future.

In summary, we have demonstrated an 880-2400 nm continuum generation by coupling a 600-fs, 250-nJ optical pulse, centered at 1550 nm, into a 41-cm-long silica fiber. The continuum phase has been measured by using the angle-dithered FROG (XFROG) technique.

CHAPTER 7

SPATIAL CHIRP IN ULTRAFAST LASER BEAMS

7.1 Introduction

Spatial chirp, a phenomenon that different frequency components in a broad-bandwidth beam separate in space, is a very common and often undesirable spatio-temporal distortion in ultrafast optics. It can be introduced by many routine operations in laser labs. For example, a beam going through a dispersive element such as a prism or a grating experiences angular dispersion. After some propagation, angular dispersion naturally results in spatial chirp. Ultrafast laser scientists often use identical anti-parallel prism/grating pairs to generate negative group-delay dispersion [90]. The output beam coming out of the prism/grating pair contains significant spatial chirp. Although using the prism/grating pair in a double-pass setup can eliminate spatial chirp in the output beam, small misalignment often leaves some amount of residual spatial chirp in the beam [Figure 18(a)]. Other common practices in a lab, such as propagating beam through a tilted substrate [Figure 18(b)], also introduces spatial chirp.

In some other situations, we need to deliberately separate different frequency components spatially, so that we can discriminatively operate on these frequency components. A common example is the Fourier-synthesis pulse shaping [64, 124]. In this technique, a lens (or curved mirror) is placed one focal length away from a grating (or prism) in a telecentric configuration, mapping frequencies to positions, i.e., creating spatial chirp, on its focal plane [Figure 18(c)]. Therefore, transmission of the beam through an amplitude/phase modulator on the focal plane permits imposition of spatial modulation, which, because of spatial chirp, is also spectral modulation on the pulse. This allows one to generate a pulse with arbitrary spectral intensity or phase. The accuracy of the pulse shaping obviously depends on the degree of spatial chirp on the focal plane, on which extensive studies have been carried out in the past [64, 122, 123]. Other applications of spatial chirp include using it to suppress

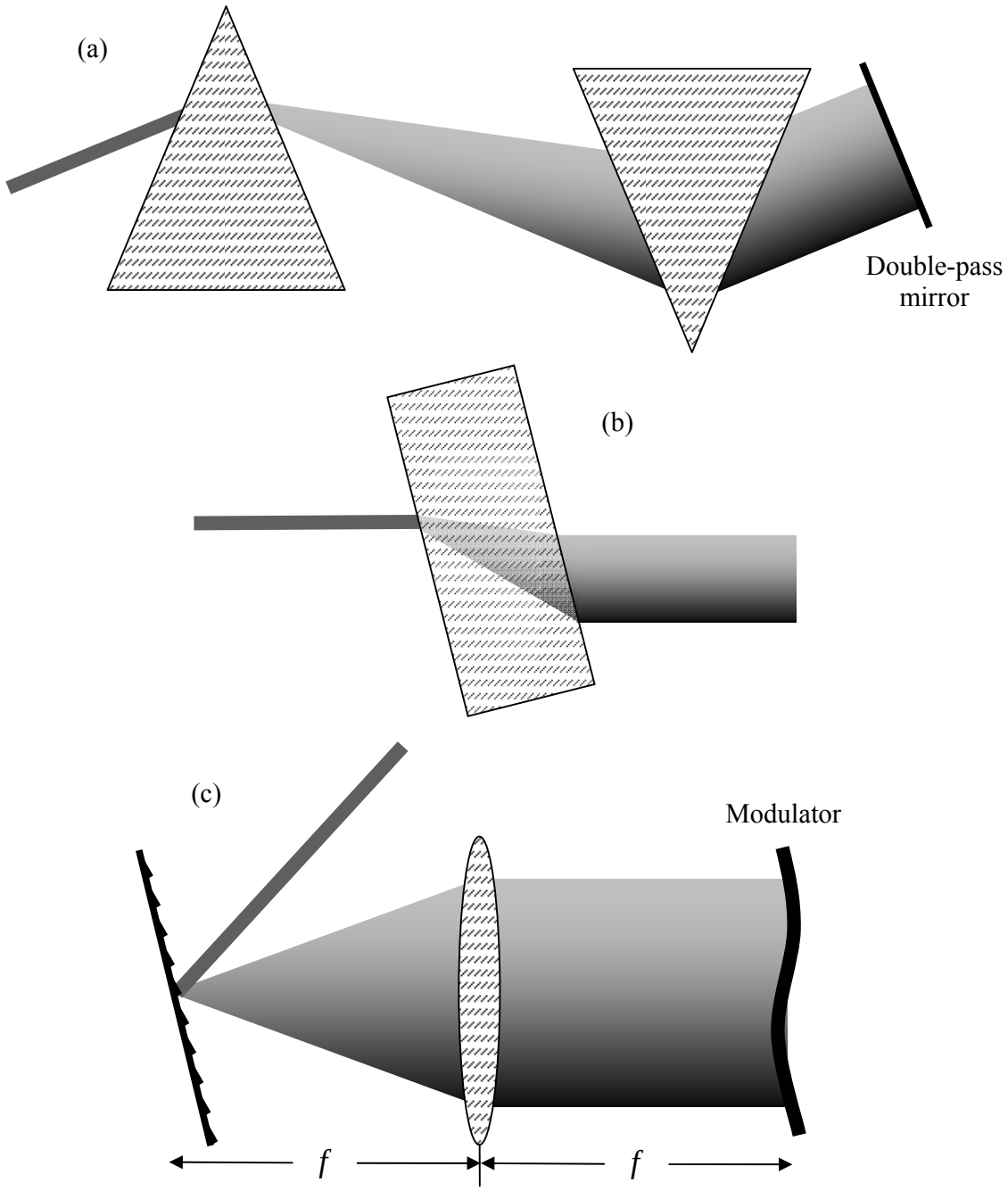

Figure 18: Generation of spatial chirp in a (a) prism pair, (b) tilted substrate, (c) f-f Fourier-synthesis pulse shaper.

longitudinal mode competition [19, 91], etc.

The twenty-first century has seen intensified interest in the spatio-temporal analysis of ultrafast-pulse beams. Numerous methods have been proposed to measure beams' spatio-temporal characteristics [105, 35, 36, 55, 113, 5, 6, 101], which has recently evolved into a new front of ultrafast optics. To study these spatio-temporal effects, clear and unambiguous definitions of the various coupling parameters are undoubtedly needed. Particularly, discussions on spatial chirp, one of the most common spatio-temporal coupling effects, have in the past been mostly confined to specific devices [123, 122, 91, 86, 87, 114, 42, 95], and its definition has been somewhat arbitrary and vague in literature and has not been sufficiently clarified. It is in this context that a proper universal device-independent definition of spatial chirp needs to be established. In this chapter, we establish two definitions of spatial chirp, and explore their relationship. The relationship between the two spatial-chirp parameters is found to be analogous to that between the parameters describing temporal chirp in time and frequency domains.

7.2 Definitions of Spatial Chirp

We start with the case where no spatial chirp is present. In this case, the amplitude of the electric field at position x and frequency ω (defined as frequency offset from the center frequency of the beam) can be written in the form:

$$E(x,\omega) = E_x(x)\, E_\omega(\omega) \tag{8}$$

where the spatial amplitude $E_x(x)$ and the spectral amplitude $E_\omega(\omega)$ are completely separate functions.

In the presence of spatial chirp (here we would assume it exists in one transverse spatial dimension x only), $E(x,\omega)$ becomes an inseparable two-variable function, whose spatial and spectral dependences are coupled. We can easily measure the spatio-spectral intensity profile of the spatially chirped beam by sending the beam into an imaging spectrometer with a two-dimensional camera on its output image plane, as depicted in Figure 19. Fields sampled at different points along the entrance slit of the spectrometer are spectrally resolved onto different rows of the camera image, resulting in a x-ω trace of the field intensity. With

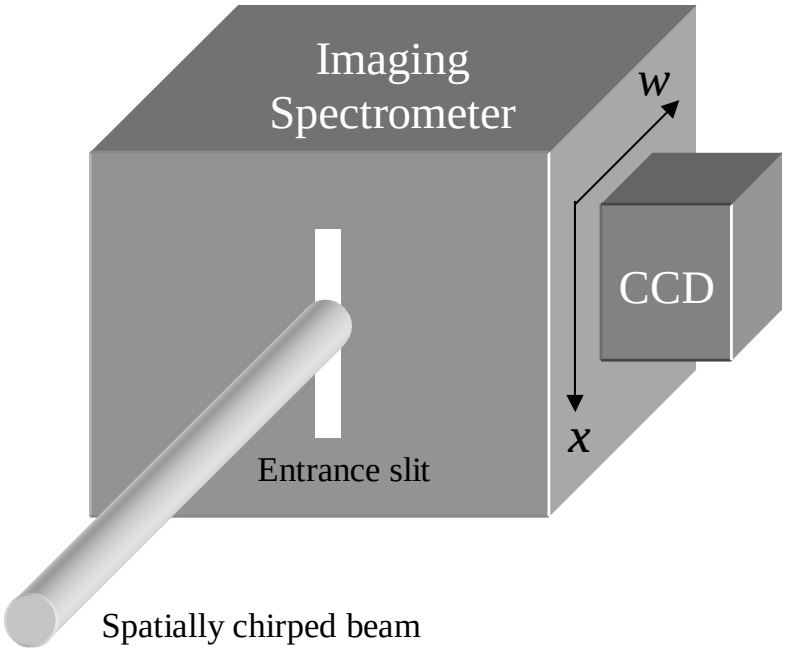

Figure 19: Measuring spatial chirp using an imaging spectrometer.

linear spatial chirp, the spatio-spectral intensity profile will appear tilted. Figure 20(a) shows a typical x-ω intensity plot of an experimental beam.

Obviously, the degree of spatial chirp can be characterized by measuring the slope of the x-ω trace. However, there is one subtlety in this measurement, namely, there are two intuitive but different ways of measuring the tilt of the x-ω trace. The first involves measuring the center frequencies of all the spatial slices, which yields a $\omega_0(x)$ function. The slope of the $\omega_0(x)$ function, $\upsilon \equiv \mathrm{d}\omega_0/\mathrm{d}x$, might be considered a natural measure of spatial chirp, which we will call *frequency gradient*. An alternative definition would be to measure the beam center positions of all the frequency components, which gives us a $x_0(\omega)$ function. Its slope $\zeta \equiv \mathrm{d}x_0/\mathrm{d}\omega$ is also a good measure of spatial chirp, which we will call *spatial dispersion*. Both parameters characterize the spatial chirp, and more importantly, they are not trivial reciprocals of one another. As can be seen in Figure 20(a), the lines of triangles and circles do not overlap. Some researchers have been aware of this subtlety of spatial chirp parameterization. For example, Ohmae et al. have noted the difference between the x-ω_0 and ω-x_0 curves in their analysis of a Martinez-type multipass pulse stretcher, and their particular ray-tracing calculation yields the ω-x_0 result [95]. However, there has

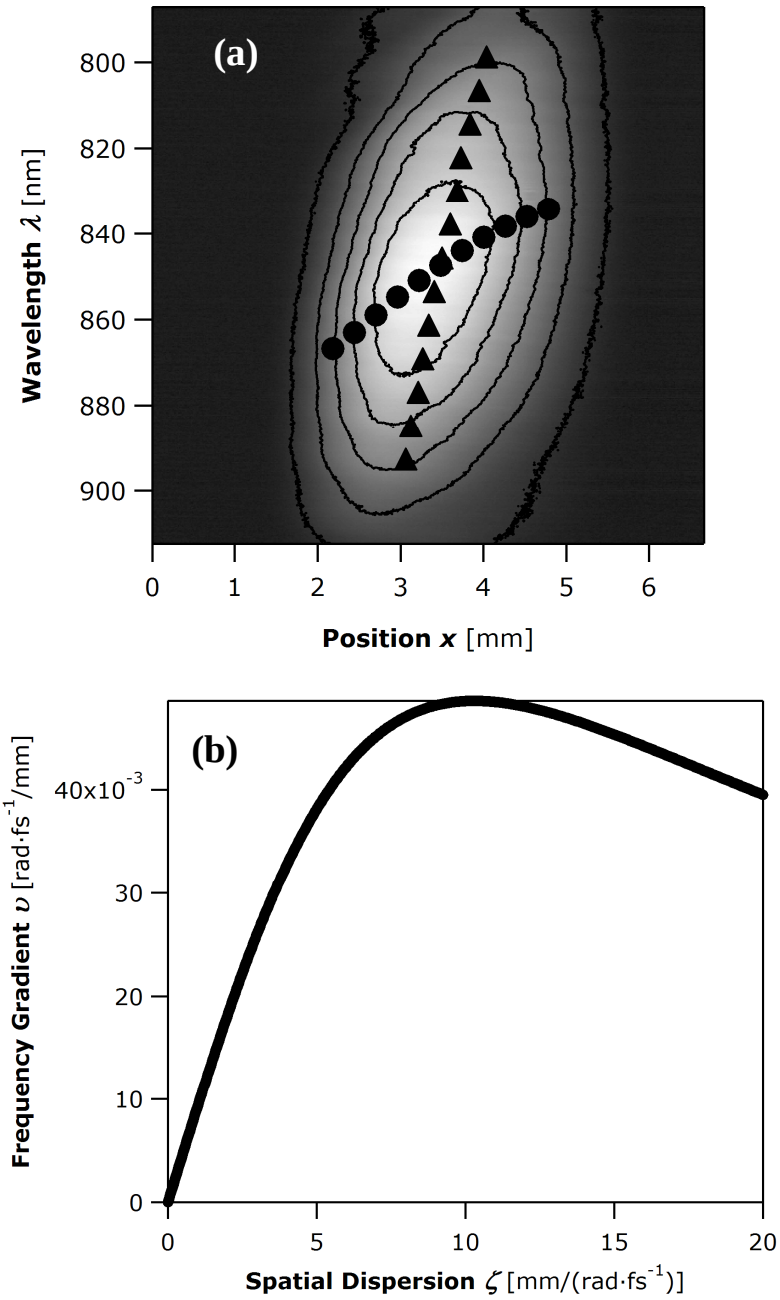

Figure 20: (a) Measured spatio-temporal intensity profile of an experimental spatially chirped beam. The triangles indicate the ω_0-x function, which determines frequency gradient υ , and the circles indicate the x_0-ω function, which determines spatial dispersion ζ. (b) Plot of frequency gradient υ vs. spatial dispersion ζ, with the same experimental conditions for the measurement in plot (a).

been no previous work published on the general relationship between the two spatial-chirp parameters, which is necessary background for the increasingly important research of spatio-temporal distortions. We will devote the rest of the chapter on this issue, and will draw an analogy between spatial chirp and temporal chirp at the end.

Before the discussion, we would like to point out that in most cases spatial chirp is introduced through angular dispersion; therefore, spatial dispersion is often the more fundamental of the two definitions. When a beam with angular dispersion $\beta = \mathrm{d}\theta/\mathrm{d}\omega$ propagates through a distance L, the induced change in spatial dispersion is

$$\Delta\zeta = L\beta \tag{9}$$

which is completely determined by the optical system itself. Frequency gradient, on the other hand, is affected indirectly. As can be seen later, the change of frequency gradient depends not only on the optical system, but on the parameters of the input beam and pulse as well. It is in this sense that spatial dispersion is a more fundamental parameter of spatial chirp in its generation, manipulation and removal than frequency gradient. Frequency gradient, on the other hand, is often more useful in the intended application of spatial chirp.

The relationship between frequency gradient and spatial dispersion is in general complicated, in that it depends on the spatial mode profiles of all the constituent frequency components, and the shape of spectrum. A common assumption is to assign all the frequency components the same spatial mode profile, which we will write as $E_x(x)$. We will also write the complex spectral amplitude of the beam as $E_\omega(\omega)$. Then the field expression at position x and frequency ω in the beam can be written in terms of spatial dispersion ζ as:

$$E(x,\omega) = E_\omega(\omega)\, E_x(x - \zeta\omega) \tag{10}$$

We will focus on the simplest possible case, which is a Gaussian spectrum and a Gaussian spatial profile for all the frequency components. Namely,

$$E_\omega(\omega) = \exp\left[-\left(\frac{\omega}{\Delta\omega}\right)^2\right], \quad E_x(x) = \exp\left[-\left(\frac{x}{\Delta x}\right)^2\right] \tag{11}$$

where $\Delta\omega$ is the frequency bandwidth of the beam ($1/e$ amplitude half width, as are for all widths defined so forth); Δx is the beam width of a particular frequency component.

The spatio-spectral field amplitude is then

$$E(x,\omega) = E_0 \exp\left[-\left(\frac{\omega}{\Delta\omega}\right)^2\right] \exp\left[-\left(\frac{x-\zeta\omega}{\Delta x}\right)^2\right] \tag{12}$$

We may reorganize the two exponential functions, and write the field in terms of frequency gradient υ. The expression becomes

$$E(x,\omega) = E_0 \exp\left[-\left(\frac{x}{\Delta x'}\right)^2\right] \exp\left[-\left(\frac{\omega-\upsilon x}{\Delta\omega'}\right)^2\right] \tag{13}$$

where

$$\upsilon = \frac{\zeta}{\zeta^2 + \left(\frac{\Delta x}{\Delta\omega}\right)^2} \text{ is the frequency gradient;} \tag{14a}$$

$$\Delta\omega' = \left[\frac{1}{(\Delta\omega)^2} + \frac{\zeta^2}{(\Delta x)^2}\right]^{-1/2} \text{ is the locally reduced frequency bandwidth due to} \tag{14b}$$

spatial chirp, available at any particular locations in the beam;

$$\Delta x' = \left[\frac{1}{(\Delta x)^2} - \left(\frac{\upsilon}{\Delta\omega}\right)^2\right]^{-1/2} \text{ is the increased overall beam width due to spatial} \tag{14c}$$

chirp.

Eq. (14a) describes the relationship between the frequency gradient υ and the spatial dispersion ζ . Note that they are not reciprocals of one another. In fact, they are asymptotically reciprocals only when spatial dispersion $\zeta \equiv \mathrm{d}x_0/\mathrm{d}\omega$ is much larger than $\Delta x/\Delta\omega$. If spatial dispersion ζ is very small, on the other extreme, the two parameters are proportional. For a given beam width Δx and frequency bandwidth $\Delta\omega$, frequency gradient υ reaches its maximum achievable value $\Delta\omega/2\Delta x$ when $\zeta \equiv \mathrm{d}x_0/\mathrm{d}\omega = \Delta x/\Delta\omega$. Figure 20(b) shows the relationship of frequency gradient and spatial chirp with $\Delta x = 1.0$ mm and $\Delta\omega = 0.094$ rad/fs, the conditions for the experimental trace in Figure 20(a), with stated Gaussian approximations.

7.3 Analogy to Temporal Chirp

The distinction between the two definitions of spatial chirp is quite analogous to that between the definitions of temporal chirp in time and frequency domains. For a linearly

chirped Gaussian pulse, we can write it either in the time domain,

$$E(t) = |E(t)| \exp[-i\phi(t)] = E_0 \exp\left[-\left(\frac{t}{\Delta t}\right)^2\right] \exp\left(-\frac{i}{2}\phi_2 t^2\right) \tag{15}$$

or equivalently in the frequency domain,

$$\tilde{E}(\omega) = \left|\tilde{E}(\omega)\right| \exp[-i\varphi(\omega)] = \tilde{E}_0 \exp\left[-\left(\frac{\omega}{\Delta\omega}\right)^2\right] \exp\left(-\frac{i}{2}\varphi_2 \omega^2\right) \tag{16}$$

The two expressions are a Fourier transform pair.

The physical significance of chirp parameters ϕ_2 and φ_2 can be viewed as such: In the time domain, $-\phi_2$ is the derivative of instantaneous (angular) frequency $\omega_0 \equiv -\mathrm{d}\phi(t)/\mathrm{d}t = -\phi_2 t$ with respect to t. On the other hand, in the frequency domain, φ_2 (often called group-delay dispersion) is the derivative of group delay $t_0 \equiv \mathrm{d}\varphi(\omega)/\mathrm{d}\omega = \varphi_2\omega$ with respect to ω. Parameters $\phi_2 = -\mathrm{d}\omega_0/\mathrm{d}t$ and $\varphi_2 = \mathrm{d}t_0/\mathrm{d}\omega$ are two different but equivalent parameters describing temporal (spectral) chirp in the time/frequency domains, just as parameters $\zeta = \mathrm{d}x_0/\mathrm{d}\omega$ and $\upsilon = \mathrm{d}\omega_0/\mathrm{d}x$ are the parameters describing spatio-temporal chirp in the frequency/space domains. Indeed, on a closer look, the relationship between ϕ_2 and φ_2,

$$\varphi_2 = \frac{-\phi_2}{\frac{1}{4}\phi_2^2 + \frac{1}{(\Delta t)^2}} \tag{17}$$

which follows from the Fourier transform, is remarkably similar to the relationship between ζ and υ [Eq. (14a)] for the case of spatial chirp.

7.4 Conclusion

To understand the difference and relationship of spatial dispersion and frequency gradient, the two definitions of spatial chirp, is important. Many uses of spatial chirp require a careful control of one parameter or the other. For example, in pulse shaping, frequency gradient determines the mapping of spatial modulation to spectral modulation. From our definition, we can see that the two parameters are related in a complicated way, involving both the beam width and the frequency bandwidth. Indeed, there is a maximum frequency gradient value one can achieve with given pulse and beam parameters. Knowing their relationship can help researchers achieve better control of their experiment conditions involving spatial chirp.

To conclude, we have proposed and compared two definitions of spatial chirp, namely, spatial dispersion and frequency gradient. The relationship between the two parameters has been derived, and we find it analogous to that between the two quadratic-phase parameters (ϕ_2 and φ_2) characterizing temporal chirp in the time/frequency domains.

CHAPTER 8

ZEEK'S PARADOX: PULSE-FRONT TILT WITHOUT ANGULAR DISPERSION

8.1 Introduction

The space and time dependencies of an ultrashort pulse's electric field are often assumed to be separable into independent functions. This assumption fails when coupling occurs between the pulse electric field's space and time dependencies, which is referred to as a spatio-temporal distortion. Spatio-temporal distortions are common in ultrafast optics because the generation, amplification, and manipulation of ultrashort pulses all involve the deliberate introduction and removal of massive spatio-temporal distortions. While it is generally desired that the resulting pulse be free of such distortions, improper alignment is common, and as a result, ultrashort pulses utilized in applications are often contaminated with spatio-temporal distortions. Indeed, the broadband nature of ultrashort pulses makes them particularly vulnerable to these distortions.

The most common such distortion is angular dispersion (AD), which is caused by the use of a dispersive element such as a prism or grating. Once it was realized that angular dispersion yields negative group-velocity dispersion in the mid 1980's [50, 56, 90], researchers have widely adopted prism/grating pairs as pulse compressors/stretchers. Pulse compressors/stretchers are designed so that, at the output, there is no angular dispersion. Unfortunately, these devices have strict alignment requirements, and, as a result, some residual angular dispersion often remains in the output pulse. Although the effect of angular dispersion may be initially very small, the pulse's constituent frequency components become increasingly separated as the pulse propagates, resulting in another spatio-temporal distortion called spatial chirp (SC), in which the frequency changes transversely across the beam.

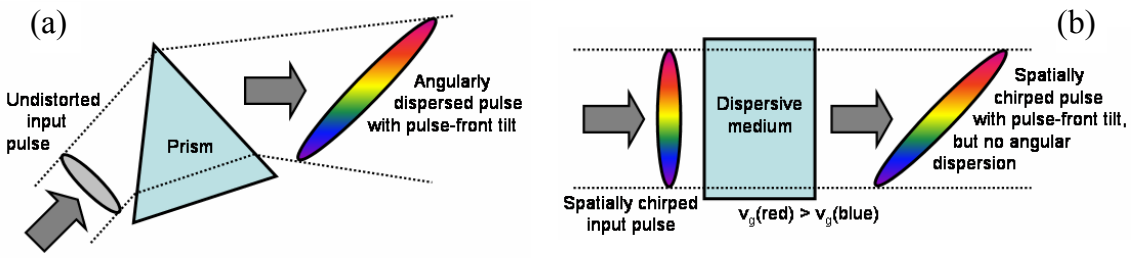

Figure 21: Two sources of pulse-front tilt: (a) Angular dispersion; (b) combination of spatial and temporal chirp.

Angular dispersion also yields another spatio-temporal distortion—pulse-front tilt (PFT) [see Figure 21(a)]. In fact, it is generally thought that angular dispersion and pulse-front tilt are equivalent phenomena. This is due to a well-known simple Fourier transform result given by Bor et al. [14] and Hebling [62]. Specifically, a beam with pulse-front tilt is given by:

$$E(x, z, t) = E_0(x, z, t - \gamma x) \tag{18}$$

where we have suppressed the y-dependence. Simply Fourier-transforming from the x-t domain to the k-ω domain, and using two applications of the shift theorem, we have:

$$\hat{\tilde{E}}\left(k_x, k_z, \omega\right) = \hat{\tilde{E}}_0\left(k_x - \gamma\omega, k_z, \omega\right) \tag{19}$$

which is a beam with angular dispersion.

While the above proof seems quite fundamental, we show in this work that angular dispersion and pulse-front tilt are *not* equivalent, and provide an additional (and rather common!) source of pulse-front tilt, in which no angular dispersion occurs. We point out that the above derivation of the AD/PFT equivalence only holds for plane waves, and our counter-example incorporates a finite-size beam. In fact, due to their infinite size, plane waves also cannot be used to describe spatial chirp, which is the key to this effect.

Specifically, to see how pulse-front tilt can easily occur in the absence of angular dispersion, consider an initially transform-limited, but spatially chirped, finite-size beam—with no angular dispersion—passing through a dispersive medium [see Figure 21(b)]. Due to the group-velocity dispersion in the medium, the redder side of the beam emerges from the medium earlier than the bluer side, resulting in pulse-front tilt in the output beam. Because

no angular dispersion exists, this obviously violates the well-known AD/PFT equivalence. This paradoxical case concerning the AD/PFT equivalence was first put forward by a former postdoc in our group Erik Zeek. In the rest of this chapter, we will establish a generalized ultrashort-pulse beam theory to resolve this paradox.

Some other previous work has considered pulse-front tilt. Geometrical optical modeling of angular dispersion in ultrashort pulses was performed using plane waves [81]. Bor and Racz [13] showed that position-dependent delays of the pulse front occur at the output of a two-prism pulse compressor, but they did not note the violation of the AD/PFT equivalence. The most comprehensive work on spatio-temporal distortions with dispersive elements is that of Martinez [87], who considered pulse-front tilt in an angularly dispersed beam with finite beam size. Martinez derived the modified expression of pulse-front tilt in this case, but did not realize that his finite-beam correction is indeed due to the combined effect of the temporal chirp and spatial chirp, both results of beam propagation with angular dispersion.

8.2 Spatio-Temporal Distortions in the Case of Finite Beam Size

We begin with an expression for the electric field of a pulse with linear spatial chirp and angular dispersion.

$$E(x,\omega) = E(\omega)\exp\left[-i\frac{k(x-\zeta\omega)^2}{2q}\right]\exp(-ik\beta\omega x) \tag{20}$$

where ω is the offset from the center angular frequency, and q is the complex q parameter of a Gaussian beam:

$$q(z) = (z+d) + i\frac{\pi w^2}{\lambda} = (z+d) + i\frac{kw^2}{2} \tag{21}$$

where d is the position of the beam waist and w is the spot size. The spatial chirp and angular dispersion are parameterized by $\zeta \equiv \mathrm{d}x_0/\mathrm{d}\omega$ and $\beta \equiv \mathrm{d}\theta_0/\mathrm{d}\omega$, where x_0 is the beam center position of the ω-component of the beam and θ_0 is the propagation angle of this component.

Throughout this work, we concentrate on spatio-temporal distortions in x-direction only and therefore neglect the beam's y-dependence. Generalization to both x and y dependences is straightforward.

We assume a Gaussian pulse with linear chirp:

$$E(\omega) = E_0 \exp\left(-\frac{\omega^2\tau_0^2}{4}\right)\exp\left(-i\frac{\varphi^{(2)}}{2}\omega^2\right) \tag{22}$$

For a well collimated beam, we can write:

$$q(z) \approx q_0(d) = i\frac{kw^2}{2} \tag{23}$$

Using these, Eq. (20) becomes

$$E(x,\omega) = E_0 \exp\left(-\frac{\omega^2\tau_0^2}{4}\right)\exp\left[-\frac{(x-\zeta\omega)^2}{w^2}\right]\exp\left(-i\frac{\varphi^{(2)}}{2}\omega^2\right)\exp(-ik\beta\omega x) \tag{24}$$

Here, we would like to point out, as shown in Chapter 7, there are two different but related definitions of spatial chirp. We can either define spatial chirp as spatial dispersion $\zeta \equiv \mathrm{d}x_0/\mathrm{d}\omega$, where x_0 is the beam center position of the ω-component, or equivalently define it as frequency gradient $\upsilon \equiv \mathrm{d}\omega_0/\mathrm{d}x$, where ω_0 is the mean frequency at position x. The relationship between ζ and υ is

$$\upsilon = \frac{\zeta}{\zeta^2 + \dfrac{w^2\tau_0^2}{4}} \tag{25}$$

Using frequency gradient υ, Eq. (24) may be rewritten as

$$E(x,\omega) = E_0 \exp\left[-\left(\frac{x}{w'}\right)^2\right]\exp\left[-\frac{(\tau')^2}{4}(\omega-\upsilon x)^2\right]\exp\left(-i\frac{\varphi^{(2)}}{2}\omega^2\right)\exp(-ik\beta\omega x) \tag{26}$$

where $w' = \left(\dfrac{1}{w^2} - \dfrac{\upsilon^2\tau_0^2}{4}\right)^{-1/2}$ is the overall beam width, increased from w due to spatial chirp, $\tau' = \left(\tau_0^2 + \dfrac{4\zeta^2}{w^2}\right)^{1/2}$ is the local transform-limited pulse width, increased from τ_0 due to the reduced locally available bandwidth.

After some reorganizing,

$$\begin{aligned} E(x,\omega) = E_0 &\exp\left[-\left(\frac{x}{w'}\right)^2\right]\exp\left[-i\left(k\beta + \frac{\varphi^{(2)}}{2}\upsilon\right)\upsilon x^2\right] \\ &\times \exp\left[-\frac{(\tau')^2}{4}(\omega-\upsilon x)^2\right]\exp\left[-i\frac{\varphi^{(2)}}{2}(\omega-\upsilon x)^2\right] \\ &\times \exp\left[-i\left(k\beta + \varphi^{(2)}\upsilon\right)x(\omega-\upsilon x)\right] \end{aligned} \tag{27}$$

The frequency dependence in Eq. (27) is familiar, namely a linearly chirped pulse, and can be easily inversely Fourier-transformed into the time domain:

$$E(x,t) = f(x) \exp\left[-\frac{(t-t_0)^2}{\tau^2}\right] \exp\left\{i\left[\phi^{(1)}(t-t_0) + \frac{\phi^{(2)}}{2}(t-t_0)^2\right]\right\} \tag{28}$$

where:

$$f(x) = \frac{1}{\pi}\left[(\tau')^2 + i2\varphi_2\right]^{-1/2} E_0 \exp\left[-\left(\frac{x}{w'}\right)^2\right] \exp\left(i\frac{\varphi^{(2)}}{2}\upsilon^2 x^2\right) \tag{29a}$$

$$t_0 = \left(k\beta + \varphi^{(2)}\upsilon\right)x \tag{29b}$$

$$\tau = \left[(\tau')^2 + \frac{4\left(\varphi^{(2)}\right)^2}{(\tau')^2}\right]^{1/2} = \left[\tau_0^2 + \frac{4\zeta^2}{w^2} + \frac{4\left(\varphi^{(2)}\right)^2}{\tau_0^2 + \frac{4\zeta^2}{w^2}}\right]^{1/2} \tag{29c}$$

$$\phi^{(1)} = \upsilon x \tag{29d}$$

$$\phi^{(2)} = \frac{\varphi^{(2)}}{\frac{(\tau')^2}{4} + \left(\varphi^{(2)}\right)^2} = \frac{\varphi^{(2)}}{\frac{1}{4}\left(\tau_0^2 + \frac{4\zeta^2}{\sigma^2}\right)^2 + \left(\varphi^{(2)}\right)^2} \tag{29e}$$

We identify t_0 as the pulse-front (maximum intensity contour) arrival time, and the pulse-front tilt may be characterized by the derivative of t_0 with respect to x,

$$p \equiv \frac{\mathrm{d}t_0}{\mathrm{d}x} \tag{30}$$

The pulse-front tilt angle ψ, the angle between the pulse front and the propagation direction z, is then given by

$$\tan\psi = pc \tag{31}$$

From Eq. (29b), it is easy to see that, for an ultrashort-pulse beam with Gaussian spectrum and Gaussian spatial profile, the pulse-front tilt is

$$p = p^{\mathrm{AD}} + p^{\mathrm{SC+TC}} \tag{32}$$

where

$$p^{\mathrm{AD}} = k\beta \tag{33a}$$

$$p^{\mathrm{SC+TC}} = \varphi^{(2)}\upsilon \tag{33b}$$

This is the key result of this paper. Pulse-front tilt, in general, consists of two terms. The first term p^{AD} is the well-known angular-dispersion term, being the same form as derived by Bor et al. [14] and Hebling [62] for plane waves. The second term $p^{\mathrm{SC+TC}}$ is a pulse-front tilt effect caused by the combination of spatial chirp, which is characterized by frequency gradient υ, and temporal chirp, which is characterized by group-delay dispersion $\varphi^{(2)}$. This new pulse-front tilt effect is clearly the cause of the pulse-front tilt in the scenario shown in Figure 21(b), in which no angular dispersion exists.

It is also important to note that these two sources of pulse-front tilt have subtle physical effects on the pulse, beyond simply tilting the pulse front. Angular dispersion causes different frequency components to propagate at different angles, resulting in tilt in both the pulse fronts (contours of equal intensity) and the phase fronts (contours of equal phase). On the other hand, simultaneous spatial and temporal chirp tilts the pulse front, while leaving phase fronts of constituent frequencies untilted. This point is very important in the measurement of the two effects.

8.3 Propagation of Ultrashort-Pulse Beams with First-Order Spatio-Temporal Coupling

Eqs. (27) and (28) give the expressions of the electric field in frequency and time domains at a particular longitudinal position z_0. In this section, we propagate the field to an arbitrary position z, and discuss how the spatial-temporal coupling parameters, including spatial chirp and pulse-front tilt, evolve. To accomplish this, the Fresnel-Kirchoff integral formula [63] is used:

$$E\left(x,\omega,z\right)=\frac{i}{\lambda z}\int_{-\infty}^{\infty}E\left(x',\omega,z=0\right)\exp\left[-\frac{i\pi}{\lambda z}\left(x-x'\right)^{2}\right]\mathrm{d}x' \tag{34}$$

We start from an initial field at $z_0 = 0$,

$$\begin{aligned}E\left(x,\omega,z=0\right)&=E\left(\omega,z=0\right)\exp\left[-i\frac{k\left(x-\zeta_0\omega\right)^{2}}{2q_0}\right]\exp\left(-ik\beta\omega x\right)\\&=E_0\exp\left(-\frac{\omega^2\tau_0^2}{4}\right)\exp\left(-i\frac{\varphi_0^{(2)}}{2}\omega^2\right)\exp\left[-i\frac{k\left(x-\zeta_0\omega\right)^{2}}{2q_0}\right]\exp\left(-ik\beta\omega x\right)\end{aligned} \tag{35}$$

Substituting Eq. (35) in Eq. (34), we obtain:

$$\begin{aligned} E(x,\omega,z) &= \frac{ik}{2\pi z} E_0 \exp\left(-\frac{\omega^2\tau_0^2}{4}\right) \exp\left(-i\frac{\varphi_0^{(2)}}{2}\omega^2\right) \\ &\times \int_{-\infty}^{\infty} \exp\left[-i\frac{k\left(x'\right)^2}{2q\left(0\right)}\right] \exp\left[-ik\beta\omega\left(x'+\zeta_0\omega\right)\right] \exp\left[-\frac{ik}{2z}\left(x'+\zeta_0\omega-x\right)^2\right] \mathrm{d}x' \\ &= \left[\frac{ik}{2\pi z}\frac{q\left(0\right)}{q\left(z\right)}\right]^{1/2} E_0 \exp\left(-\frac{\omega^2\tau_0^2}{4}\right) \exp\left(-i\frac{\varphi_0^{(2)}}{2}\omega^2\right) \\ &\times \exp\left\{i\frac{kz}{2}\frac{q\left(0\right)}{q\left(z\right)}\left(\frac{x-\zeta_0\omega}{z}-\beta\omega\right)^2 - ik\left[\beta\zeta_0\omega^2+\frac{\left(x-\zeta_0\omega\right)^2}{2z}\right]\right\} \end{aligned} \tag{36}$$

For well collimated beams, we can write:

$$\frac{q\left(0\right)}{q\left(z\right)} = \frac{d+i\frac{kw^2}{2}}{z+d+i\frac{kw^2}{2}} \simeq 1+i\frac{2z}{kw^2} \tag{37}$$

Eq. (36) then simplifies to:

$$\begin{aligned} E(x,\omega,z) &= \left(\frac{ik}{2\pi z}\right)^{1/2}\left(1+i\frac{2z}{kw^2}\right)^{1/2} E_0 \exp\left(-\frac{\omega^2\tau_0^2}{4}\right) \exp\left[-\frac{i}{2}\left(\varphi_0^{(2)}-k\beta^2 z\right)\omega^2\right] \\ &\times \exp\left\{-\frac{\left[x-\left(\zeta_0+\beta z\right)\omega\right]^2}{w^2}\right\} \exp\left(-ik\beta\omega x\right) \end{aligned} \tag{38}$$

Note that this is exactly in the form of Eq. (24), with the spatial dispersion and group-delay dispersion parameters substituted by the z-evolved values:

$$\zeta\left(z\right) = \zeta_0 + \beta z \tag{39}$$

$$\varphi^{(2)}\left(z\right) = \varphi_0^{(2)} - k\beta^2 z \tag{40}$$

The physical meanings of these results are obvious. Eq. (39) describes the increase of spatial dispersion with propagation due to angular dispersion. As the pulse propagates, different colors in the pulse become increasingly spatially separated from each other. Eq. (40) describes the introduction of negative group-delay dispersion (GDD) due to angular dispersion, which is the theoretical basis of pulse compressors. Using the evolved values of spatial dispersion and group-delay dispersion, the results in previous section can be applied

to obtain the evolution of other spatial-temporal coupling parameters, including frequency gradient υ and pulse-front tilt p.

The generalized theory of spatio-temporal coupling in ultrafast-pulse beams can also be derived analogously using the matrix formalism introduced by A. G. Kostenbauder [80] (see Appendix B).

8.4 Experiment

In the previous sections, we showed that simultaneous spatial and temporal chirps cause pulse-front tilt, even in the absence of angular dispersion. In this section, we describe our experimental demonstration of these theoretical results. Our experimental setup is shown in Figure 22. We used a prism pair to introduce spatial chirp in the beam. Identical prisms aligned in an anti-parallel Brewster-angle configuration were used to ensure that angular dispersion was eliminated after the second prism. The beam then entered an imaging spectrometer with the direction of the spatial chirp along the entrance slit. A CCD camera on the exit plane of the spectrometer measured the spatio-spectral intensity profile of the beam. From this trace, we can either measure the slope of the beam center position vs. frequency, which yields spatial dispersion ζ, or the slope of the center frequency vs. position, which yields frequency gradient υ. The same beam was also sent to a GRENOUILLE [99, 116], which measured both the GDD and the PFT with high sensitivity [5]. (GRENOUILLE also reveals spatial chirp [6], but a spatially resolved spectrometer measurement has higher sensitivity.) Other sensitive methods of measuring pulse-front tilt have also been demonstrated [119, 120], but they in fact measure angular dispersion. As a result, they could not be used for our purposes. Since the separation between the two prisms was fixed, our setup (see Figure 22) introduced constant spatial chirp with no angular dispersion. Translating one of the prisms in and out of the beam adjusted the temporal chirp in the usual manner.

GRENOUILLE measures the pulse-front tilt as a shift of the center of the trace along the delay axis [5]. Therefore, by translating the prism in and out of the beam (adding and removing material and hence adjusting the temporal chirp of the output pulse), we expect to see a change in the shift of the center of the trace. Figure 23 shows some of

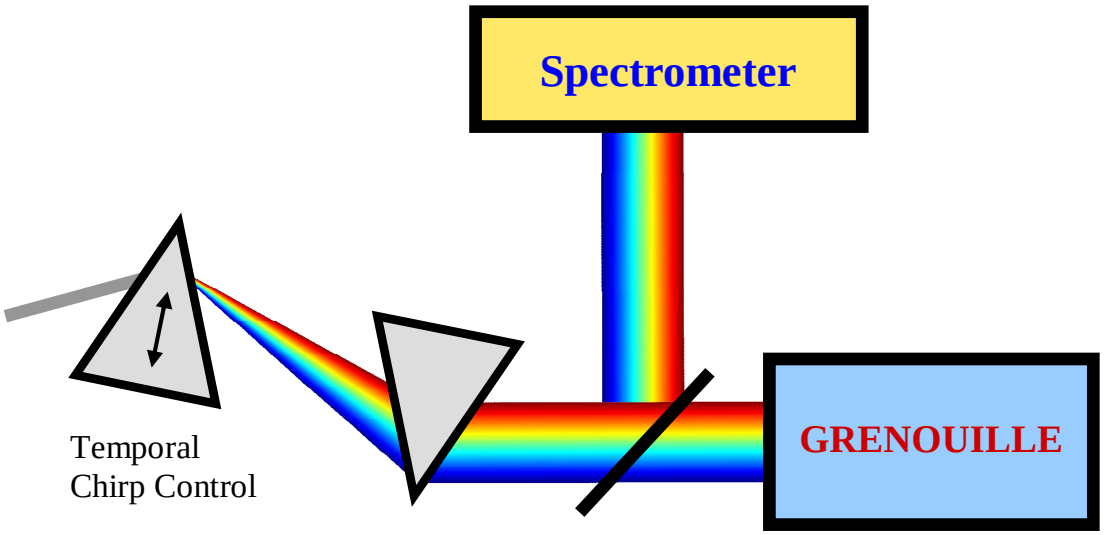

Figure 22: Apparatus to generate constant spatial chirp, variable temporal chirp with no angular dispersion

the experimental GRENOUILLE traces for different values of temporal chirp. These traces clearly show that, although no angular dispersion is present, the beam possesses a significant amount of pulse-front tilt that results from spatial and temporal chirp. This qualitatively demonstrates our theory.

More quantitatively, Eq. (33b) shows that the slope of pulse-front tilt $\varphi^{(2)}$ vs. group-delay dispersion $\varphi^{(2)}$ should yield frequency gradient v. Figure 24 shows such a plot. We measured the slope of this plot to be 8.78×10^{-3} (rad-fs^{-1})/mm (dλ_0/dx = 2.98 nm/mm). The value of frequency gradient measured by the imaging spectrometer is 8.87×10^{-3} (rad-fs^{-1})/mm (dλ_0/dx = 3.01 nm/mm), in excellent agreement with the other measurement.

8.5 Conclusion

In conclusion, we have shown that, the equivalence of pulse-front tilt and angular dispersion is valid only for plane waves, whereas, for finite-size Gaussian beams, simultaneous spatial and temporal chirp also causes pulse-front tilt. We have derived analytical expressions for ultrashort-pulse beams that possess angular dispersion, spatial chirp and temporal chirp. We verified our theoretical results experimentally using GRENOUILLE.

This material is based upon work supported by the National Science Foundation under

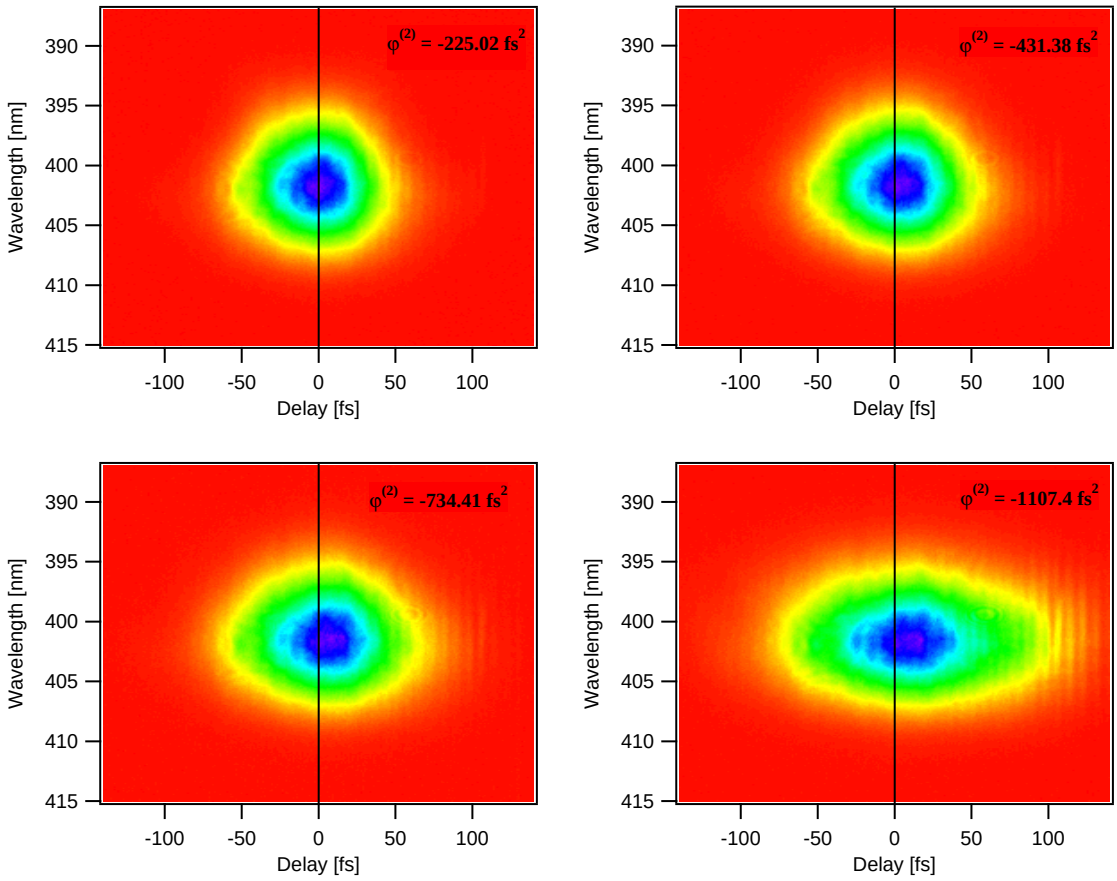

Figure 23: GRENOUILLE traces of a beam that has constant spatial chirp and variable temporal chirp. Note that the amount of shift of the center (a measure of pulse-front tilt) increases with increasing temporal chirp.

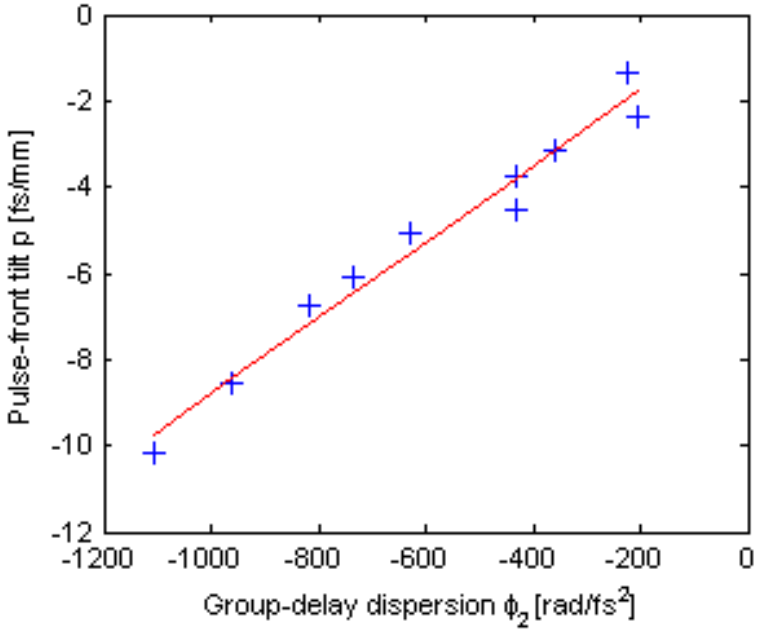

Figure 24: Experimental measurements (plus sign symbols) of pulse-front tilt for different amounts of GDD. The red line shows the linear fit.

Grant No. ECS-9988706. We are grateful for helpful discussions with A. G. Kostenbauder.

CHAPTER 9

GRENOUILLE UNDER SPATIO-TEMPORAL DISTORTIONS

9.1 Introduction

Most pulse characterization techniques work on the assumption that the input ultrafast laser beam is free of spatio-temporal distortions. If that is the case, the measurement results depend only on the temporal dependence of the pulse, while the spatial dependence plays no role, and therefore can be ignored.

When spatio-temporal distortions do exist, such distortions in the input beam would usually cause the measurement results to be distorted. If the distortion is not accounted for in data processing, errors could propagate into the end result.

Spatio-temporal distortions are fairly common in ultrafast laser beams. As is shown in Chapters 7 and 8, many common setups in ultrafast experiments cause spatio-temporal distortions, whose complete removal depends on careful and sensitive alignment subsequently. Not only are spatio-temporal distortions difficult to eliminate, information about their presence and values is also vitally important for the design and adjustment of optical systems. In some cases, spatio-temporal couplings are even intentionally introduced and used to achieve certain goals, such as in the case of noncollinear OPA phase-matching [111], and pulse shaping [64, 122, 123]. Careful manipulation of spatio-temporal couplings in ultrafast laser beams requires good measurement techniques.

Many ultrafast pulse characterization techniques can be extended to measure additional information of spatio-temporal couplings. For example, SPIDER is a pulse characterization technique, whose raw outputs (spectrum and interferogram) are all one-dimensional vectors. It is conceivable to use the second dimension of an imaging spectrometer, and measure spatio-temporal distortions with it. This idea was demonstrated by Dorrer et al.

[35], when they extended the shearing interferometry that SPIDER uses for retrieving the pulse's spectral phase to the spatial dimension, by performing a separate spatial shearing interferometry measurement. Using the two resulting two-dimensional interferograms, they were able to reconstruct the spatio-spectral phase $\varphi(x, \omega)$.

A FROG trace, on the the hand, is a two-dimensional matrix. Adding an extra spatial dimension to it is not as straightforward. However, having two dimensions in a FROG trace is in fact a special forte of the technique, for the two-dimensional trace contains a lot of redundant information about the pulse, which in practice works as a safeguard feature against noise and systematic errors. Discussions on this issue have been given in Chapter 2. Due to the far greater complexity in a two-dimensional trace than a one-dimensional complex-valued pulse, the changes in a FROG trace induced by spatio-temporal distortions are usually distinguishable from the changes induced by temporal variations. This allows the possibility of using the FROG trace to measure extra information on spatio-temporal distortions. The advantage in using a FROG technique is clear: the extra spatio-temporal information comes for free. The measurement apparatus is exactly the same, requiring no modifications to the already very simple device. Meanwhile, all the great features of FROG are preserved, such as informative feedback.

Analysis of the effects of spatio-temporal distortions to a FROG trace of course depends on the specific apparatus geometry. In this chapter, we will focus on a very compact and simple single-shot SHG-FROG device—GRENOUILLE. GRENOUILLE has been shown to be able to measure two of the most common spatio-temporal distortions: spatial chirp and pulse-front tilt. In particular, spatial chirp causes a shear in the GRENOUILLE trace, and pulse-front tilt causes the GRENOUILLE trace to shift in the delay axis—both distinctly not producible in a standard SHG-FROG trace due to delay symmetry. Intuitive explanations can be found in Refs [6] and [5] (Figure 26), where we show the physical origins of the effects. However, the mathematical results drawn from these theories rely on certain simple and naïve assumptions that are in reality questionable with a complicated temporal pulse form and/or spatial profile. In this chapter, we will derive a rigorous theory of GRENOUILLE applicable to an arbitrary input of one-dimensional spatio-temporal field, discuss the effects

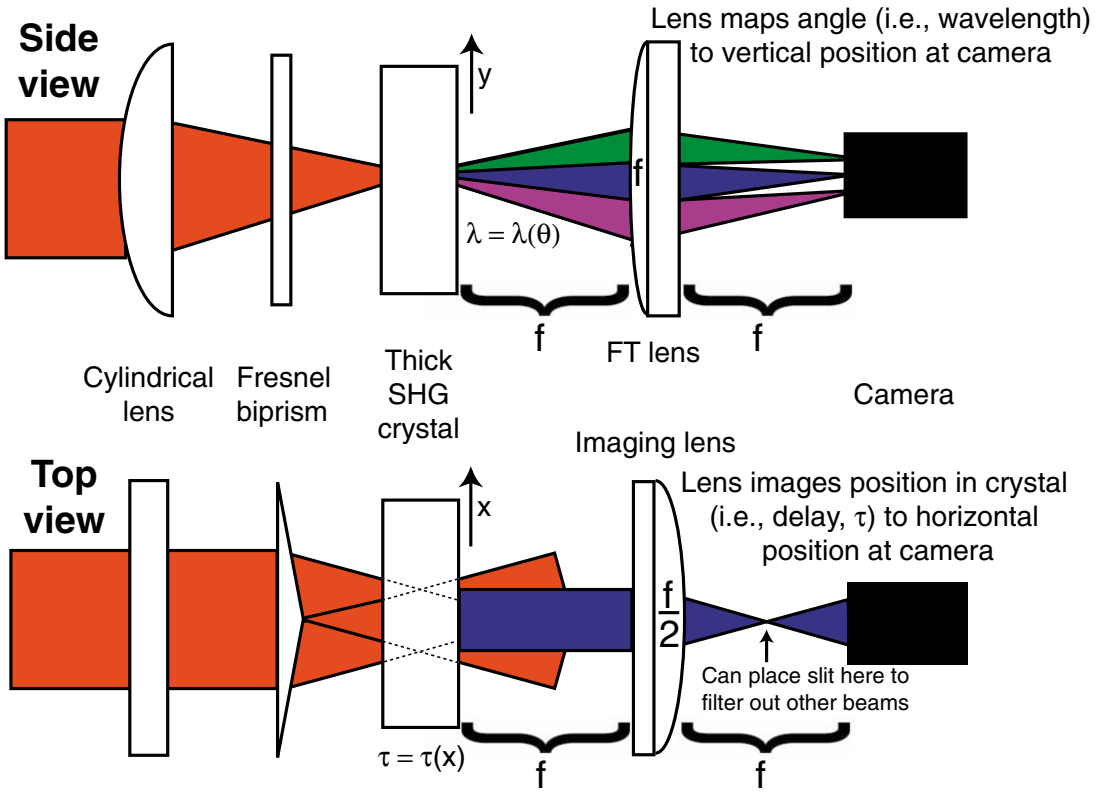

Figure 25: Side and top views of the GRENOUILLE beam geometry

of first-order spatio-temporal distortions to a GRENOUILLE trace, and demonstrate a simple algorithm to retrieve spatio-temporal distortions from a GRENOUILLE trace.

9.2 Rigorous GRENOUILLE Theory with Spatio-Temporal Distortions

The key innovations in GRENOUILLE are the use of two unconventional elements: a Fresnel biprism and a thick SHG crystal (Figure 25).

The Fresnel biprism divides the input beam spatially into two half beamlets, and crosses them in the SHG crystal at a half crossing angle $\theta = \sin^{-1}(n \sin \alpha) - \alpha$, where n is the index of refraction of glass, and $\pi - 2\alpha$ is the apex angle of the Fresnel biprism. This one single element replaces the entire delay generation line in a FROG device, making the device much simpler.

The other innovation is the use of a thick SHG crystal instead of a thin one. Normally, to correctly measure an ultrashort pulse, one needs a nonlinear optical crystal thin

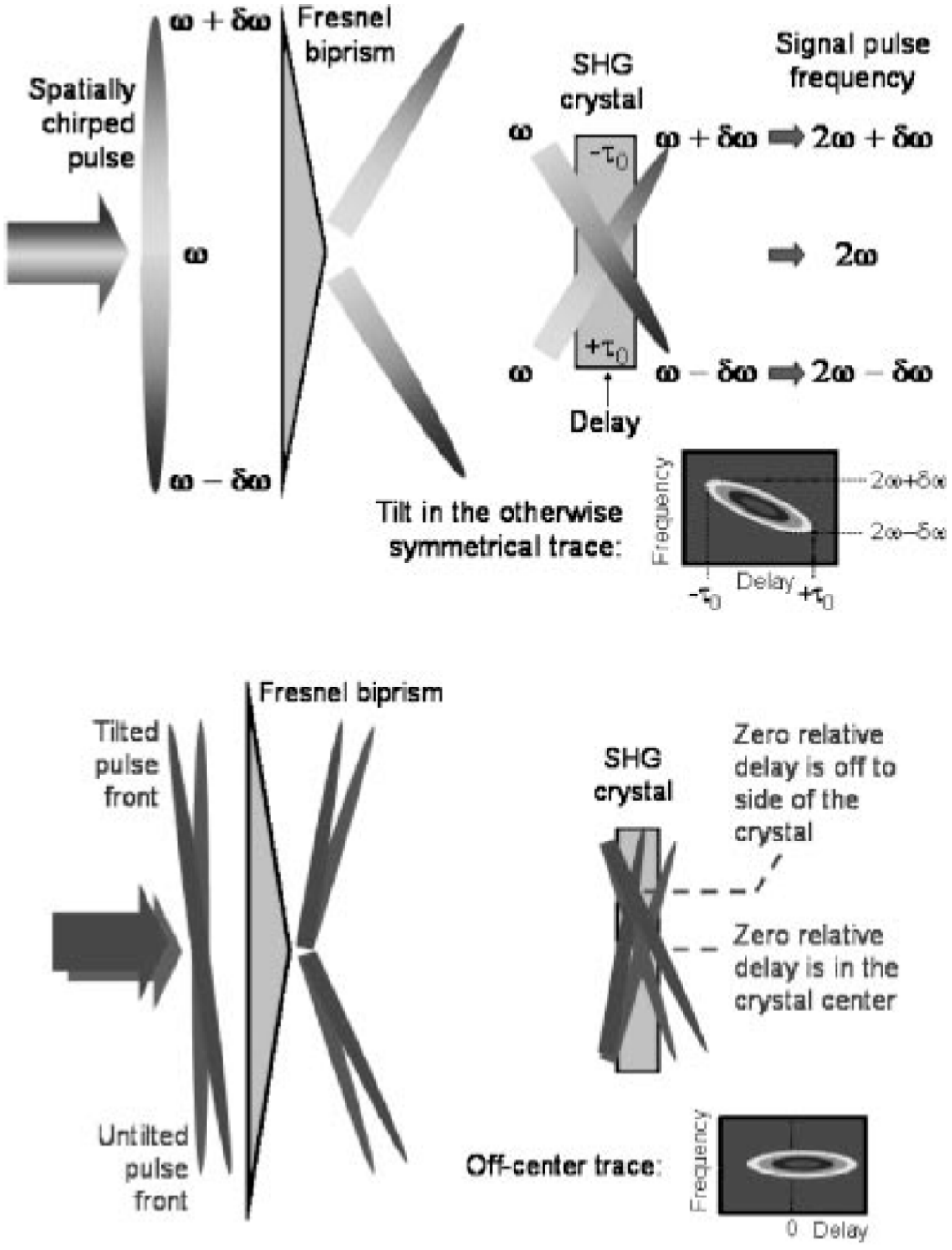

Figure 26: Spatial chirp shears the trace (top), and pulse-front tilt translates the trace (bottom) in GRENOUILLE measurements. This allows GRENOUILLE to measure these distortions easily and without modification to the apparatus.

enough to possess a phase-matching bandwidth larger than that of the pulse to be measured. GRENOUILLE intentionally uses a very thick (several mm) SHG crystal. The thick crystal only phase-matches a small spectral portion of the pulse bandwidth about the crystal's phase-matching wavelength, and the value of the phase-matching wavelength depends on the crystal angle in a nearly linear fashion. In GRENOUILLE, a focused beam which contains a range of input angles is brought into the SHG crystal, generating a fan of second-harmonic (SH) beams whose wavelengths depend on the angles. A subsequent Fourier-transform lens maps angle onto position on the CCD camera. Thereby, the thick crystal not only achieves the phase-matching bandwidth for the pulse measurement, but also replaces the spectrometer in a FROG device.

Delay generation by the Fresnel biprism and spectral resolution by the thick SHG crystal are in two independent orthogonal dimensions. Because delay is generated spatially as is in all single-shot techniques, it is conceivable that spatio-temporal distortion in the dimension of the Fresnel biprism operation will impart its effect onto the resultant trace, which then can in turn be used to measure the distortion. In the following work, we will assume that the input beam contains spatio-temporal distortion in the Fresnel biprism operation dimension x only, while the orthogonal dimension is distortion-free. The function of the think SHG crystal can be modeled as an ideal Fourier transformer.

If we write the input spatio-temporal electric field as $E_{\text{in}}(x,\omega)$, the electric field after the Fresnel biprism is:

$$E_{\text{Fres}}(x,\omega) = \begin{cases} E^{+}_{\text{Fres}}(x,\omega) = E_{\text{in}}(x,\omega)\exp(-ik\theta x) & \text{for } x<0; \\ E^{-}_{\text{Fres}}(x,\omega) = E_{\text{in}}(x,\omega)\exp(ik\theta x) & \text{for } x>0. \end{cases} \tag{41}$$

Beamlets on both sides of the biprism cross the z axis at angle θ, in opposite directions.

After propagating distance of L to the SHG crystal, both beamlets shift laterally by $L\theta$, in opposite directions (neglecting any hard-edge diffraction effects) (Figure 27),

$$\begin{cases} E^{-}(x,\omega) = E(x-L\theta,\omega)\exp(-ik\theta x) & \text{for } x<L\theta; \\ E^{+}(x,\omega) = E(x+L\theta,\omega)\exp(ik\theta x) & \text{for } x>-L\theta. \end{cases} \tag{42}$$

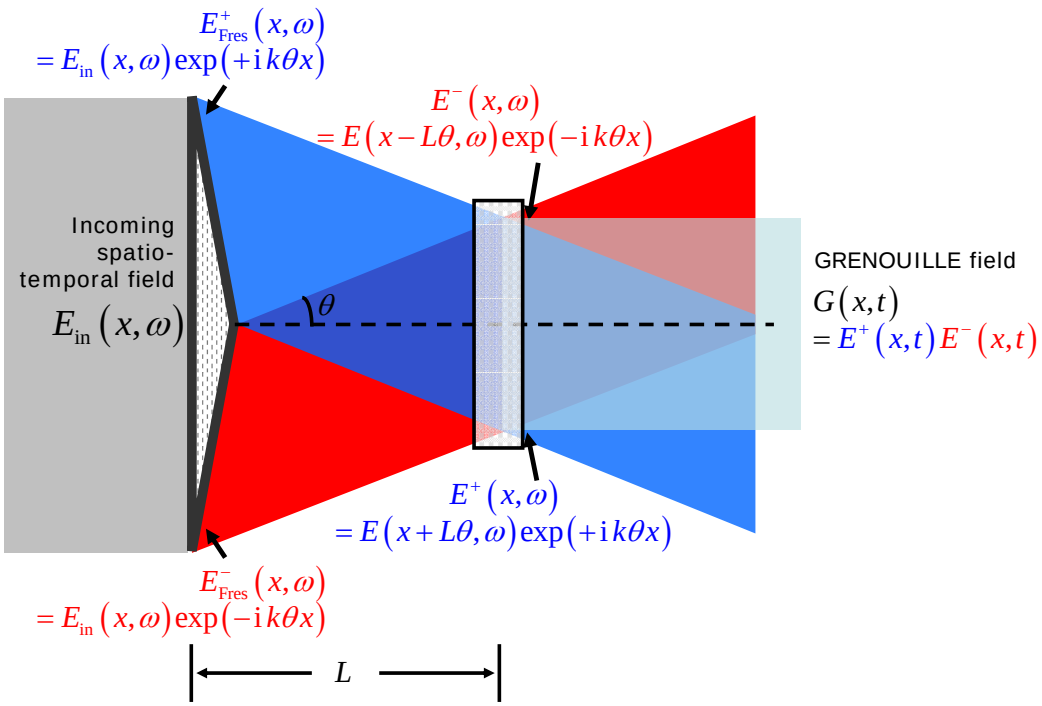

Figure 27: Schematic diagram of rigorous GRENOUILLE theory with arbitrary input spatio-temporal field

where $E(x,\omega)$ is the spatio-temporal field at the crystal location (if the Fresnel biprism were non-existent). GRENOUILLE measures the spatio-temporal distortion in $E(x,\omega)$ at the crystal location. As has been shown in the previous chapter, spatio-temporal parameters evolve with propagation, but the evolution is easy to model and calculate. Therefore, it is sufficient to measure the spatio-temporal parameters at any longitudinal position. Calculating the parameters at positions other than the crystal involves only simple mathematics.

Eq. (42) is an expression of the electric field in the x-ω domain. To write the field in the x-t domain, we first need to write out the ω-dependence of the wavenumber k explicitly:

$$k = k_0 + \frac{\omega}{c} \tag{43}$$

where $k_0 = \omega_0/c$ is the wavenumber corresponding to the center frequency of the beam, and ω is the shift from the center frequency, as is the convention we have used in the previous two chapters.

Substituting Eq. (43) into Eq. (42), we obtain

$$\begin{cases} E^-(x,\omega) = E(x - L\theta, \omega)\exp(-ik_0\theta x)\exp(-i\omega\theta x/c) & \text{for } x < L\theta; \\ E^+(x,\omega) = E(x + L\theta, \omega)\exp(ik_0\theta x)\exp(i\omega\theta x/c) & \text{for } x > -L\theta. \end{cases} \tag{44}$$

Invoking the shift theorem, we may inversely Fourier-transform Eq. (44) into the x-t domain,

$$\begin{cases} E^-(x,t) = E\left(x - L\theta, t - \theta x/c\right)\exp(-ik_0\theta x) & \text{for } x < L\theta; \\ E^+(x,t) = E\left(x + L\theta, t + \theta x/c\right)\exp(ik_0\theta x) & \text{for } x > -L\theta. \end{cases} \tag{45}$$

The second-harmonic GRENOUILLE signal is generated in the SHG crystal only in the region where the two beamlets overlap ($-L\theta < x < L\theta$). The signal is spectrally resolved by the combined action of the thick SHG crystal and the Fourier-transform lens. The GRENOUILLE trace—image directly captured on the CCD camera—can therefore be represented as:

$$\begin{aligned} G(x,\omega) &= \left| \int E^+(x,t)E^-(x,t)\exp(-i\omega t)\mathrm{d}t \right|^2 \\ &= \left| \int E\left(x - L\theta, t - \theta x/c\right) E\left(x + L\theta, t + \theta x/c\right)\exp(-i\omega t)\mathrm{d}t \right|^2 \end{aligned} \tag{46}$$

Eq. (46) is the main result of our rigorous theory. It applies to an arbitrary input one-dimensional spatio-temporal field, with no assumptions being made about the pulse shape or spatial profile.

9.3 Effects of Spatio-Temporal Distortions to GRENOUILLE Traces

In this section, we will apply our rigorous theory to study how the GRENOUILLE trace is affected by the spatio-temporal distortions in the input beam.

We start with the simplest case ever—no spatio-temporal distortions. In this case, spatial and temporal dependences can be separated: $E(x,t) = f(x)E(t)$. The GRENOUILLE trace is then

$$\begin{aligned} G(x,\omega) &= \left| \int f(x-L\theta) E\left(t-\frac{\theta x}{c}\right) f(x+L\theta) E\left(t+\frac{\theta x}{c}\right) \exp(-i\omega t)\mathrm{d}t \right|^2 \\ &= \left| \int F(x)E(t)E\left(t-\frac{2\theta x}{c}\right) \exp(-i\omega t)\mathrm{d}t \right|^2 \\ &= |F(x)|^2 I_{\mathrm{FROG}}\left(\frac{2\theta x}{c},\omega\right) \end{aligned} \tag{47}$$

where

$$F(x) = f(x-L\theta) f(x+L\theta) \tag{48}$$

and $I_{\mathrm{FROG}}(\tau,\omega) = \left|\int E(t)E(t-\tau)\exp(-i\omega t)\mathrm{d}t\right|^2$ (Eq. 5) is the standard SHG-FROG trace.

Therefore, a GRENOUILLE trace in the ideal spatio-temporal-distortion-free case is a standard SHG-FROG trace with delay $\tau = 2\theta x/c$, its intensity weighted by the input beam spatial profile.

Adding spatio-temporal distortion to the input beam distorts the GRENOUILLE trace, according to Eq. (46). We shall first consider a simple case: the GRENOUILLE trace of a linearly chirped Gaussian pulse, with a Gaussian spatial profile, under first-order spatio-temporal distortions.

The input field can be written in the x-ω domain as

$$E(x,\omega) = E_0 \exp\left(-\frac{\omega^2\tau_0^2}{4}\right) \exp\left[-\frac{(x-\zeta\omega)^2}{w^2}\right] \exp\left(-i\frac{\varphi^{(2)}}{2}\omega^2\right) \exp\left(-ik\beta\omega x\right) \tag{49}$$

As is shown in Chapter 8, the expression of the field in the x-t domain is [Eq. (28)]:

$$E(x,t) = f(x)\exp\left[-\frac{(t-px)^2}{\tau^2}\right]\exp\left\{i\left[\upsilon x(t-px)+\frac{\phi^{(2)}}{2}(t-px)^2\right]\right\} \tag{50}$$

where the definitions of the various parameters are shown in Eqs. (29).

Therefore,

$$\begin{aligned}
&E\left(x-L\theta,t-\frac{\theta x}{c}\right)E\left(x+L\theta,t+\frac{\theta x}{c}\right)\\
=&f(x-L\theta)f(x+L\theta)\exp\left\{-\frac{1}{\tau^2}\left(\left[t-\frac{\theta x}{c}-p(x-L\theta)\right]^2+\left[t+\frac{\theta x}{c}-p(x+L\theta)\right]^2\right)\right\}\\
&\times\exp\left\{i\upsilon(x-L\theta)\left[t-\frac{\theta x}{c}-p(x-L\theta)\right]+i\upsilon(x+L\theta)\left[t+\frac{\theta x}{c}-p(x+L\theta)\right]\right\}\\
&\times\exp\left\{i\frac{\phi^{(2)}}{2}\left[t-\frac{\theta x}{c}-p(x-L\theta)\right]^2+i\frac{\phi^{(2)}}{2}\left[t+\frac{\theta x}{c}-p(x+L\theta)\right]^2\right\}\\
=&F(x)E'\left(t-px+pL\theta-\frac{\theta x}{c}\right)E'\left(t-px-pL\theta+\frac{\theta x}{c}\right)\\
&\times\exp\left[i2\upsilon x(t-px)\right]\exp\left[i2\upsilon L\theta\left(\frac{\theta x}{c}-pL\theta\right)\right]
\end{aligned} \tag{51}$$

where

$$E'(t) = \exp\left[-\left(\frac{t}{\tau}\right)^2\right]\exp\left[i\frac{\phi^{(2)}}{2}t^2\right] \tag{52}$$

is the pulse locally measured at the center of the beam.

Substituting Eq. (51) into Eq. (46), we obtain the GRENOUILLE trace under spatio-temporal distortion

$$\begin{aligned}
G(x,\omega) &= \left|\int E(t-\frac{\theta x}{c})E(t+\frac{\theta x}{c})\exp(-i\omega t)\mathrm{d}t\right|^2\\
&= \left|\int F(x)E'\left(t-px+pL\theta-\frac{\theta x}{c}\right)E'\left(t-px-pL\theta+\frac{\theta x}{c}\right)\exp\left[i2\upsilon x(t-px)\right]\mathrm{d}t\right|^2\\
&= |F(x)|^2\left|\int E'\left(t+pL\theta-\frac{\theta x}{c}\right)E'\left(t-pL\theta+\frac{\theta x}{c}\right)\exp(i2\upsilon xt)\mathrm{d}t\right|^2\\
&= |F(x)|^2 I'_{\mathrm{FROG}}\left(\frac{2\theta x}{c}-2pL\theta,\omega-2\upsilon x\right)
\end{aligned} \tag{53}$$

where $I'_{\mathrm{FROG}}(\tau,\omega) = \left|\int E'(t)E'(t-\tau)\exp(-i\omega t)\mathrm{d}t\right|^2$ is the standard SHG-FROG trace of the local pulse $E'(t)$.

If we define $\tau = \frac{2\theta}{c}x$,

$$G(x,\omega) = |F(x)|^2 \, I'_{\mathrm{FROG}}\left(\tau - 2pL\theta, \omega - \frac{\upsilon c}{\theta}\tau\right) \tag{54}$$

Eq. (54) shows that under spatio-temporal distortions, the GRENOUILLE trace undergoes two transformations from an SHG-FROG trace of the local pulse:

1. Shear in the frequency axis due to spatial chirp. The shear value is determined by the frequency gradient parameter υ:

$$\frac{\delta\omega}{\delta\tau} = \frac{\upsilon c}{\theta} \tag{55}$$

2. Shift in the delay axis due to pulse-front tilt. The amount of shift is:

$$\Delta\tau = 2pL\theta \tag{56}$$

These results are in perfect agreement with the intuitive physical explanations from Refs. [6] and [5].

9.4 Algorithm for Retrieving Spatio-Temporal Distortions from GRENOUILLE Trace

In the previous section, we have shown that under spatial chirp and pulse-front tilt, a GRENOUILLE trace undergoes a transformation characterized by Eq. (46). Such a transformation does not obey the delay-axis symmetry of a standard SHG-FROG trace, and hence can in principal be used to measure the value of spatio-temporal distortions.

If the input pulse-beam is a linearly chirped Gaussian pulse, or more generally, if the input beam can be written in the x-t domain using first-order frequency gradient υ and pulse-front tilt p as:

$$E(x,t) = f(x)E'(t - px)\exp[i\upsilon x(t - px)] \tag{57}$$

where $E'(t)$ is the pulse locally measured at the center of the beam, it is easy to show that the GRENOUILLE trace under distortion is

$$G(x,\omega) = |F(x)|^2 \, I'_{\mathrm{FROG}}\left(\tau - 2pL\theta, \omega - \frac{\upsilon c}{\theta}\tau\right) \tag{58}$$

where $I'_{\mathrm{FROG}}(\tau,\omega) = \left|\int E'(t)E'(t-\tau)\exp(-i\omega t)\mathrm{d}t\right|^2$, $F(x) = f(x-L\theta)f(x+L\theta)$ and $\tau = \dfrac{2\theta}{c}x$. Namely, the transformation can be described as a frequency-axis shear due to spatial chirp and a delay-axis shift due to pulse-front tilt.

Frequency-axis shear and delay-axis shift in a SHG-FROG trace are easy to measure and quantify. Their use in measuring spatial chirp and pulse-front tilt has already been demonstrated ([6] and [5]). In addition, the GRENOUILLE measurement of pulse-front tilt has been shown to be the most sensitive technique to date.

Eq. (57) may seem quite general, but in fact, it cannot describe many common experimental beams. The key problem is that in writing Eq. (57), we assume that the temporal pulse form is invariant across the beam (so the trace transformation starts from the FROG trace of a local invariant pulse), except for a position-linear frequency shift described by the frequency gradient parameter υ. Fourier transform of Eq. (57) yields

$$E\left(x,\omega\right) = f\left(x\right)\tilde{E}'\left(\omega-\upsilon x\right)\exp\left(-ip\omega x\right) \tag{59}$$

in the x-ω domain.

In experimental laser beams, spatial chirp is almost always generated via angular dispersion, so the field should be written in the x-ω domain as

$$E(x,\omega) = E(\omega)f(x-\zeta\omega)\exp\left(-ik\beta\omega x\right) \tag{60}$$

Eqs. (59) and (60) are both special cases of the general spatio-spectral field $E(x,\omega)$, but it should be noted that they imply different assumptions about the beam. The key issue is that, with a complicated pulse form, the two equations are not compatible, and whereas Eq. (60) is a reasonable assumption to make for experimental beams, Eq. (59) is not.

It is very important to note that we always discuss spatio-temporal distortions in the context of a well-collimated beam. If the physics of rapid convergence or divergence were included, the spatio-temporal analysis would be unnecessarily much more complicated. If all the frequency components are well collimated in the beam, their phase fronts are all considered to be flat. Therefore, aside from a linear spatial phase factor $\exp\left(-ik\beta\omega x\right)$ which characterizes angular dispersion, the phase of the spatio-spectral field $E(x,\omega)$ should

be x-independent. Eq. (60) satisfies this important assumption. Indeed, with $f(x)$ being real and ignoring angular dispersion, $\arg\{E(x,\omega)\} = \arg\{E(\omega)\}$ is independent of x.

Eq. (59), on the other hand, is not compatible with the assumption of a well-collimated beam. This can be seen in that if $\tilde{E}'(\omega)$ has a complicated phase, again ignoring linear spatial phase, $\arg\{E(x,\omega)\} = \arg\{f(x)\} + \arg\{\tilde{E}'(\omega - \upsilon x)\}$ will always have an x-dependence, mandating that its frequency components be not collimated. What's more discomforting is that the complexity of the phase fronts of constituent frequencies would be affected by the complexity of the pulse's spectral phase, a totally unacceptable assumption. A similar problem also exists for the intensity. If the intensity of $\tilde{E}'(\omega)$ is not Gaussian, the conversion of $|E(\omega)f(x-\zeta\omega)|$ to $|f(x)\,\tilde{E}'(\omega - \upsilon x)|$ is also problematic.

In view of these problems, it is necessary to use Eq. (60) instead of Eq. (59) to describe an experimental beam with spatio-temporal distortions. This is important for the interpretation of a spatio-temporally distorted GRENOUILLE trace experimentally, as GRENOUILLE, being a pulse characterization device, is designed to measure complicated pulses. Using Eq. (59), as we have shown before, the distortion of a GRENOUILLE trace would only be a frequency-axis shear under spatial chirp, and the shear value would be entirely determined by spatial chirp, as predicted by the simple theory in Ref. [6]. In an experimental beam, this is often not the case. For example, the existence of cubic spectral phase in a spatially chirped Gaussian pulse-beam causes the GRENOUILLE trace to exhibit an apparent delay-axis shear (Figure 28), whose value also depends on the cubic-phase coefficient.

Clearly, to measure spatio-temporal distortion reliably for all pulse shapes and phases, one needs to resort to the rigorous GRENOUILLE theory described in Section 9.2, where no assumptions about the pulse or beam characteristics are made, and use Eq. (60) as the form of the input spatio-spectral field. However, that also means that the current FROG algorithm cannot be used for the purpose of temporal domain pulse retrieval, as the spatio-temporal distortion parameters are buried deep in the kernel, and to retrieve them or the temporal/spectral pulse characteristics now requires a complete overhaul of the algorithm. Nevertheless, the development of such an algorithm is under way, which,

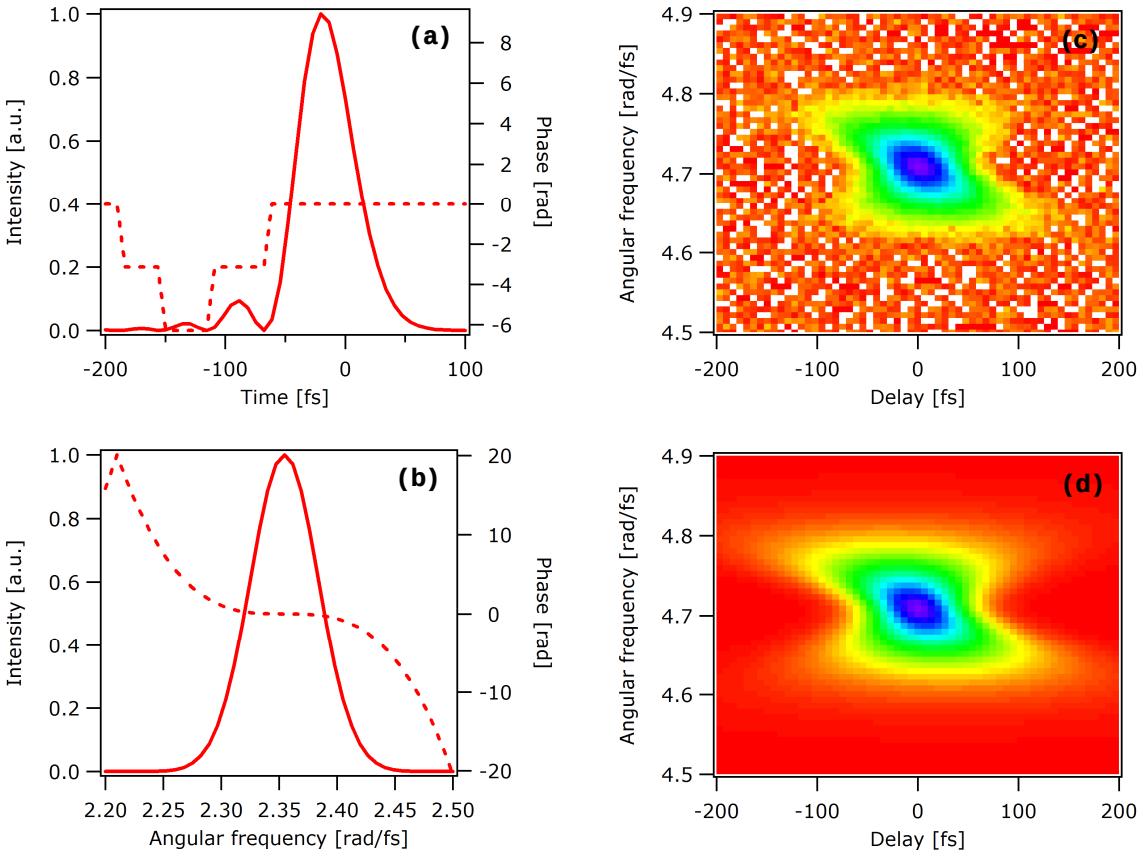

Figure 28: Results of retrieving spatial chirp from a GRENOUILLE trace under spatio-temporal distortion: (a) Temporal and (b) spectral intensity and phase of a cubic-spectral-phase pulse. (c) Simulated GRENOUILLE trace of the pulse with spatial dispersion $\zeta = \mathrm{d}x/\mathrm{d}\omega = 30$ mm/(fs $\cdot$ rad^{-1}). Additive 1% Gaussian noise has been imposed. Note that the trace has an apparent delay-axis shear, which is inconsistent with the simple theory's prediction of frequency-axis shear. (d) Reconstructed GRENOUILLE trace using the algorithm described in the text and the simulated noisy trace as input. Retrieved spatial dispersion value is $\zeta = 29.9$ mm/(fs $\cdot$ rad^{-1}). The Levenberg-Marquardt method is used for the one-dimensional minimization of ζ.

upon its completion, will be an important development in the field of spatio-temporal field characterization.

If the spatio-temporal distortion is small, there may be simpler approximate approaches that could still work fairly well for the measurement of spatio-temporal distortions. One such algorithm can be described as follows:

When the distortion is small, the GRENOUILLE trace under distortion must still be quite similar to an ideal distortion-free trace. Running the commercial FROG algorithm on this distorted trace (or a symmetrized version of it) will most likely return a pretty good estimation of the temporal pulse form, locally at the center of the beam. Using that approximate retrieval result as an input to Eqs. (60) and (46), a few-dimensional optimization routine can be used to retrieve the spatio-temporal coupling parameters. Although such an approach is only approximate in nature, tests show that its performance is quite good, even with a moderate level of noise (Figure 28). Its major advantage is, of course, minimal code development and superior speed. Because this method only requires a fast few-dimensional optimization step after the normal FROG retrieval procedure, this implementation of spatio-temporal characterization is a very simple adaptation of the current well-tested FROG code, while capable of offering users additional outputs of spatio-temporal distortion in a wide array of cases.

Spatio-temporal dynamics of ultrafast laser beams is a fast growing field, which is gaining increasing attention in recent years. There will no doubt be new developments in the characterization techniques in the future. Hopefully, theoretical and experimental results contained in this thesis will be useful background for future researchers in this field.

APPENDIX A

COLLIMATING MICROSTRUCTURE-FIBER SUPERCONTINUUM

This appendix originally appeared as a conference paper by the author:

Xun Gu, Lin Xu, Mark Kimmel, Patrick O'Shea, Rick Trebino, Robert S. Windeler, Charles Kerbage, and Benjamin J. Eggleton, "The problem of collimating ultra-broadband continuum from microstructure fiber," presented at the Conference on Lasers and Electro-Optics (CLEO), Baltimore, MD, May 6–11, 2001. [59]

Ultrashort laser pulse technology plays an important role in the fields of physics, chemistry, biology, etc. Ultrashort pulses allow the study of incredibly fast time scales. More importantly, the broad bandwidths of such pulses, whether the pulses are short or not, are useful for many applications, including communication, coherent control of chemical reaction, ultrahigh-spatial-resolution optical coherence tomography, and optical metrology. Recently, ultra-broadband continuum has been obtained from microstructure fibers [102]. As interesting as the potential applications of the supercontinuum are, the huge bandwidth also implies great intrinsic complexity in maneuvering and even simply collimating the beam. Hardly any optical components are designed to deal with such a broad bandwidth, and reflective optics also have their limitations. The problem is still to be solved, and we will discuss the pros and cons of several different methods in the following section.

Microstructure fibers are fabricated so that different wavelengths expand differently into the cladding (air). As the usual diffraction angle depends linearly on wavelength and inversely on waist size, one would speculate that the divergence of different wavelengths at the fiber output face would be different—and different from that of common fibers. Knowledge of the frequency dependence of divergence will certainly aid us in our effort to

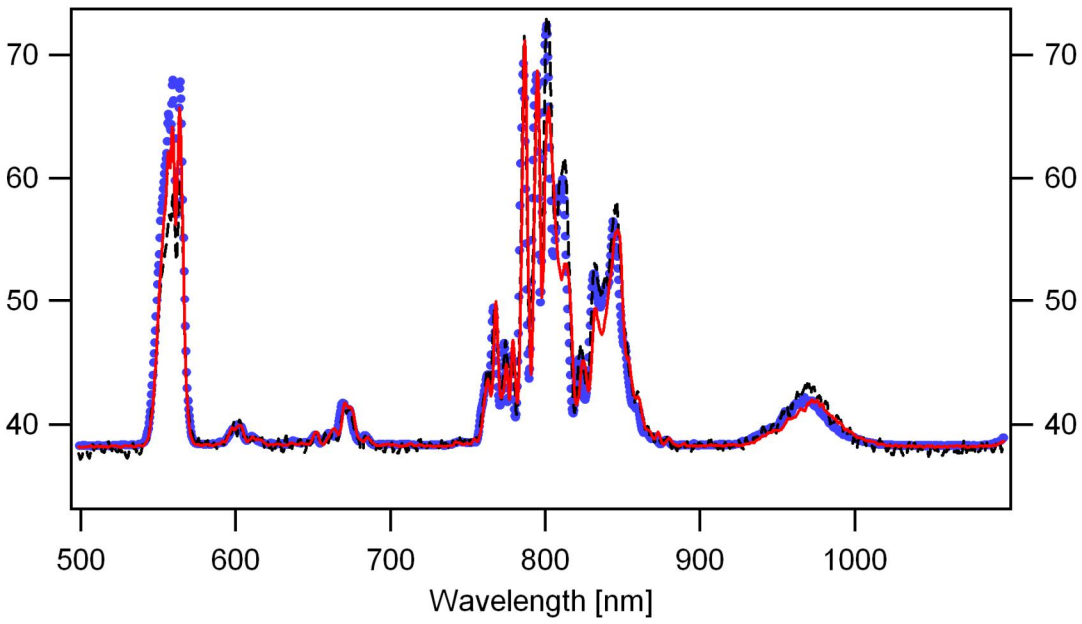

Figure 29: The spectra measured at three different locations from the output of the fiber. The curves agree well, which demonstrates little "divergence chirp."

collimate the beam. We measured the spectrum at a series of points across a plane at a certain distance away from the output face. The result (Figure 29) reveals nearly identical spectra, which means that different frequency components diverge at essentially the same angle from the fiber.

Unfortunately, the divergence angle is as large as 60 degrees, which causes difficulties in coupling and collimating the output light.

In order to collimate the output beam, there are several known options available. One choice is a reflective (Cassegrain) microscopic objective. Widely used in optical applications, it is composed of two spherical mirrors face to face. Focused by the first mirror, the light is collimated by the second small mirror placed in the center, and sent out through the hole that is cut in the center of the large mirror. The major pitfall of this setup is though that, the majority of the output energy (the center) is blocked by the small mirror sitting in the center, disqualifying the beam from further utilization.

Alternatively, we turn to using the reflective microscopic objective off axis. The idea is to project the output light on one side of the large mirror only, to avoid the blockage by

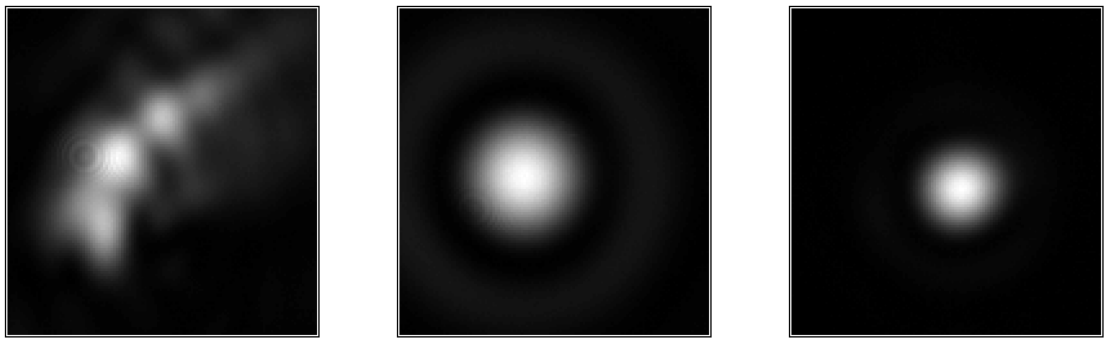

Figure 30: Far-field spatial modes from a reflective microscopic objective in the off-axis configuration (left), a triplet lens (center), and a 60× refractive microscopic objective (right).

the small mirror. However, strong astigmatism results from this abnormal use of the optic, giving an unacceptable spatial mode in the far field, as is shown in Figure A.

A third option is the off-axis paraboloid, which is a standard technique in collimation of fiber outputs. However, because the microstructure fiber has a core diameter of merely ~ 1.5 μm, the divergence angle of the output light is as large as ~ 60 degrees, which requires the use of an off-axis paraboloid of very short focal length. Off-axis paraboloids of such a size are very hard to fabricate with the precision necessary to maintain a good beam profile in the far field. Mechanical engineerability becomes the main limiting factor in this case, and we have found the results of such an optic highly unsatisfactory (the beam assumes a cross-shape a meter away).

Having exhausted the common reflective optical methods, we considered using refractive optics to deal with our continuum. We have considered triplet lenses and refractive microscopic objectives. Although they do give good beam shape, as shown in Figure A, there exists a huge problem of using them to deal with the supercontinuum—chromatic aberration. Most lenses are designed for one or several wavelengths only; never are they intended to operate with such a huge bandwidth that we have. Therefore, chromatic aberration is expected, and is observed in our measurement. In Figure 31, we show the spectra measured at several locations in the beam. Obviously, the weight of different frequency components changes as we move our detector across the beam, which implies that those components

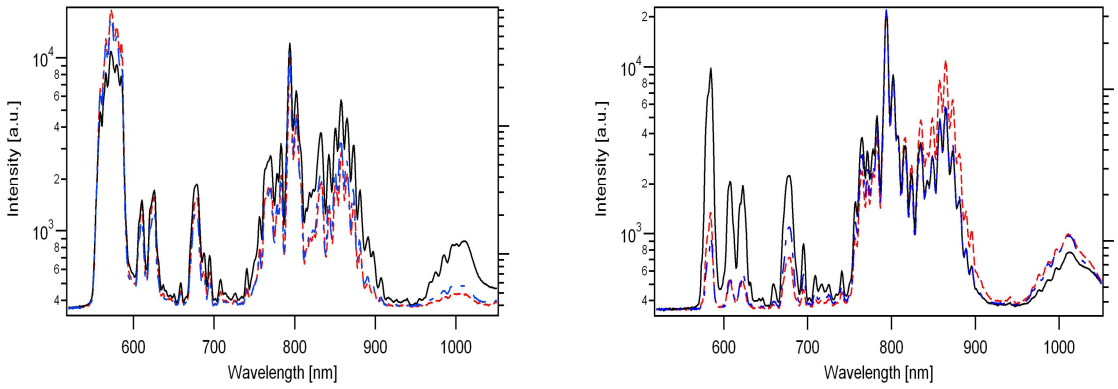

Figure 31: Spectra measured at three different locations in the beam as we try to collimate using a triplet (left) and a 60× refractive microscopic objective (right). The solid line is the measured spectrum in the center of the beam, while the two other curves are measured on the sides. It can be easily seen that chromatic aberration exists in both scenarios.

propagate in different manners in space. This is a severe problem in the far field, as the colors begin to separate significantly, causing great difficulty in phase-matching, or any other operation involving theis light. We have gone to great lengths looking for solutions, but a perfect answer has yet to be found. As the applications of the supercontinuum begin to attract more and more people's attention, we feel that it may be helpful to point out the existing difficulties in dealing with the light, and we hope they might get addressed in the near future. Indeed, the solution may be Lucent's newly developed tapered-core microstructure fiber, whose core increases gradually to as much as 8 μm at the output. This will decrease the divergence angle of the continuum from about 60 degrees to $\sim$ 10 degrees, allowing off-axis reflective mirrors to suffice.

APPENDIX B

KOSTENBAUDER MATRIX FORMALISM

We have shown above that simultaneous temporal and spatial chirp cause pulse-front tilt even in the absence of angular dispersion. Here, we provide an alternative derivation using the matrix formalism introduced by Martinez [89, 88] and extended by Kostenbauder [80].

An optical system that introduces spatial and temporal chirp can be described in terms of a 4×4 ray-pulse matrix as:

$$K = \begin{bmatrix} A & B & 0 & E \\ C & D & 0 & F \\ G & H & 1 & I \\ 0 & 0 & 0 & 1 \end{bmatrix} = \begin{bmatrix} 1 & L & 0 & 2\pi\zeta \\ 0 & 1 & 0 & 0 \\ 0 & -2\pi\zeta/\lambda_0 & 1 & 2\pi\varphi^{(2)} \\ 0 & 0 & 0 & 1 \end{bmatrix} \tag{61}$$

where ζ is spatial dispersion and $\varphi^{(2)}$ is group-delay dispersion.

Matrix K can be obtained either by calculating the system ray-pulse matrix for a two-prism pulse compressor separated by L or for a fictitious system that introduces only spatial chirp followed by a dispersive slab of thickness nL (where $n = n(\omega)$ is the index of refraction). In both cases, GDD is the total GDD due to both the material and angular dispersions. Note that this approach describes only rays or plane waves, so the matrix shows no pulse-front tilt ($K_{31} = \dfrac{\partial t}{\partial x} = 0$), as we expect.

In order to apply the ray-pulse matrix to a finite-size Gaussian beam, we must use the complex Q matrix, as illustrated by Kostenbauder in Ref. [11]. Using this approach, the spatio-temporal electric field is expressed as:

$$\begin{aligned} E(x,t) &= \exp\left\{-i\frac{\pi}{\lambda_0}\begin{pmatrix} x \\ -t \end{pmatrix}^T Q^{-1}\begin{pmatrix} x \\ t \end{pmatrix}\right\} \\ &= \exp\left[-i\frac{\pi}{\lambda_0}\left(Q_{11}^{-1}x^2 + Q_{12}^{-1}xt - Q_{21}^{-1}xt - Q_{22}^{-1}t^2\right)\right] \end{aligned} \tag{62}$$

The off-diagonal elements of the matrix Q^{-1} indicate spatial-temporal coupling. We may write the electric-field magnitude in terms of local pulse length and pulse-front tilt as

$$|E(x,t)| \propto \exp\left[-\frac{(t-px)^2}{\tau^2}\right] \tag{63}$$

Equating the magnitudes of (62) and (63) yields

$$\tau = \left[\frac{\pi}{\lambda_0}\operatorname{Im}\left\{Q_{22}^{-1}\right\}\right]^{-1/2} \tag{64}$$

$$p = \frac{\pi\tau^2}{2\lambda_0}\operatorname{Im}\left\{Q_{12}^{-1} - Q_{21}^{-1}\right\} = \frac{\operatorname{Im}\left\{Q_{12}^{-1} - Q_{21}^{-1}\right\}}{2\operatorname{Im}\left\{Q_{22}^{-1}\right\}} \tag{65}$$

For an input pulse with no spatio-temporal distortions and flat phase, we have:

$$\left(Q_{\text{in}}^{-1}\right)_{11} = \frac{1}{q} \tag{66a}$$

$$\left(Q_{\text{in}}^{-1}\right)_{22} = i\frac{\lambda_0}{\pi\tau_0^2} \tag{66b}$$

Then the input Q matrix is:

$$Q_{\text{in}} = \begin{bmatrix} q & 0 \\ 0 & -i\dfrac{\pi\tau_0^2}{\lambda_0} \end{bmatrix} \tag{67}$$

The output Q matrix is found by:

$$Q_{\text{out}} = \left(\begin{bmatrix} A & 0 \\ G & 1 \end{bmatrix} Q_{\text{in}} + \begin{bmatrix} B & E/\lambda_0 \\ H & I/\lambda_0 \end{bmatrix}\right) \cdot \left(\begin{bmatrix} C & 0 \\ 0 & 1 \end{bmatrix} Q_{\text{in}} + \begin{bmatrix} D & F/\lambda_0 \\ 0 & 1 \end{bmatrix}\right)^{-1} \tag{68}$$

Substituting the elements of K from Eq. (61) into (68), we obtain:

$$Q_{\text{out}} = \begin{bmatrix} q+L & \dfrac{2\pi\zeta}{\lambda_0} \\ -\dfrac{2\pi\zeta}{\lambda_0} & \dfrac{2\pi\varphi^{(2)}}{\lambda_0} - i\dfrac{\pi\tau_0^2}{\lambda_0} \end{bmatrix} \tag{69}$$

Inverting this matrix yields:

$$Q_{\text{out}}^{-1} = \begin{bmatrix} \dfrac{\lambda_0\left(\varphi^{(2)} - \dfrac{i}{2}\tau_0^2\right)}{\varphi^{(2)}(L+q)\lambda_0 + 2\pi\zeta^2 - \dfrac{i}{2}(L+q)\lambda_0\tau_0^2} & -\dfrac{\lambda_0\zeta}{\varphi^{(2)}(L+q)\lambda_0 + 2\pi\zeta^2 - \dfrac{i}{2}(L+q)\lambda_0\tau_0^2} \\ \dfrac{\lambda_0\zeta}{\varphi^{(2)}(L+q)\lambda_0 + 2\pi\zeta^2 - \dfrac{i}{2}(L+q)\lambda_0\tau_0^2} & \dfrac{1}{2\pi}\dfrac{(L+q)\lambda_0^2}{\varphi^{(2)}(L+q)\lambda_0 + 2\pi\zeta^2 - \dfrac{i}{2}(L+q)\lambda_0\tau_0^2} \end{bmatrix} \tag{70}$$

For a well collimated beam, we can approximate:

$$q\left(L\right)=L+q\approx i\frac{\pi w^{2}}{\lambda_{0}} \tag{71}$$

Therefore,

$$Q_{\text{out}}^{-1}=\left[\begin{array}{cc}\frac{\lambda_{0}}{\pi}\frac{2\varphi^{(2)}-i\tau_{0}^{2}}{4\zeta^{2}+w^{2}\tau_{0}^{2}+i2\varphi^{(2)}w^{2}} & -\frac{2\lambda_{0}}{\pi}\frac{\zeta}{4\zeta^{2}+w^{2}\tau_{0}^{2}+i2\varphi^{(2)}w^{2}}\\ \frac{2\lambda_{0}}{\pi}\frac{\zeta}{4\zeta^{2}+w^{2}\tau_{0}^{2}+i2\varphi^{(2)}w^{2}} & i\frac{\lambda_{0}}{\pi}\frac{w^{2}}{4\zeta^{2}+w^{2}\tau_{0}^{2}+i2\varphi^{(2)}w^{2}}\end{array}\right] \tag{72}$$

Using Eqs. (64) and (65), we find

$$\tau=\left[\tau_{0}^{2}+\frac{4\zeta^{2}}{w^{2}}+\frac{4\left(\varphi^{(2)}\right)^{2}}{\tau_{0}^{2}+\frac{4\zeta^{2}}{w^{2}}}\right]^{1/2} \tag{73}$$

$$p=\frac{\varphi^{(2)}\zeta}{\zeta^{2}+\frac{1}{4}w^{2}\tau_{0}^{2}} \tag{74}$$

which are identical to the results we obtained in Chapter 8.

REFERENCES

[1] Abedin, K. S., Gopinath, J. T., Ippen, E. P., Kerbage, C. E., Windeler, R. S., and Eggleton, B. J., "Highly nondegenerate femtosecond four-wave mixing in tapered microstructure fiber," *Applied Physics Letters*, vol. 81, no. 8, pp. 1384–1386, 2002.

[2] Agrawal, G. P., *Nonlinear Fiber Optics*. Optics and photonics, San Diego: Academic Press, 3rd ed., 2001.

[3] Akhmediev, N. and Karlsson, M., "Cherenkov radiation emitted by solitons in optical fibers," *Physical Review A*, vol. 51, no. 3, pp. 2602–2607, 1995.

[4] Akimov, D. A., Serebryannikov, E. E., Zheltikov, A. M., Schmitt, M., Maksimenka, R., Kiefer, W., Dukel'skii, K. V., Shevandin, V. S., and Kondrat'ev, Y. N., "Efficient anti-Stokes generation through phase-matched four-wave mixing in higher-order modes of a microstructure fiber," *Optics Letters*, vol. 28, no. 20, pp. 1948–1950, 2003.

[5] Akturk, S., Kimmel, M., O'Shea, P., and Trebino, R., "Measuring pulse–front tilt in ultrashort pulses using GRENOUILLE," *Optics Express*, vol. 11, no. 5, pp. 491–501, 2003.

[6] Akturk, S., Kimmel, M., O'Shea, P., and Trebino, R., "Measuring spatial chirp in ultrashort pulses using single-shot frequency-resolved optical gating," *Optics Express*, vol. 11, no. 1, pp. 68–78, 2003.

[7] Arbore, M. A., Galvanauskas, A., Harter, D., Chou, M. H., and Fejer, M. M., "Engineerable compression of ultrashort pulses by use of second-harmonic generation in chirped-period-poled lithium niobate," *Optics Letters*, vol. 22, no. 17, pp. 1341–1343, 1997.

[8] Baltuska, A., Pshenichnikov, M., and Wiersma, D., "Second-harmonic generation frequency-resolved optical gating in the single-cycle regime," *IEEE Journal of Quantum Electronics*, vol. 35, no. 4, pp. 459–478, 1999.

[9] Baum, P., Lochbrunner, S., Piel, J., and Riedle, E., "Phase-coherent generation of tunable visible femtosecond pulses," *Optics Letters*, vol. 28, no. 3, pp. 185–187, 2003.

[10] Bellini, M. and Hänsch, T. W., "Phase-locked white-light continuum pulses: toward a universal optical frequency-comb synthesizer," *Optics Letters*, vol. 25, no. 14, pp. 1049–1051, 2000.

[11] Birks, T. A., Wadsworth, W. J., and Russell, P. S., "Supercontinuum generation in tapered fibers," *Optics Letters*, vol. 25, no. 19, pp. 1415–1417, 2000.

[12] Birks, T., Knight, J., and Russell, P., "Endlessly single-mode photonic crystal fiber," *Optics Letters*, vol. 22, no. 13, pp. 961–963, 1997.

[13] Bor, Z. and Racz, B., "Group-velocity dispersion in prisms and its application to pulse-compression and traveling-wave excitation," *Optics Communications*, vol. 54, no. 3, pp. 165–170, 1985.

[14] Bor, Z., Racz, B., Szabo, G., Hilbert, M., and Hazim, H. A., "Femtosecond pulse front tilt caused by angular-dispersion," *Optical Engineering*, vol. 32, no. 10, pp. 2501–2504, 1993.

[15] Boyd, R. W., *Nonlinear Optics*. Boston: Academic Press, c1992.

[16] Bruck, Y. and Sodin, L., "On the ambiguity of the image reconstruction problem," *Optics Communications*, vol. 30, no. 3, pp. 304–308, 1979.

[17] Buck, J. A., *Fundamentals of Optical Fibers*. John Wiley & Sons, Inc., 1995.

[18] Cao, Q., Gu, X., Zeek, E., Kimmel, M., Trebino, R., Dudley, J., and Windeler, R. S., "Measurement of the intensity and phase of supercontinuum from an 8-mm-long microstructure fiber," *Applied Physics B*, vol. 77, no. 2-3, pp. 239–244, 2003.

[19] Christov, I. P., Michailov, N. I., and Danailov, M. B., "Mode-locking with spatial-dispersion in the gain medium," *Applied Physics B*, vol. 53, no. 2, pp. 115–118, 1991.

[20] Chung, J.-H. and Weiner, A. M., "Ambiguity of ultrashort pulse shapes retrieved from the intensity autocorrelation and the power spectrum," *IEEE Journal of Selected Topics in Quantum Electronics*, vol. 7, no. 4, pp. 656–666, 2001.

[21] Clement, T. S., Taylor, A. J., and Kane, D. J., "Single-shot measurement of the amplitude and phase of ultrashort laser pulses in the violet," *Optics Letters*, vol. 20, no. 1, pp. 70–72, 1995.

[22] Coen, S., Chau, A. H. L., Leonhardt, R., Harvey, J. D., Knight, J. C., Wadsworth, W. J., and Russell, P. S. J., "Supercontinuum generation by stimulated Raman scattering and parametric four-wave mixing in photonic crystal fibers," *Journal of the Optical Society of America B*, vol. 19, no. 4, pp. 753–764, 2002.

[23] Cohen, L., *Time-Frequency Analysis*. Englewood Cliffs, NJ: Prentiss-Hall, 1995.

[24] Cormack, I. G., Reid, D. T., Wadsworth, W. J., Knight, J. C., and Russell, P. S. J., "Observation of soliton self-frequency shift in photonic crystal fibre," *Electronics Letters*, vol. 38, no. 4, pp. 167–169, 2002.

[25] Corwin, K. L., Newbury, N. R., Dudley, J. M., Coen, S., Diddams, S. A., Washburn, B. R., Weber, K., and Windeler, R. S., "Fundamental amplitude noise limitations to supercontinuum spectra generated in a microstructured fiber," *Applied Physics B*, vol. 77, no. 2–3, pp. 269–277, 2003.

[26] Cregan, R. F., Mangan, B. J., Knight, J. C., Birks, T. A., Russell, P. S., Roberts, P. J., and Allan, D. C., "Single-mode photonic band gap guidance of light in air," *Science*, vol. 285, no. 5433, pp. 1537–1539, 1999.

[27] Cristiani, I., Tediosi, R., Tartara, L., and Degiorgio, V., "Dispersive wave generation by solitons in microstructured optical fibers," *Optics Express*, vol. 12, no. 1, pp. 124–135, 2004.

[28] Cucinotta, A., Selleri, S., Vincetti, L., and Zoboli, M., "Holey fiber analysis through the finite-element method," *IEEE Photonics Technology Letters*, vol. 14, no. 11, pp. 1530–1532, 2002.

[29] Delfyett, P., Shi, H., Gee, S., Nitta, I., Connolly, J., and Alphonse, G., "Joint time-frequency measurements of mode-locked semiconductor diode lasers and dynamics using frequency-resolved optical gating," *IEEE Journal of Quantum Electronics*, vol. 35, no. 4, pp. 487–500, 1999.

[30] DeLong, K., Trebino, R., Hunter, J., and White, W., "Frequency-resolved optical gating with the use of second-harmonic generation," *Journal of the Optical Society of America B*, vol. 11, no. 11, pp. 2206–2215, 1994.

[31] Diddams, S. A., Jones, D. J., Ye, J., Cundiff, S. T., Hall, J. L., Ranka, J. K., Windeler, R. S., Holzwarth, R., Udem, T., and Hansch, T. W., "Direct link between microwave and optical frequencies with a 300 THz femtosecond laser comb," *Physical Review Letters*, vol. 84, no. 22, pp. 5102–5105, 2000.

[32] Diddams, S. A., Udem, T., Bergquist, J. C., Curtis, E. A., Drullinger, R. E., Hollberg, L., Itano, W. M., Lee, W. D., Oates, C. W., Vogel, K. R., and Wineland, D. J., "An optical clock based on a single trapped $^{199}Hg^{+}$ ion," *Science*, vol. 293, no. 5531, pp. 825–828, 2001.

[33] Diddams, S., Hollberg, L., Ma, L.-S., and Robertsson, L., "Femtosecond-laser-based optical clockwork with instability $< 6.3 \times 10^{-16}$ in 1 s," *Optics Letters*, vol. 27, no. 1, pp. 58–60, 2002.

[34] Diels, J., Fontaine, J., McMichael, I., and Simoni, F., "Control and measurement of ultrashort pulse shapes (in amplitute and phase) with femtosecond accuracy," *Applied Optics*, vol. 24, no. 9, pp. 1270–1282, 1985.

[35] Dorrer, C., Kosik, E. M., and Walmsley, I. A., "Spatio-temporal characterization of the electric field of ultrashort optical pulses using two-dimensional shearing interferometry," *Applied Physics B*, vol. 74, pp. S209–S217, 2002.

[36] Dorrer, C. and Walmsley, I. A., "Simple linear technique for the measurement of space-time coupling in ultrashort optical pulses," *Optics Letters*, vol. 27, no. 21, 2002.

[37] Drummond, P. D. and Corney, J. F., "Quantum noise in optical fibers. I. stochastic equations," *Journal of the Optical Society of America B*, vol. 18, no. 2, pp. 139–152, 2001.

[38] Dudley, J. M. and Coen, S., "Coherence properties of supercontinuum spectra generated in photonic crystal and tapered optical fibers," *Optics Letters*, vol. 27, no. 13, pp. 1180–1182, 2002.

[39] Dudley, J. M., Provino, L., Grossard, N., Maillotte, H., Windeler, R. S., Eggleton, B. J., and Coen, S., "Supercontinuum generation in air-silica microstructured fibers with nanosecond and femtosecond pulse pumping," *Journal of the Optical Society of America B*, vol. 19, no. 4, pp. 765–771, 2002.

[40] Dudley, J., Barry, L., Harvey, J., Thomson, M., Thomsen, B., Bollond, P., and Leonhardt, R., "Complete characterization of ultrashort pulse sources at 1550 nm," *IEEE Journal of Quantum Electronics*, vol. 35, no. 4, pp. 441–450, 1999.

[41] Dudley, J. M., Gu, X., Xu, L., Kimmel, M., Zeek, E., O'Shea, P., Trebino, R., Coen, S., and Windeler, R. S., "Cross-correlation frequency resolved optical gating analysis of broadband continuum generation in photonic crystal fiber: simulations and experiments," *Optics Express*, vol. 10, no. 21, pp. 1215–1221, 2002.

[42] Efimov, A., Schaffer, C., and Reitze, D. H., "Programmable shaping of ultrabroad-bandwidth pulses from a Ti:sapphire laser," *Journal of the Optical Society of America B*, vol. 12, no. 10, pp. 1968–1980, 1995.

[43] Efimov, A., Taylor, A. J., Omenetto, F. G., Knight, J. C., Wadsworth, W. J., and Russell, P. S. J., "Phase-matched third harmonic generation in microstructured fibers," *Optics Express*, vol. 11, no. 20, pp. 2567–2576, 2003.

[44] Etchepare, J., Grillon, G., and Orszag, A., "Third order autocorrelation study of amplified subpicosecond laser pulses," *IEEE Journal of Quantum Electronics*, vol. 19, no. 5, pp. 775–778, 1983.

[45] Fedotov, A. B., Naumov, A. N., Konorov, S. O., Beloglazov, V. I., Mel'nikov, L. A., Skibina, N. B., Sidorov-Biryukov, D. A., Shcherbakov, A. V., and Zheltikov, A. M., "Photonic-molecule modes of a microstructure cobweb fiber," *Laser Physics*, vol. 12, no. 11, pp. 1363–1367, 2002.

[46] Fermann, M. E., Galvanauskas, A., Sucha, G., and Harter, D., "Fiber-lasers for ultrafast optics," *Applied Physics B*, vol. 65, no. 2, pp. 259–275, 1997.

[47] Fini, J. M., "Analysis of microstructure optical fibers by radial scattering decomposition," *Optics Letters*, vol. 28, no. 12, pp. 992–994, 2003.

[48] Fiorentino, M., Sharping, J. E., Kumar, P., Porzio, A., and Windeler, R. S., "Soliton squeezing in microstructure fiber," *Optics Letters*, vol. 27, no. 8, pp. 649–651, 2002.

[49] Fittinghoff, D., Bowie, J., Sweetser, J., Jennings, R., Krumbügel, M., DeLong, K., Trebino, R., and Walmsley, I., "Measurement of the intensity and phase of ultraweak, ultrashort laser pulse," *Optics Letters*, vol. 21, no. 12, pp. 884–886, 1996.

[50] Fork, R. L., Martinez, O. E., and Gordon, J. P., "Negative dispersion using pairs of prisms," *Optics Letters*, vol. 9, no. 5, pp. 150–152, 1984.

[51] Fortier, T. M., Jones, D. J., Ye, J., Cundiff, S. T., and Windeler, R. S., "Long-term carrier-envelope phase coherence," *Optics Letters*, vol. 27, no. 16, pp. 1436–1438, 2002.

[52] Fortier, T. M., Ye, J., Cundiff, S. T., and Windeler, R. S., "Nonlinear phase noise generated in air-silica microstructure fiber and its effect on carrier-envelope phase," *Optics Letters*, vol. 27, no. 6, pp. 445–447, 2002.

[53] Froehly, C., Lacourt, A., and Vienot, J., "Time impulse response and time frequency response of optical pupils. experimental confirmations and applications," *Journal of Optics (Nouvelle Revue d'Optique, Paris)*, vol. 4, no. 4, pp. 183–96, 1973.

[54] Gaeta, A. L., "Nonlinear propagation and continuum generation in microstructured optical fibers," *Optics Letters*, vol. 27, no. 11, pp. 924–926, 2002.

[55] Gallmann, L., Steinmeyer, G., Sutter, D. H., Rupp, T., Iaconis, C., Walmsley, I. A., and Keller, U., "Spatially resolved amplitude and phase characterization of femtosecond optical pulses," *Optics Letters*, vol. 26, no. 2, pp. 96–98, 2001.

[56] Gordon, J. and Fork, R., "Optical resonator with negative dispersion," *Optics Letters*, vol. 9, no. 5, pp. 153–155, 1984.

[57] Gu, X., Kimmel, M., Shreenath, A. P., Trebino, R., Dudley, J. M., Coen, S., and Windeler, R. S., "Experimental studies of the coherence of microstructure-fiber supercontinuum," *Optics Express*, vol. 11, no. 21, pp. 2697–2703, 2003.

[58] Gu, X., Ahmad, F., Gaeta, A. L., Trebino, R., and Windeler, R. S., "Fine spectral features in single-shot microstructure-fiber continuum," in *Conference on Laser and Eletro-Optics (CLEO)*, (Baltimore, MD), 2003.

[59] Gu, X., Xu, L., Kimmel, M., O'Shea, P., Trebino, R., Windeler, R. S., Kerbage, C., and Eggleton, B. J., "The problem of collimating ultra-broadband continuum from microstructure fiber," in *Conference on Laser and Eletro-Optics (CLEO)*, (Baltimore, MD), 2001.

[60] Gu, X., Xu, L., Kimmel, M., Zeek, E., O'Shea, P., Shreenath, A. P., Trebino, R., and Windeler, R. S., "Frequency-resolved optical gating and single-shot spectral measurements reveal fine structure in microstructure-fiber continuum," *Optics Letters*, vol. 27, no. 13, pp. 1174–1176, 2002.

[61] Hartl, I., Li, X. D., Chudoba, C., Ghanta, R. K., Ko, T. H., Fujimoto, J. G., Ranka, J. K., and Windeler, R. S., "Ultrahigh-resolution optical coherence tomography using continuum generation in an air-silica microstructure optical fiber," *Optics Letters*, vol. 26, no. 9, pp. 608–610, 2001.

[62] Hebling, J., "Derivation of the pulse front tilt caused by angular dispersion," *Optical and Quantum Electronics*, vol. 28, no. 12, pp. 1759–1763, 1996.

[63] Hecht, E., *Optics*. Addison Wesley Longman, Inc., 3rd ed., 1998.

[64] Heritage, J. P., Weiner, A. M., and Thurston, R. N., "Picosecond pulse shaping by spectral phase and amplitude manipulation," *Optics Letters*, vol. 10, no. 12, pp. 609–611, 1985.

[65] Herrmann, J., Griebner, U., Zhavoronkov, N., Husakou, A., Nickel, D., Knight, J. C., Wadsworth, W. J., Russell, P. S. J., and Korn, G., "Experimental evidence for supercontinuum generation by fission of higher-order solitons in photonic fibers," *Physical Review Letters*, vol. 88, no. 17, p. 173901, 2002.

[66] Ho, K. M., Chan, C. T., and Soukoulis, C. M., "Existence of a photonic gap in periodic dielectric structures," *Physical Review Letters*, vol. 65, no. 25, pp. 3152–3155, 1990.

[67] Husakou, A. V. and Herrmann, J., "Supercontinuum generation of higher-order solitons by fission in photonic crystal fibers," *Physical Review Letters*, vol. 8720, no. 20, p. 203901, 2001.

[68] Husakou, A. V. and Herrmann, J., "Frequency comb generation by four-wave mixing in a multicore photonic crystal fiber," *Applied Physics Letters*, vol. 83, no. 19, pp. 3867–3869, 2003.

[69] Iaconis, C. and Walmsley, I., "Self-referencing spectral interferometry for measuring ultrashort optical pulses," *IEEE Journal of Quantum Electronics*, vol. 35, no. 4, pp. 501–509, 1999.

[70] Imeshev, G., Arbore, M. A., Fejer, M. M., Galvanauskas, A., Fermann, M., and Harter, D., "Ultrashort-pulse second-harmonic generation with longitudinally nonuniform quasi-phase-matching gratings: pulse compression and shaping," *Journal of the Optical Society of America B*, vol. 17, no. 2, pp. 304–318, 2000.

[71] Joannopoulos, J., Meade, R., and Winn, J., *Photonic Crystals: Molding the Flow of Light*. Princeton: Princeton University Press, 1995.

[72] Johnson, S. G. and Joannopoulos, J. D., "Block-iterative frequency-domain methods for Maxwell's equations in a planewave basis," *Optics Express*, vol. 8, no. 3, pp. 173–190, 2001.

[73] Kane, D. J. and Trebino, R., "Single-shot measurement of the intensity and phase of an arbitrary ultrashort pulse by using frequency-resolved optical gating," *Optics Letters*, vol. 18, no. 10, pp. 823–825, 1993.

[74] Kerbage, C. and Eggleton, B. J., "Numerical analysis and experimental design of tunable birefringence in microstructured optical fiber," *Optics Express*, vol. 10, no. 5, pp. 246–255, 2002.

[75] Kerbage, C. E., Eggleton, B. J., Westbrook, P. S., and Windeler, R. S., "Experimental and scalar beam propagation analysis of an air-silica microstructure fiber," *Optics Express*, vol. 7, no. 3, pp. 113–122, 2000.

[76] Knight, J. C., Arriaga, J., Birks, T. A., Ortigosa-Blanch, A., Wadsworth, W. J., and Russell, P. S., "Anomalous dispersion in photonic crystal fiber," *IEEE Photonics Technolology Letters*, vol. 12, no. 7, pp. 807–809, 2000.

[77] Knight, J. C., Birks, T. A., Russell, P. S., and Atkin, D. M., "All-silica single-mode optical fiber with photonic crystal cladding," *Optics Letters*, vol. 21, no. 19, pp. 1547–1549, 1996.

[78] Knight, J. C., Birks, T. A., Russell, P. S. J., and de Sandro, J. P., "Properties of photonic crystal fiber and the effective index model," *Journal of the Optical Society of America A*, vol. 15, no. 3, pp. 748–752, 1998.

[79] Knight, J. C., Broeng, J., Birks, T. A., and Russel, P. S. J., "Photonic band gap guidance in optical fibers," *Science*, vol. 282, no. 5393, pp. 1476–1478, 1998.

[80] Kostenbauder, A. G., "Ray-pulse matrices: A rational treatment for dispersive optical systems," *IEEE Journal of Quantum Electronics*, vol. 26, no. 6, pp. 1148–1157, 1990.

[81] Kozma, I. Z., Almasi, G., and Hebling, J., "Geometrical optical modeling of femtosecond setups having angular dispersion," *Applied Physics B*, vol. 76, no. 3, pp. 257–261, 2003.

[82] Kubota, H., Tamura, K. R., and Nakazawa, M., "Analyses of coherence-maintained ultrashort optical pulse trains and supercontinuum generation in the presence of soliton-amplified spontaneous-emission interaction," *Journal of the Optical Society of America B*, vol. 16, no. 12, pp. 2223–2232, 1999.

[83] Kuhlmey, B. T., White, T. P., Renversez, G., Maystre, D., Botten, L. C., de Sterke, C. M., and McPhedran, R. C., "Multipole method for microstructured optical fibers. II. implementation and results," *Journal of the Optical Society of America B*, vol. 19, no. 10, pp. 2331–2340, 2002.

[84] Linden, S., Giessen, H., and Kuhl, J., "XFROG—a new method for amplitude and phase characterization of weak ultrashort pulses," *Physica Status Solidi B*, vol. 206, no. 1, pp. 119–24, 1998.

[85] Liu, X., Xu, C., Knox, W. H., Chandalia, J. K., Eggleton, B. J., Kosinski, S. G., and Windeler, R. S., "Soliton self-frequency shift in a short tapered air-silica microstructure fiber," *Optics Letters*, vol. 26, no. 6, pp. 358–360, 2001.

[86] Martinez, O. E., "Grating and prism compressors in the case of finite beam size," *Journal of the Optical Society of America B*, vol. 3, no. 7, pp. 929–934, 1986.

[87] Martinez, O. E., "Pulse distortions in tilted pulse schemes for ultrashort pulses," *Optics Communications*, vol. 59, no. 3, pp. 229–232, 1986.

[88] Martinez, O. E., "Matrix formalism for pulse compressors," *IEEE Journal of Quantum Electronics*, vol. 24, no. 12, pp. 2530–2536, 1988.

[89] Martinez, O. E., "Matrix formalism for dispersive laser cavities," *IEEE Journal of Quantum Electronics*, vol. 25, no. 3, pp. 296–300, 1989.

[90] Martinez, O. E., Gordon, J. P., and Fork, R. L., "Negative group-velocity dispersion using refraction," *Journal of the Optical Society of America A*, vol. 1, no. 10, pp. 1003–1006, 1984.

[91] Michailov, N. I., "Passively mode-locked dye-laser with spatial-dispersion in the gain medium," *Journal of the Optical Society of America B*, vol. 9, no. 8, pp. 1369–1373, 1992.

[92] Mitschke, F. and Mollenauer, L., "Discovery of the soliton self-frequency shift," *Optics Letters*, vol. 11, no. 10, pp. 659–661, 1986.

[93] Nakazawa, M., Tamura, K., Kubota, H., and Yoshida, E., "Coherence degradation in the process of supercontinuum generation in an optical fiber," *Optical Fiber Technology*, vol. 4, no. 2, pp. 215–223, 1998.

[94] Nowak, G. A., Kim, J., and Islam, M. N., "Stable supercontinuum generation in short lengths of conventional dispersion-shifted fiber," *Applied Optics*, vol. 38, no. 36, pp. 7364–7369, 1999.

[95] Ohmae, G., Yagi, T., Nanri, K., and Fujioka, T., "Spatial spectrum chirp characteristic of a Martinez-type multipass pulse stretcher," *Japanese Journal of Applied Physics*, vol. 39, no. 10, pp. 5864–5869, 2000.

[96] Okoshi, T., *Optical fibers*. New York: Academic Press, 1982.

[97] Omenetto, F. G., Taylor, A. J., Moores, M. D., Arriaga, J., Knight, J. C., Wadsworth, W. J., and Russell, P. S. J., "Simultaneous generation of spectrally distinct third harmonics in a photonic crystal fiber," *Optics Letters*, vol. 26, no. 15, pp. 1158–1160, 2001.

[98] O'Shea, P., Kimmel, M., Gu, X., and Trebino, R., "Increased-bandwidth in ultrashort-pulse measurement using an angle-dithered nonlinear-optical crystal," *Optics Express*, vol. 7, no. 10, pp. 342–349, 2000.

[99] O'Shea, P., Kimmel, M., Gu, X., and Trebino, R., "Highly simplified ultrashort pulse measurement," *Optics Letters*, vol. 26, pp. 932–934, 2001.

[100] Peatross, J. and Rundquist, A., "Temporal decorrelation of short laser pulses," *Journal of the Optical Society of America B*, vol. 15, no. 1, pp. 216–222, 1998.

[101] Raghuramaiah, M., Sharma, A. K., Naik, P. A., and Gupta, P. D., "Simultaneous measurement of pulse-front tilt and pulse duration of a femtosecond laser beam," *Optics Communications*, vol. 223, no. 1-3, pp. 163–168, 2003.

[102] Ranka, J. K., Windeler, R. S., and Stentz, A. J., "Visible continuum generation in air-silica microstructure optical fibers with anomalous dispersion at 800 nm," *Optics Letters*, vol. 25, pp. 25–27, 2000.

[103] Ranka, J., Windeler, R., and Stentz, A., "Visible continuum generation in air-silica microstructure optical fibers with anomalous dispersion at 800 nm," in *Conference on Lasers and Electro-Optics*, (Baltimore), Optical Society of America, 1999.

[104] Ranka, J., Windeler, R., and Stentz, A., "Optical properties of high-delta air-silica microstructure optical fibers," *Optics Letters*, vol. 25, no. 11, pp. 796–8, 2000.

[105] Sacks, Z., Mourou, G., and Danielius, R., "Adjusting pulse-front tilt and pulse duration by use of a single-shot autocorrelator," *Optics Letters*, vol. 26, no. 7, pp. 462–464, 2001.

[106] Saitoh, K. and Koshiba, M., "Single-polarization single-mode photonic crystal fibers," *IEEE Photonics Technology Letters*, vol. 15, no. 10, pp. 1384–1386, 2003.

[107] Sala, K., Kenney-Wallace, G., and Hall, G., "CW autocorrelation measurements of picosecond laser pulses," *IEEE Journal of Quantum Electronics*, vol. 16, no. 9, pp. 990–996, 1980.

[108] Scarmozzino, R., Gopinath, A., Pregla, R., and Helfert, S., "Numerical techniques for modeling guided-wave photonic devices," *IEEE Journal of Selected Topics in Quantum Electronics*, vol. 6, no. 1, pp. 150–162, 2000.

[109] Sharping, J. E., Fiorentino, M., Coker, A., Kumar, P., and Windeler, R. S., "Four-wave mixing in microstructure fiber," *Optics Letters*, vol. 26, no. 14, pp. 1048–1050, 2001.

[110] Sharping, J., Fiorentino, M., Kumar, P., and Windeler, R., "All-optical switching based on cross-phase modulation in microstructure fiber," *IEEE Photonics Technology Letters*, vol. 14, no. 1, pp. 77–79, 2002.

[111] Smith, A. V., "Group-velocity-matched three-wave mixing in birefringent crystals," *Optics Letters*, vol. 26, no. 10, pp. 719–721, 2001.

[112] Sweetser, J., Fittinghoff, D., and Trebino, R., "Transient-grating frequency-resolved optical gating," *Optics Letters*, vol. 22, no. 8, pp. 519–521, 1997.

[113] Tanabe, T., Tanabe, H., Teramura, Y., and Kannari, F., "Spatiotemporal measurements based on spatial spectral interferometry for ultrashort optical pulses shaped by a Fourier pulse shaper," *Journal of the Optical Society of America B*, vol. 19, no. 11, pp. 2795–2802, 2002.

[114] Thurston, R., Heritage, J., Weiner, A., and Tomlinson, W., "Analysis of picosecond pulse shape synthesis by spectral masking in a grating pulse compressor," *IEEE Journal of Quantum Electronics*, vol. 22, no. 5, pp. 682–696, 1986.

[115] Trebino, R., DeLong, K. W., Fittinghoff, D. N., Sweetser, J. N., Krumbügel, M. A., Richman, B. A., and Kane, D. J., "Measuring ultrashort laser pulses in the time-frequency domain using frequency-resolved optical gating," *Review of Scientific Instruments*, vol. 68, no. 9, pp. 3277–3295, 1997.

[116] Trebino, R., *Frequency-Resolved Optical Gating*. Boston: Kluwer Academic Publishers, 2002.

[117] Trebino, R. and Kane, D. J., "Using phase retrieval to measure the intensity and phase of ultrashort pulses: frequency-resolved optical gating," *Journal of the Optical Society of America A*, vol. 10, no. 5, pp. 1101–1111, 1993.

[118] van Eijkelenborg, M. A., Large, M. C. J., Argyros, A., Zagari, J., Manos, S., Issa, N. A., Bassett, I., Fleming, S., McPhedran, R. C., de Sterke, C. M., and Nicorovici, N. A. P., "Microstructured polymer optical fibre," *Optics Express*, vol. 9, no. 7, pp. 319–327, 2001.

[119] Varjú, K., Kovács, A. P., Kurdi, G., and Osvay, K., "High-precision measurement of angular dispersion in a CPA laser," *Applied Physics B*, vol. 74, pp. S259–S263, 2002.

[120] Varjú, K., Kovács, A. P., Osvay, K., and Kurdi, G., "Angular dispersion of femtosecond pulses in a Gaussian beam," *Optics Letters*, vol. 27, no. 22, pp. 2034–2036, 2002.

[121] Wang, Y. M., Zhao, Y. H., Nelson, J. S., Chen, Z. P., and Windeler, R. S., "Ultrahigh-resolution optical coherence tomography by broadband continuum generation from a photonic crystal fiber," *Optics Letters*, vol. 28, no. 3, pp. 182–184, 2003. Article.

[122] Wefers, M. M. and Nelson, K. A., "Analysis of programmable ultrashort waveform generation using liquid-crystal spatial light modulators," *Journal of the Optical Society of America B*, vol. 12, no. 7, pp. 1343–1362, 1995.

[123] Wefers, M. M. and Nelson, K. A., "Space-time profiles of shaped ultrafast optical waveforms," *IEEE Journal of Quantum Electronics*, vol. 32, no. 1, pp. 161–172, 1996.

[124] Weiner, A. M., Heritage, J. P., and Kirschner, E. M., "High-resolution femtosecond pulse shaping," *Journal of the Optical Society of America B*, vol. 5, no. 8, pp. 1563–1572, 1988.

[125] White, T. P., Kuhlmey, B. T., McPhedran, R. C., Maystre, D., Renversez, G., de Sterke, C. M., and Botten, L. C., "Multipole method for microstructured optical fibers. I. formulation," *Journal of the Optical Society of America B*, vol. 19, no. 10, pp. 2322–2330, 2002.

[126] Wyatt, R. and Marinero, E., "Versatile single-shot background-free pulse duration measurement technique for pulses of subnanosecond to picosecond duration," *Applied Physics*, vol. 25, pp. 297–301, 1981.

[127] Xu, L., Gu, X., Kimmel, M., O'Shea, P., Trebino, R., and Galvanauskas, A., "Ultra-broadband IR continuum generation and its phase measurement using cross-correlation FROG," in *Conference on Lasers and Electro-Optics (CLEO)*, (Baltimore, MD), Optical Society of America, 2001.

[128] Xu, L., Kimmel, M., O'Shea, P., Trebino, R., Ranka, J. K., Windeler, R., and Stentz, A. J., "Measuring the intensity and phase of ultrabroad continuum," in *Conference on Lasers and Electro-Optics (CLEO)*, Trends in Optics and Photonics (TOPS), (San Francisco, CA), Optical Society of America, 2000.

[129] Zhu, Z. and Brown, T. G., "Full-vectorial finite-difference analysis of microstructured optical fibers," *Optics Express*, vol. 10, no. 17, pp. 853–864, 2002.

VITA

Xun Gu was born in Shanghai, China, in August 1975. He received the degrees of Bachelor of Science in Physics and Bachelor of Engineering in Economics/Management from the University of Science and Technology of China, Hefei, China, in 1998. Since then, he has been working in the School of Physics, Georgia Tech, where he conducts graduate research in the Ultrafast Optics Lab under the advisement of Professor Rick Trebino.